

ON THE CORRELATION OF DYNAMIC ELECTRIC-FIELD-INDUCED STRUCTURAL
CHANGES AND PIEZOELECTRICITY IN FERROELECTRIC CERAMICS

By

ABHIJIT PRAMANICK

A DISSERTATION PRESENTED TO THE GRADUATE SCHOOL
OF THE UNIVERSITY OF FLORIDA IN PARTIAL FULFILLMENT
OF THE REQUIREMENTS FOR THE DEGREE OF
DOCTOR OF PHILOSOPHY

UNIVERSITY OF FLORIDA

2009

© 2009 Abhijit Pramanick

To my parents

ACKNOWLEDGMENTS

I would like to thank my advisor Dr. Jacob L. Jones for providing me all the opportunities for completing this work and his guidance and assistance throughout. I would also like to express my gratitude to Dr. Dragan Damjanovic and Dr. John E. Daniels for their collaboration and helpful discussions, which contributed to significant portions of this work. I sincerely acknowledge the intellectual inputs from my committee members Dr. Juan C. Nino, Dr. David P. Norton, Dr. Aravind Asthagiri and Dr. Franky So.

I would like to acknowledge the following funding sources: funding from the National Science Foundation (NSF) under award number DMR-0746902; funding for travel to the Swiss Federal Institute of Technology (EPFL) through NSF award number OISE-0755170; funding to travel to Oak Ridge National Laboratories through the Oak Ridge Associated Universities (ORAU) Powe Junior Faculty Enhancement Award; travel funds to access the Australian Nuclear Science and Technology Organisation (ANSTO) provided by the University of Tennessee's International Materials Institute (IMI) ANSWER program and supported by NSF under award number DMR-0231320.

I want to thank all the present and past members of Dr. Jacob Jones' research group for their company and support – Shelley Cottrell, Anderson D. Prewitt, Wei Qiu, Martin McBriarty, Prateek Maheswari, Sandhya Nallamada, Chris Dosch, Elena Aksel, Chris Brink, Krishna Nittala, Kyle Calhoun and Paul Draper. Special thanks to Elena for her assistance while writing this dissertation. Also, I would like to thank Lu Cai for helping me with ferroelectric measurements in Dr. Nino's laboratory.

During this work, I had opportunities to spend time at other facilities as part of my research and education. I want to acknowledge members of the Ceramics Laboratory at the Swiss Federal Institute of Technology for providing company and assistance during a very productive and

enjoyable stay at EPFL. I want to especially thank Soodkhet (Bond) for showing me around in Sydney during my off-hours at ANSTO. I would also like to thank the organizers of the 10th National School on Neutron and X-ray Scattering, in which I had a chance to participate. I want to thank the fellow attendees of the school Aiming, Vibhor and others for the good times.

For all the varied and engaging discussions, not-so-apparent attempts at comedies, rivalries at the bowling alley, dinner and lunch times and all sort of things during the last four years, I want to thank Krishna (KP), Mahesh, Purushottam, Kalyan, Rakesh, Shobit, Sankara, David and Peter.

Finally, I want to acknowledge my family for all of their support during the good and bad times. I want to express my most heartfelt gratitude to my parents for which no amount of words would be enough. Their encouragement, support and guidance have been instrumental in all my life. This work is my humble tribute to all their love and support.

TABLE OF CONTENTS

	<u>page</u>
ACKNOWLEDGMENTS	4
LIST OF TABLES	9
LIST OF FIGURES	10
ABSTRACT	14
1 INTRODUCTION TO PIEZOELECTRICITY.....	16
1.1 Piezoelectric Ceramics.....	16
1.2 Structural Origin of Piezoelectricity in Ceramics.....	17
1.2.1 Intrinsic Mechanisms.....	20
1.2.2 Extrinsic Mechanisms	22
1.2.2.1 Rayleigh law.....	23
1.2.2.2 Preisach model	24
1.2.2.3 Micro-mechanical models.....	26
1.3 Diffraction Studies of Piezoelectric Mechanisms.....	27
2 OBJECTIVE AND OVERVIEW	42
3 SYNTHESIS OF LEAD ZIRCONATE TITANATE CERAMICS	45
3.1 Phase Diagram and Dopants for PZT	45
3.2 Synthesis of PZT Ceramics	46
4 NONLINEARITIES AND LOSSES IN CONVERSE PIEZOELECTRIC EFFECT OF PZT CERAMICS.....	56
4.1 Experimental Procedure.....	56
4.1.1 Converse Piezoelectric Measurements	56
4.1.2 Application of Rayleigh Law	57
4.1.3 Calculation of Piezoelectric Losses and Complex Coefficients.....	58
4.1.4 Measurement of the Harmonic Components of Converse Piezoelectric Strain	61
4.2 Results and Discussion	62
4.2.1 Piezoelectric Nonlinearity and Application of Rayleigh Law.....	62
4.2.1.1 Effect of crystal structure on nonlinear behavior	62
4.2.1.2 Effect of dopants on nonlinear behavior	64
4.2.1.3 Prediction of piezoelectric hysteresis from Rayleigh relations.....	65
4.2.2 Piezoelectric Losses and Complex Coefficients.....	66
4.2.3 Harmonics of the Converse Piezoelectric Strain.....	67
4.3 Conclusions.....	68

5	CHARACTERIZATION OF ELECTRIC-FIELD-INDUCED STRUCTURAL CHANGES USING LABORATORY X-RAY DIFFRACTION.....	81
5.1	Experimental Procedure.....	81
5.1.1	In situ X-ray Diffraction Under Application of Electric Field.....	82
5.1.1.1	Diffraction under static electric fields.....	82
5.1.1.2	Diffraction under cyclic electric fields.....	82
5.1.2	Quantification of Structural Changes.....	84
5.2	Results and Discussions.....	87
5.2.1	Structural Changes Under Static Electric Fields.....	87
5.2.2	Structural Changes Under Cyclic Electric Fields.....	89
5.3	Conclusions.....	92
6	CHARACTERIZATION OF ELECTRIC-FIELD-INDUCED STRUCTURAL CHANGES USING HIGH-ENERGY SYNCHROTRON X-RAY DIFFRACTION.....	101
6.1	Experimental Procedure.....	101
6.1.1	Sample Synthesis and Preparation.....	101
6.1.2	Time-Resolved Diffraction.....	102
6.2	Analysis of Diffraction Data.....	103
6.2.1	Binning of Diffraction Data at Different Azimuthal Angles.....	103
6.2.2	Fitting of (<i>hkl</i>) Diffraction Peaks.....	103
6.2.3	Analysis of Ferroelectric Phases.....	104
6.2.4	Binning of Diffraction Data with Respect to Time.....	105
6.2.5	Quantification of Structural Changes.....	107
6.2.5.1	Non-180° domain switching.....	107
6.2.5.2	Electric-field-induced lattice strains.....	109
6.3	Results and Discussions.....	110
6.3.1	Non-180° Domain Switching.....	110
6.3.2	Calculation of Strain from Non-180° Domain Switching.....	113
6.3.3	Field Dependence of Non-180° Domain Switching Strains.....	114
6.3.4	Electric-Field-Induced Lattice Strains.....	116
6.4	Conclusions.....	118
7	NONLINEAR CONTRIBUTIONS FROM STRUCTURAL MECHANISMS UNDER CYCLIC ELECTRIC FIELDS.....	135
7.1	Effect of Non-180° Domain Switching Strains.....	135
7.2	Effect of Lattice Strains.....	138
7.3	Cumulative Nonlinear Contributions from Different Structural Mechanisms.....	141
7.4	Conclusions.....	143
8	SUMMARY AND FUTURE WORK.....	152
8.1	Summary.....	152
8.2	Suggestions for Future Work in this Area.....	157
8.2.1	Nonlinearity in Direct Piezoelectric Behavior.....	157

8.2.2 Frequency Dependence of Piezoelectric Coefficients	158
8.2.3 Temperature Dependence of Piezoelectric Nonlinearity and Frequency Dispersion	159
8.2.4 Piezoelectric Nonlinearity and Frequency Dispersion in Lead-Free Piezoceramics	160
8.2.5 Piezoelectric Nonlinearity and Frequency Dispersion in Ferroelectric Thin Films	161

APPENDIX

A EFFECT OF SAMPLE DISPLACEMENT ON DIFFRACTION PEAK POSITION FOR A CPS DETECTOR.....	165
B STROBOSCOPIC DATA COLLECTION USING MCDWIN	168
C PENETRATION DEPTH OF X-RAYS IN PZT CERAMICS	170
D IGOR CODES FOR ANALYSIS OF 2-DIMENSIONAL DIFFRACTION DATA	173
REFERENCES	195
BIOGRAPHICAL SKETCH	200

LIST OF TABLES

<u>Table</u>	<u>page</u>
3-1. The measured densities and the percent theoretical densities for the different samples ...	54
3-2. List of the samples used for experiments in this work.....	55
4-1. Harmonics of the converse piezoelectric strains for PLZT5248.	80
7-1. α_d and $\alpha_{\text{non-180}^\circ}$ for the different samples studied.	150
7-2. The values of T_{hkl} and m_{hkl} for the different hkl crystallographic poles used to calculate the total effective lattice strain.....	151

LIST OF FIGURES

<u>Figure</u>	<u>page</u>
1-1. Unit cell of a cubic perovskite crystal structure.....	28
1-2. Domain variants in ferroelectric ceramics shown as arrangement of polarization axes of adjacent domains..	29
1-3. The different structural changes in a ferroelectric ceramic from a paraelectric state above T_C to a ‘poled’ ferroelectric state with reference to a tetragonal crystal structure.....	30
1-4. The effect of reorientation of domains under applied electric field on A) the polarization, and B) the strain of a piezoelectric ceramic.....	31
1-5. The elastic free energy profiles for polarization contraction/elongation and polarization rotation in tetragonal PZT with Zr/Ti ratio of 40/60.	33
1-6. The electric-field-induced lattice strain coefficients for different crystal orientations within a polycrystalline tetragonal lead zirconate titanate piezoelectric ceramic under cyclic electric actuation.....	34
1-7. Illustration of energy profile for domain wall motion in a medium with random pinning centers.....	35
1-8. Application of Rayleigh law for direct piezoelectric behavior of 4 atomic % Nb-doped PZT ceramics with Zr/Ti ratio of 63/37.....	36
1-9. Energy profile (left), and square hysteresis (right) of an elementary bistable unit, as assumed in Preisach model for hysteresis. m represents generalized susceptibility.....	37
1-10. Energy profile and hysteresis of bistable units as a function of their position on the Preisach plane at zero applied field.	38
1-11. Preisach distribution function for different characteristic piezoelectric behaviors.	39
1-12. Simulated and measured x - E hysteresis loops for La-doped PZT ceramics using micro-mechanical models based on energy criterion for switching, as described in Eq. 1-7.....	40
1-13. Non-180° domain switching fraction ($\Delta\eta_{002}$) in tetragonal PZT ceramics under applied unipolar and bipolar electric fields, as a function of field amplitude.....	41
3-1. Phase diagram and piezoelectric coefficients of PZT ceramics. $PbZrO_3 - PbTiO_3$ phase diagram over compositional range close to the morphotropic phase boundary (MPB) is shown in the bottom half of the plot.	50

3-2.	A) Scanning electron micrograph of fracture surface of PLZT5248; the grain size is of the order of 1-2 μm . B) X-ray diffraction patterns of the sintered ceramics.....	51
3-3.	A) Polarization-electric field, and B) strain-electric field hysteresis loops of the various samples.....	52
4-1.	Experimental setup for measuring converse piezoelectric strain.....	70
4-2.	The piezoelectric coefficient d_{33} was calculated from the measured peak-to-peak longitudinal strain, indicated as x_{max} , using Eq. 4-1.	71
4-3.	Converse piezoelectric coefficients of PLZT6040, PLZT5248 and PLZT4060 as a function of applied sinusoidal electric field amplitudes.	72
4-4.	Estimate of the irreversible extrinsic contributions for La-doped PZT ceramics as a function of applied sinusoidal electric field amplitudes.	73
4-5.	Converse piezoelectric coefficients and fractional extrinsic contributions for PLZT5248, PUZT5248 and PFZT4753.....	74
4-6.	The strain-electric field hysteresis loops for the PZT ceramic samples at electric field amplitudes 400 V/mm and 600 V/mm: A) PLZT5248, B) PLZT6040, C) PLZT4060, D) PUZT5248.	75
4-7.	Hysteresis area and imaginary piezoelectric coefficient.....	79
5-1.	Experimental setup and synchronization settings for <i>in situ</i> diffraction experiments.	94
5-2.	The fit for the (002)-type diffraction peaks for an unpoled sample of the type PLZT5248.....	95
5-3.	Structural changes measured under the application of stepwise static electric fields: A) η_{002} and B) ϵ_{111} , as a function of the field amplitude.	96
5-4.	Schematic of the proposed 90° domain switching process under static electric fields E_0	97
5-5.	Structural changes as a function of time during the application of cyclic square wave electric field of amplitude ± 650 V/mm and of frequency 0.3 Hz.....	98
5-6.	Measured and fit patterns of the A) (002)-type, and B) (111) diffraction peaks, during the positive and the negative parts of the applied electric field waveform.	99
5-7.	Dependence of non-180° domain switching and 111 lattice strains on amplitude of applied cyclic electric fields.....	100
6-1.	Details about experimental setup and timing electronics for <i>in situ</i> diffraction experiments.....	120

6-2.	Specific diffraction peaks for the different samples used in the current experiments.	121
6-3.	Time-resolved structural changes under cyclic electric fields.	122
6-4.	η_{002} as a function of field amplitude as well as orientation with respect to the direction of applied field, for an unpoled La-doped tetragonal PZT ceramic under the application of static electric fields.	125
6-5.	Change in volume fraction of non-180° domains in La-doped PZT ceramics under application of cyclic electric fields.	126
6-6.	$\Delta\eta_{002}$ for different amplitudes of applied cyclic square wave electric fields, for A) sample PUZT5248, and B) sample PFZT4753.	129
6-7.	Illustration of strain due to non-180° switching of ferroelastic domains in a single grain.	130
6-8.	The coefficient of strain due to non-180° domain switching $d_{\text{non-180}^\circ}$ for PZT ceramics.	131
6-9.	Electric-field-induced lattice strain coefficients in PZT ceramics.	133
7-1.	Nonlinear contributions to macroscopic electric-field-induced strains and nonlinear contributions from non-180° domain switching strains for samples A) PLZT6040, B) PLZT5248, C) PUZT5248, D) PFZT4753.	144
7-2.	A simplified schematic illustration of cumulative addition of strains with different hkl orientations towards macroscopic electric-field-induced strain.	146
7-3.	The total effective lattice strain coefficient as a function of the amplitude of the applied cyclic electric field.	147
7-4.	Nonlinear contributions to macroscopic electric-field-induced strain in sample PLZT5248 as a function of amplitude of applied electric field.	148
7-5.	Illustration of intergranular interactions leading to elastic strains for grains with different orientations.	149
8-1.	Variation of converse piezoelectric coefficients of PLZT5248, as a function of frequency of applied electric fields.	162
8-2.	The time-dependent changes in the 111 lattice strains in PLZT5248 ceramic, parallel to the direction of the applied electric fields of different frequencies.	163
8-3.	The electric-field-induced 111 lattice strains ε_{111} , as a function of time during application of a bipolar electric waveform of amplitude ± 0.4 kV/mm and frequencies of A) 1 Hz, B) 10 Hz, C) 100 Hz, and D) 500 Hz, for EC65 ceramics.	164

A-1.	Diffraction geometry and peak shift due to sample displacement, for a CPS detector. ...	167
B-1.	Sequential steps for enabling stroboscopic data collection.....	169
C-1.	Fraction of diffracted intensities as a function of thickness of diffracting volume for A) X-rays from a Cu-K α source, B) high energy X-rays (87.80 keV) from a synchrotron source.	172

Abstract of Dissertation Presented to the Graduate School
of the University of Florida in Partial Fulfillment of the
Requirements for the Degree of Doctor of Philosophy

ON THE CORRELATION OF DYNAMIC ELECTRIC-FIELD-INDUCED STRUCTURAL
CHANGES AND PIEZOELECTRICITY IN FERROELECTRIC CERAMICS

By

Abhijit Pramanick

May 2009

Chair: Jacob L. Jones

Major: Materials Science and Engineering

Piezoelectric ceramics are used in various devices such as sensors and actuators for conversion of electrical signals into mechanical signals and vice versa. In order to gain more insight into the fundamental behavior of these materials, the present work reconciles macroscopic piezoelectric nonlinearities with respect to the electric-field-induced microstructural and crystallographic changes in ferroelectric lead zirconate titanate (PZT) ceramics.

Nonlinearity and hysteresis in piezoelectric response under cyclic electric fields are investigated as a function of crystallographic phase (rhombohedral and tetragonal) and different dopants (undoped, La, and Fe). For longitudinal piezoelectric response, the amount of nonlinear contributions from irreversible extrinsic mechanisms in the rhombohedral phase is observed to be greater than in tetragonal phases for all amplitudes of applied electric fields. Likewise, La-doping increases the amount of nonlinear contributions from irreversible extrinsic mechanisms as compared to both undoped and Fe doped ceramics. The largest irreversible extrinsic contribution is observed to be about 55% of the total electric-field-induced strain for 2 atomic % La-doped rhombohedral PZT ceramics, for an applied electric field of ± 750 V/mm.

Structural changes under the application of cyclic electric fields are measured by time-resolved diffraction using both laboratory and synchrotron X-ray sources. From time-resolved X-

ray diffraction experiments, the largest non-180° domain switching strains are observed for 2 atomic % La-doped tetragonal PZT ceramics of compositions close to the morphotropic phase boundary. It is further observed that both non-180° domain switching and lattice strains can be nonlinear with respect to the applied electric fields.

The nonlinear contributions from different structural changes to macroscopic electric-field-induced strains are subsequently analyzed. Quantitative analyses show only partial contribution from non-180° domain switching towards macroscopic piezoelectric nonlinearity for La-doped and undoped compositions. This is consistent with certain additional nonlinear contributions determined from different *hkl* lattice strains. It is proposed that the nonlinear lattice strains originate through intergranular constraints and are therefore influenced by non-180° domain switching in the material.

It is therefore concluded that the displacement of non-180° domain walls is the primary driving mechanism but not necessarily contribute exclusively towards macroscopic piezoelectric nonlinearity in ferroelectric PZT ceramics.

CHAPTER 1 INTRODUCTION TO PIEZOELECTRICITY

A brief description of the fundamentals of piezoelectricity is provided in this chapter along with an overview of the present understanding of the different structural mechanisms contributing to piezoelectric effect in ferroelectric ceramics. This chapter is intended as a background for the concepts developed later in the dissertation. Readers with advanced understanding of piezoelectricity in solids are referred to Chapter 2 for objective and overview of the present work.

1.1 Piezoelectric Ceramics

Piezoelectric ceramics are an important part of many modern technologies. Actuators based on piezoelectric ceramics transform electrical energy to an induced linear or rotary motion and are valuable in applications which require fast response, high precision, high structural endurance, and high power-to-weight ratio [1]. Some devices that use this technology include precise positioning systems, fuel injectors, sonar and ultrasonics.

Piezoelectricity is the coupling between the dielectric and the elastic displacements in a material. The linear relations for direct and converse piezoelectric effects are shown in Eqs. 1-1 and 1-2 respectively,

$$D_i = d_{ijk} X_{jk}, \quad (1-1)$$

$$x_{jk} = d_{ijk} E_i, \quad (1-2)$$

where d_{ijk} is a constant called the piezoelectric coefficient, D_i is the induced charge density, X_{jk} is the applied mechanical stress, x_{jk} is the induced strain and E_i is the applied electric field. The piezoelectric coefficient d_{ijk} is a third rank tensor that relates second rank tensors X_{jk} and x_{jk} with

first rank tensors D_i and E_i , respectively. The tensor d_{ijk} is often represented in a simplified matrix form of d_{mn} [2].

The phenomenon of converse piezoelectric effect is utilized to achieve controlled actuation under applied electric fields. An accurate description of electric-field-induced strains is necessary in high-precision actuator applications. In many instances, the “apparent” converse piezoelectric coefficient d_{mn} of a material is found to be a function of the applied electric field amplitude E_i [3-5]. Under such circumstances, the linear relationship described in Eq. 1-2 no longer remains valid.

Insight into the physical origins of nonlinear converse piezoelectric responses can be obtained from an analysis of induced structural changes such as domain switching and lattice strains under the application of electric fields. More specifically, nonlinear contributions from different possible structural mechanisms can be distinguished by direct measurements of such structural changes under the application of electric fields.

1.2 Structural Origin of Piezoelectricity in Ceramics

An understanding of the phenomenon of piezoelectricity in solids requires an understanding of the internal structure of the material or more precisely the change of structure under electrical or mechanical fields. In principle, the existence of piezoelectricity in a material is decided by the absence of a center of symmetry in its crystal structure. In addition, most piezoelectric ceramic materials are ferroelectric, which means that each crystallographic unit cell has a spontaneous and reversible polarization or dipole moment under certain conditions. The spontaneously polarized crystallites are further arranged in a complex three-dimensional pattern within a polycrystalline ceramic material. The electric-field-induced macroscopic strain in a piezoelectric ceramic is therefore a result of different structural changes, as described below.

The crystal structures of most widely used piezoelectric ceramics, such as BaTiO_3 and $\text{Pb}(\text{Zr,Ti})\text{O}_3$, belong to the perovskite family. In simple terms, the structure can be described as a network of corner-linked oxygen octahedra, with the smaller cation filling the octahedral holes and the larger cation filling the dodecahedral holes. The unit cell of a cubic perovskite structure can be represented as shown in Figure 1-1; the large cations (A) occupy the corners, the smaller cation (B) occupies the body center while the oxygen ions (O) occupy the face centers of the unit cell. When a ferroelectric ceramic is cooled through a certain temperature, the crystallographic unit cell typically undergoes distortion from a cubic structure to a lower symmetry structure with a spontaneous polarization. The temperature at which this transformation occurs coincides with the Curie temperature. For example, BaTiO_3 undergoes a second order phase transformation from a cubic paraelectric phase to a tetragonal ferroelectric phase at 130°C . In addition, a spontaneous polarization develops within each unit cell due to a shift in the relative positions of the ions. As the strains arising from crystallographic distortions give rise to internal stresses within the ceramic, twin-like patterns called domains are formed. A domain is a homogeneous area in the material having a uniform orientation of the polarization axis. The boundaries between the domains are defined by the angle between the polarization axes of the adjacent domains. Mainly they are classified as 180° domain walls (adjacent domains are antiparallel with each other) and non- 180° domain walls (polarization directions of adjacent domains are arranged in head-to-tail configurations at angles different than 180°), as shown in Figure 1-2.

In the as-sintered state, a ceramic is non-piezoelectric though the individual domains can exhibit piezoelectricity due to further lattice distortions under external fields. This happens because the polarization and strain components of all the randomly oriented domains cancel each other and no significant net macroscopic polarization or strain develops in the material.

However, the volume fractions of the differently oriented domains in a material can be changed under the application of electric fields of high enough amplitudes. The process of creating a preferred orientation of domains within a ferroelectric/piezoelectric ceramic is called poling. When ‘poled,’ the polarization and strain components of the different domains in the ceramic contribute towards a net dielectric and piezoelectric response. The different structural changes in a ferroelectric ceramic from a paraelectric state above T_C to a ‘poled’ ferroelectric state are shown in Figure 1-3 with reference to a tetragonal crystal structure. Some ceramics with orthorhombic, rhombohedral and monoclinic crystal structures are also known to be ferroelectric and exhibit similar structural changes as a function of temperature and applied electric field [6,7].

The above discussion provides only a partial description of the structural changes in a piezoelectric ceramic under the application of electric fields. The domain configuration in the material achieved after poling is not rigid but can be subjected to further rearrangements under subsequent applications of electric fields. Such rearrangements can be brought about by vibration or displacement of the existing domain walls. A change in the volume fraction of the differently oriented domains will disrupt the existing continuity of the uniformly polarized regions in the material and consequently will contribute to its macroscopic polarization and strain. When the applied electric field exceeds a certain critical limit called the coercive field E_C , a large-scale switching of domains towards an energetically preferred direction takes place – leading to a nonlinear change in macroscopic polarization and strain. Figure 1-4 illustrates the effect of reorientation of domains under applied electric field on the polarization and strain of a piezoelectric ceramic [4].

In some actuator applications, such as fuel injectors in diesel engines, piezoelectric ceramics are subjected to cyclic electric fields of subcoercive amplitudes [7,8]. Under such loading conditions, both lattice distortions and domain wall motions can contribute to the macroscopic electric-field-induced strain in the material [9]. The former is generally referred to as an intrinsic mechanism while the latter is referred to as an extrinsic mechanism [4]. In order to better predict the material behavior for such applications, it is helpful to understand the various structural mechanisms operating in piezoelectric ceramics under the application of cyclic electric fields. A brief overview of the present understanding of intrinsic and extrinsic piezoelectric mechanisms is provided in Sections 1.2.1 and 1.2.2.

1.2.1 Intrinsic Mechanisms

The intrinsic piezoelectric response can be defined as that arising due to distortion of crystallographic unit cells within a single domain, single crystal material [5,10]. The intrinsic piezoelectric properties of a material can be measured at low temperatures at which the various extrinsic contributions can be presumably excluded [11]. Alternately, they can be determined based on first-principle calculations [12-16] or from macroscopic physical properties using thermodynamic phenomenological models. The Landau-Ginsburg-Devonshire (LGD) thermodynamic theory has been used in the past for interpretation of piezoelectric properties of many perovskite ferroelectric materials. An example of the application of the LGD theory is provided here for lead zirconate titanate (PZT) solid solutions [17-24].

The tetragonal and high-temperature rhombohedral phases of the PZT solid solutions undergo proper ferroelectric transitions from the paraelectric cubic ($m3m$) state, where the spontaneous polarization is the order parameter for the phase transition. Therefore, the elastic Gibbs free energy of a PZT crystal can be expressed as a function of powers of the spontaneous

ferroelectric polarizations, the coupling between the various polarizations and the coupling between the polarizations and stress, as [5,19]

$$\begin{aligned}
\Delta G = & \alpha_1(P_1^2 + P_2^2 + P_3^2) + \alpha_{11}(P_1^4 + P_2^4 + P_3^4) + \alpha_{12}(P_1^2 P_2^2 + P_2^2 P_3^2 + P_3^2 P_1^2) \\
& + \alpha_{111}(P_1^6 + P_2^6 + P_3^6) + \alpha_{112}[P_1^4(P_2^2 + P_3^2) + P_2^4(P_3^2 + P_1^2) + P_3^4(P_1^2 + P_2^2)] \\
& + \alpha_{123}(P_1^2 P_2^2 P_3^2) - \frac{1}{2}s_{11}^D(\sigma_1^2 + \sigma_2^2 + \sigma_3^2) \\
& - s_{12}^D(\sigma_1\sigma_2 + \sigma_2\sigma_3 + \sigma_3\sigma_1) - \frac{1}{2}s_{44}^D(\sigma_4^2 + \sigma_5^2 + \sigma_6^2) - Q_{11}(\sigma_1 P_1^2 + \sigma_2 P_2^2 + \sigma_3 P_3^2) \\
& - Q_{12}[\sigma_1(P_2^2 + P_3^2) + \sigma_2(P_3^2 + P_1^2) + \sigma_3(P_1^2 + P_2^2)] \\
& - Q_{44}(\sigma_4 P_2 P_3 + \sigma_5 P_3 P_1 + \sigma_6 P_1 P_2)
\end{aligned} \tag{1-3}$$

where α 's are the ferroelectric dielectric stiffnesses at constant stress, P_i are the spontaneous polarizations, σ_i are the stress component in the Voigt notation, s_{ij}^D are the elastic compliances at constant polarization, and Q_{ij} are the electrostrictive coupling coefficients between the ferroelectric polarization and stress. Eq. 1-3 is described in the coordinate system of the parent cubic phase ($m3m$). The various parameters in Eq. 1-3 can be obtained through measurement of relevant physical properties such as spontaneous strains and subsequently relating these properties to the various parameters. Once the various parameters could be evaluated, the elastic Gibbs free energy along the various crystallographic directions can be calculated following Eq. 1-3. In effect, such a profile shows the variation of the elastic energy due to atomic shifts in a particular crystallographic direction. A flatter profile in a certain direction indicates a higher susceptibility of the system to atomic displacements in that particular direction, leading to anisotropic dielectric and piezoelectric properties.

The calculation of the longitudinal piezoelectric coefficients d_{33} along the various crystallographic directions for piezoelectric materials, using LGD theory, has been demonstrated [5,25-27]. For example, in tetragonal PZT with Zr/Ti ratio of 40/60, the elastic free energy

profiles for the following two situations: (a) for elongation or contraction of polarization parallel to the polar axis of [001] ($P_2=0; P_3 \neq 0$), and (b) polarization rotation away from the polar axis of [001] ($P_2 \neq 0; P_3 = P_3$, P_3 is the equilibrium polarization at 298 K), are shown in Figures 1-5A and 1-5B, respectively. The longitudinal piezoelectric coefficients, calculated from the ΔG profiles, are shown in Figure 1-5C as a polar plot. It can be seen from Figure 1-5C, that for tetragonal PZT the largest piezoelectric constants can be expected parallel to the polar axis of [001] and decreases as one moves away from the direction of the polar axis [26].

In polycrystalline bulk ceramics, the observed piezoelectric response along the various crystallographic directions can differ from the predictions of the LGD theory. The electric-field-induced lattice strain coefficients for different crystal orientations within a polycrystalline tetragonal lead zirconate titanate piezoelectric ceramic under cyclic electric actuation are shown in Figure 1-6 [28]. It can be seen that the maximum electric-field-induced lattice strains are observed for crystallographic orientations with polar axis oriented away from the direction of the applied electric field. This is in contrast with LGD theory which predicts largest longitudinal piezoelectric coefficients along the polar axis of [001] in tetragonal PZT. The possible reasons for disagreements between thermodynamic predictions and measured lattice strains in piezoelectric ceramics can be speculated to be due to the following: (1) deviations of crystallographic symmetry from a tetragonal state [29], (2) nonzero stress state for the grains within a polycrystalline matrix [26], (3) inter-/intragranular strains under electrical cycling [30,31].

1.2.2 Extrinsic Mechanisms

Contributions to piezoelectric responses in ceramics which are not attributed to intrinsic mechanisms can be termed as extrinsic. Extrinsic contribution to dielectric properties of

ferroelectrics was recognized very early from their polarization-electric field hysteresis loops [32]. The principal mechanisms proposed for dielectric extrinsic contributions included domain switching and domain wall vibrations [33]. Later studies concentrated on describing the relationship between the dielectric constant (ϵ) and the amplitude of the applied electric field (E_0) for ferroelectrics [34-41]. Linear [37-41] or quadratic [36] dependence of ϵ on E_0 had been reported earlier for PZT ceramics. Extrinsic contributions to piezoelectric properties of ferroelectrics were undertaken in subsequent studies. A brief description of different approaches for interpretation of extrinsic piezoelectric contributions in ferroelectrics is given below.

1.2.2.1 Rayleigh law

Systematic studies of extrinsic contributions to piezoelectric properties in ferroelectric ceramics were pioneered by Damjanovic and coworkers during the late 1990's. The direct longitudinal piezoelectric coefficients (d_{33}) of different ferroelectric ceramics were studied under subswitching mechanical stresses [42-44]. It was shown for the studied materials that the Rayleigh law for ferromagnetic materials [45] can be successfully applied to describe the behavior of the piezoelectric charge and piezoelectric coefficients under low amplitudes of applied mechanical stresses. Within a certain range of applied stress amplitudes the piezoelectric coefficient d_{33} was observed to be a linear function of the amplitude of the applied mechanical stress (X_0), as described below

$$d_{33}(X_0) = d_{init} + \alpha X_0, \quad (1-4)$$

where d_{init} is the piezoelectric coefficient at the limit of zero amplitude of applied mechanical stress, and α describes the linear dependence of the piezoelectric coefficient d_{33} on the amplitude of the applied stress. In effect, d_{init} is the contribution to the piezoelectric coefficient from intrinsic lattice strains and reversible domain wall displacements, and αX_0 is the contribution

originating from the irreversible displacement of domain walls. The distinction between reversible and irreversible displacements of domain walls can be described from the energy profile for domain wall motion in a medium with random pinning centers, as is illustrated in Figure 1-7. Reversible domain wall displacements involve motion around an equilibrium position at the bottom of a potential well, while irreversible domain wall displacements occur across potential energy barriers.

Since a variable d_{33} will result in departure from the linear relationship described in Eq. 1-1, the piezoelectric response of the material becomes nonlinear with respect to the applied mechanical stress X . It was further shown that relationship between nonlinearity and hysteresis in ferroelectric ceramics can be related following,

$$D = (d_{init} + \alpha X_0)X \pm \frac{\alpha}{2}(X_0^2 - X^2), \quad (1-5)$$

for an applied cyclic mechanical stress of amplitude X_0 , where at a particular instant D is the piezoelectric charge density and X is the applied mechanical stress. [42-44]

Studies on nonlinearity and hysteresis of converse piezoelectric effect were also undertaken in subsequent years [41,46,47]. It was shown that, for certain piezoelectric materials and within certain range of applied electric field amplitudes, relations similar to Eqs. 1-4 and 1-5 can be applied to describe converse piezoelectric behavior. Figure 1-8A shows the longitudinal piezoelectric d_{33} coefficient of 4 atomic % Nb-doped PZT ceramics with Zr/Ti ratio of 63/37, as a function of amplitude of applied a.c. pressure [43]. Figure 1-8B shows the corresponding hysteresis loop for this material calculated for $\sigma_0 \approx 2.6$ MPa, using Eq. 1-5 [43].

1.2.2.2 Preisach model

The physical interpretation of Rayleigh law for magnetism in terms of magnetic regions or units was attempted by several investigators [48-50]. These type of models are most well

known as Preisach-type models [51]. Application of Preisach model for ferroelectric materials was done by Turik in 1960s [52-54]. In recent years, Preisach model has been successfully applied to describe piezoelectric nonlinearity and hysteresis in ferroelectric materials by Damjanovic and coworkers [4,55-57]. A brief description of the Preisach model is provided here. It is assumed in this model that a hysteretic piezoelectric system is composed of simple bistable units (such as domain walls in a media with pinning centers) where each unit can be characterized by following two parameters: (a) a bias field F_i , and (b) a coercive field F_c . Each state of the unit is assumed to contribute to the macroscopic piezoelectric response R by an amount $\pm R_0$, as illustrated in Figure 1-9. Further, it is defined that $-\infty < F_i < +\infty$ and $0 < F_c$. The possible values of F_i and F_c can be represented on a plane called Preisach plane as shown in Figure 1-10. The density of the bistable units in the Preisach plane can be defined by a distribution function $f(F_i, F_c)$, which obeys the following normalization condition,

$$\int_0^{\infty} \int_{-\infty}^{+\infty} f(F_i, F_c) dF_i dF_c = 1. \quad (1-6)$$

The Preisach description is only applicable for hysteretic systems which follow the necessary conditions of return-point memory and congruency [51,58]. This condition is usually satisfied for ferroelectric materials [59,60].

In the absence of any external field, the Preisach plane can be divided into three regions, as shown in Figure 1-10: (a) $F_i > F_c$ with a negative zero field state ($-R_0$); (b) $F_c > |F_i|$ with a indefinite zero field state; and (c) $F_i < -F_c$ with a positive zero field state ($+R_0$). When an external field is applied, it acts similar to a homogeneous bias field and accordingly moves the region (b) upwards or downwards. For increasing fields, the region (b) is shifted up and all bistable units with the condition $F_i + F_c < F$ are switched to a positive state thereby contributing to the total response by $+2R_0$. For decreasing fields, the region (b) is shifted down and all bistable units with

the condition $F_i - F_c < F$ are switched to a positive state thereby contributing to the total response by $+2R_0$. Integration of the distribution function $f(F_i, F_c)$, over a portion of the Preisach plane, as defined by the applied field profile, can describe the shape of the hysteresis loop. It can be shown that the Rayleigh law for piezoelectrics corresponds to a uniform distribution function, as shown in Figure 1-11A [4]. For cases where the hysteresis cannot be described by Rayleigh law, such as in hard PZT ceramics, the shape of the hysteresis loop can be described by a different distribution function as shown in Figure 1-11B [4,57].

1.2.2.3 Micro-mechanical models

Rather than an extensive review of micro-mechanical modeling for piezoelectrics, a general approach for such modeling is given in this section. In this approach, a piezoelectric ceramic is considered to be made up from an array of single domain grains. Ferroelectric or ferroelastic switching in these grains can occur when the energy provided by the applied electric or stress field exceeds a certain critical value. The energy criterion can be described as follows,

$$E_i \Delta P_i + X_{jk} x_{jk} \geq 2P_s E_{crit} \quad (1-7)$$

where P_s is the spontaneous polarization, E_i is the applied electric field, X_{jk} and x_{jk} are the stress and strain states, and E_{crit} is the critical field for polarization switching [61]. Figure 1-12 shows a comparison between the simulated and measured x - E relationships for La-doped PZT ceramics. Further development of such models could incorporate the effect of static stress and grain to grain interaction on polarization switching [62]. The main principal shortcoming of these models is the various simplifying assumptions required for their implementation such as single domain grains.

1.3 Diffraction Studies of Piezoelectric Mechanisms

In situ and *ex situ* diffraction of piezoelectrics have proved to be a highly useful experimental technique in order to gain insight into the relative electromechanical contributions from intrinsic and extrinsic mechanisms under the application of static electric fields. [9,30,31,63-71] Most of these studies in piezoelectric ceramics have been conducted for the lead zirconate titanate (PZT) solid solutions, which have wide technological application as well as being studied as a model system for fundamental understanding of piezoelectric phenomenon in ceramics. These experiments have demonstrated that changes in the volume fractions of the non-180° domains as a result of domain wall motion can be characterized from the changes in the relative intensities of the diffraction peaks which are characteristic of a particular ferroelectric distortion. For example in tetragonal PZT with a ferroelectric distortion along [001], relative intensities of $(00h)$ and $(h00)$ diffraction peaks, where h is an integer can be used to quantify changes in the volume fractions of the 90° domains. At the same time, by noting the shift in the angular position of the (hkl) diffraction peaks it is possible to calculate the amount of hkl lattice strains in response to an applied electric field. While structural measurements of piezoelectric materials under static electric fields provide valuable insight into the various electromechanical mechanisms, such measurements do not provide information about material behavior under cyclic electric fields, as is used in various actuation devices. For the measurement of structural changes in piezoelectric ceramics under cyclic electric fields, time-resolved diffraction techniques have been demonstrated to be useful [9,72-74]. It has been shown that under increasing amplitudes of applied cyclic electric fields, amount of non-180° domain switching increases linearly, as shown in Figure 1-13 [72,73]. This type of linear relationship bears resemblance to the linear variation of piezoelectric coefficients as described by Rayleigh law.

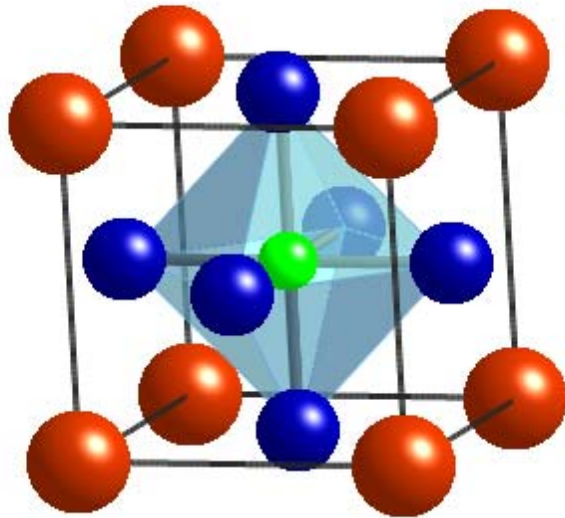


Figure 1-1. Unit cell of a cubic perovskite crystal structure. The A atoms occupy the cell corners (shown in brown), the B atom is in the body center (shown in green), and the O atoms are in the face centers (shown in blue). The BO_3 octahedron is shown in blue.

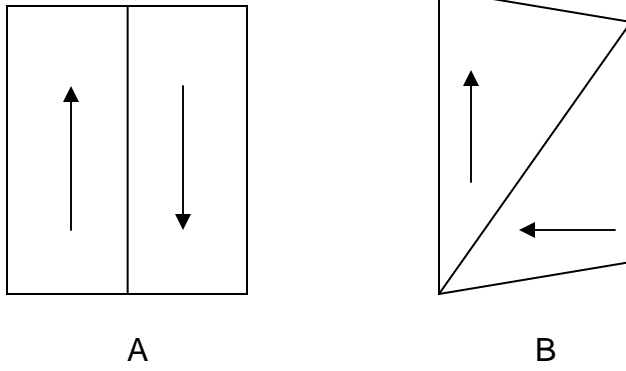


Figure 1-2. Domain variants in ferroelectric ceramics shown as arrangement of polarization axes of adjacent domains. A) 180° domains with antiparallel arrangement of polarization axes, B) non- 180° domains with head-to-tail arrangement of polarization axes at an angle different than 180° (90° in this case).

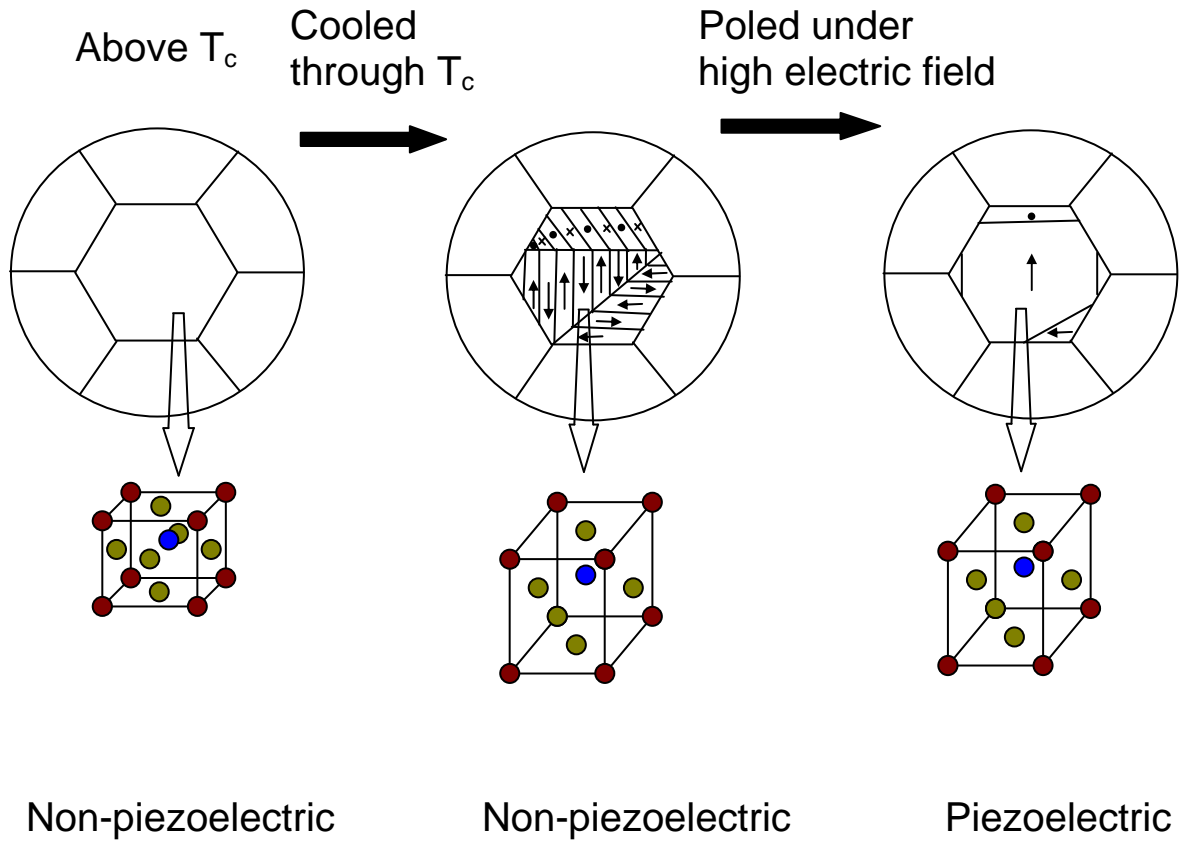
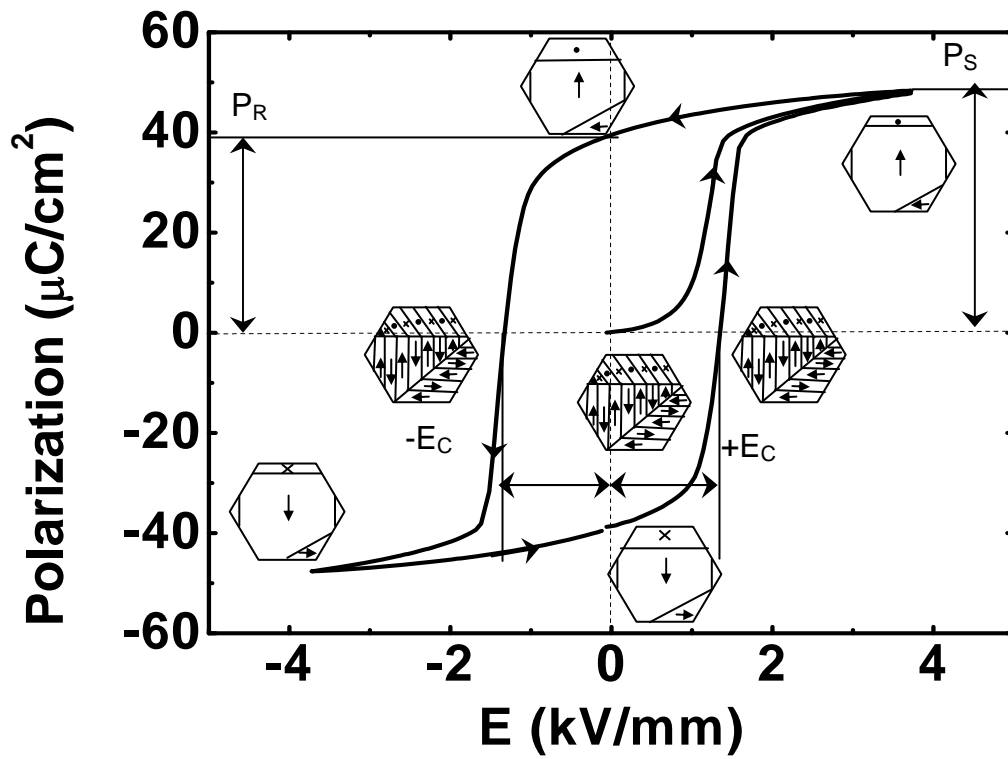
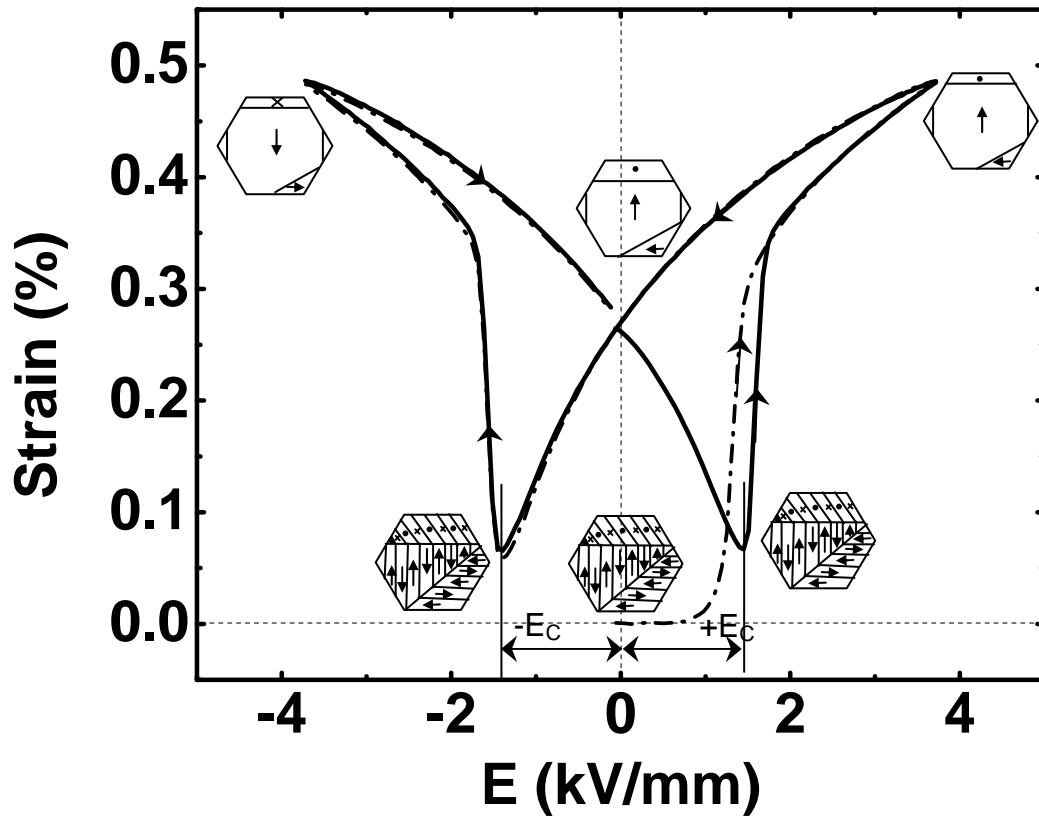


Figure 1-3. The different structural changes in a ferroelectric ceramic from a paraelectric state above T_c to a 'poled' ferroelectric state with reference to a tetragonal crystal structure. The ceramic is piezoelectric after being poled under high electric field.



A

Figure 1-4. The effect of reorientation of domains under applied electric field on A) the polarization, and B) the strain of a piezoelectric ceramic.



B

Figure 1-4 Continued.

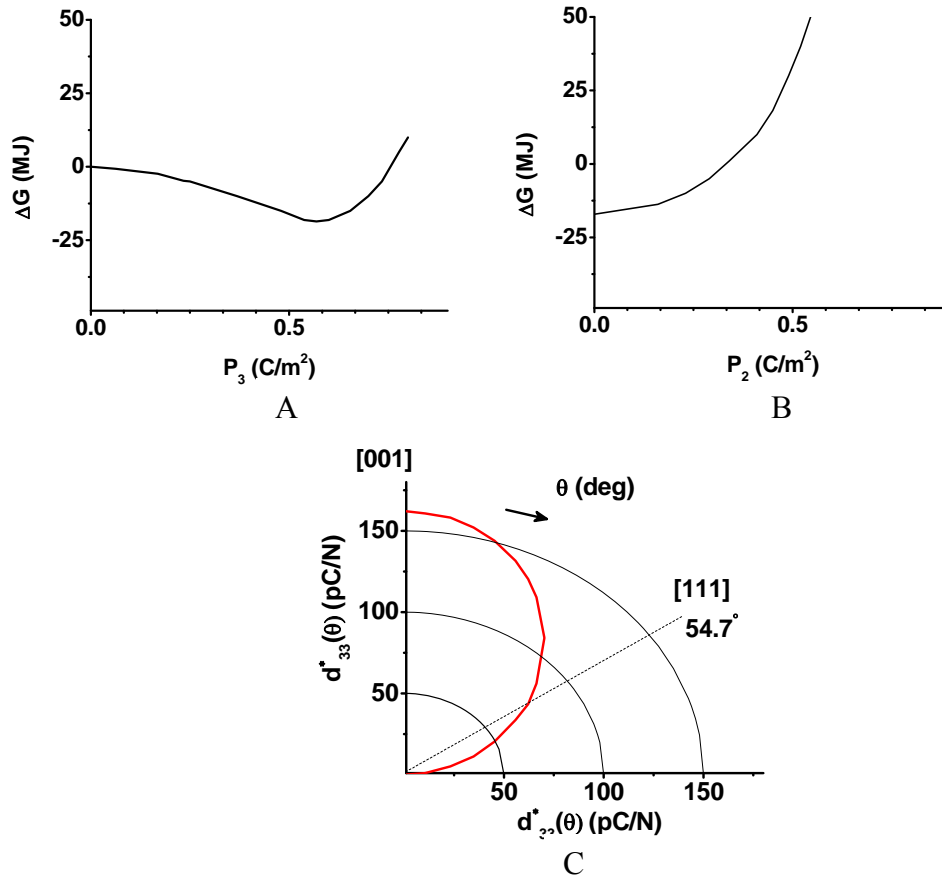


Figure 1-5. The elastic free energy profiles for polarization contraction/elongation and polarization rotation in tetragonal PZT with Zr/Ti ratio of 40/60. A) Free energy profile for elongation or contraction of polarization along the polar axis of [001] ($P_2=0$; $P_3 \neq 0$), and B) Free energy profile for polarization rotation away from the polar axis of [001] ($P_2 \neq 0$; $P_3 = P_3$, P_3 is the equilibrium polarization at 298 K) [from ref. 26].

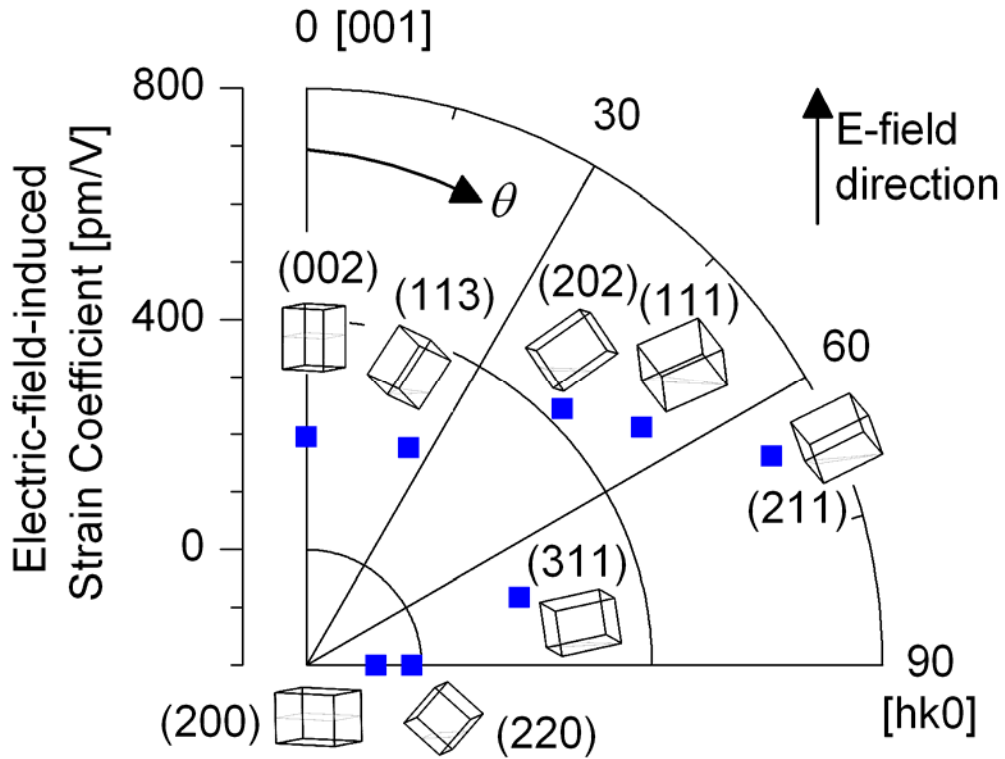


Figure 1-6. The electric-field-induced lattice strain coefficients for different crystal orientations within a polycrystalline tetragonal lead zirconate titanate piezoelectric ceramic under cyclic electric actuation. The tetragonal unit cells in the figure represent the crystallographic orientation of grains and domains in real space, with the (hkl) plane perpendicular to the electric field [from ref.28].

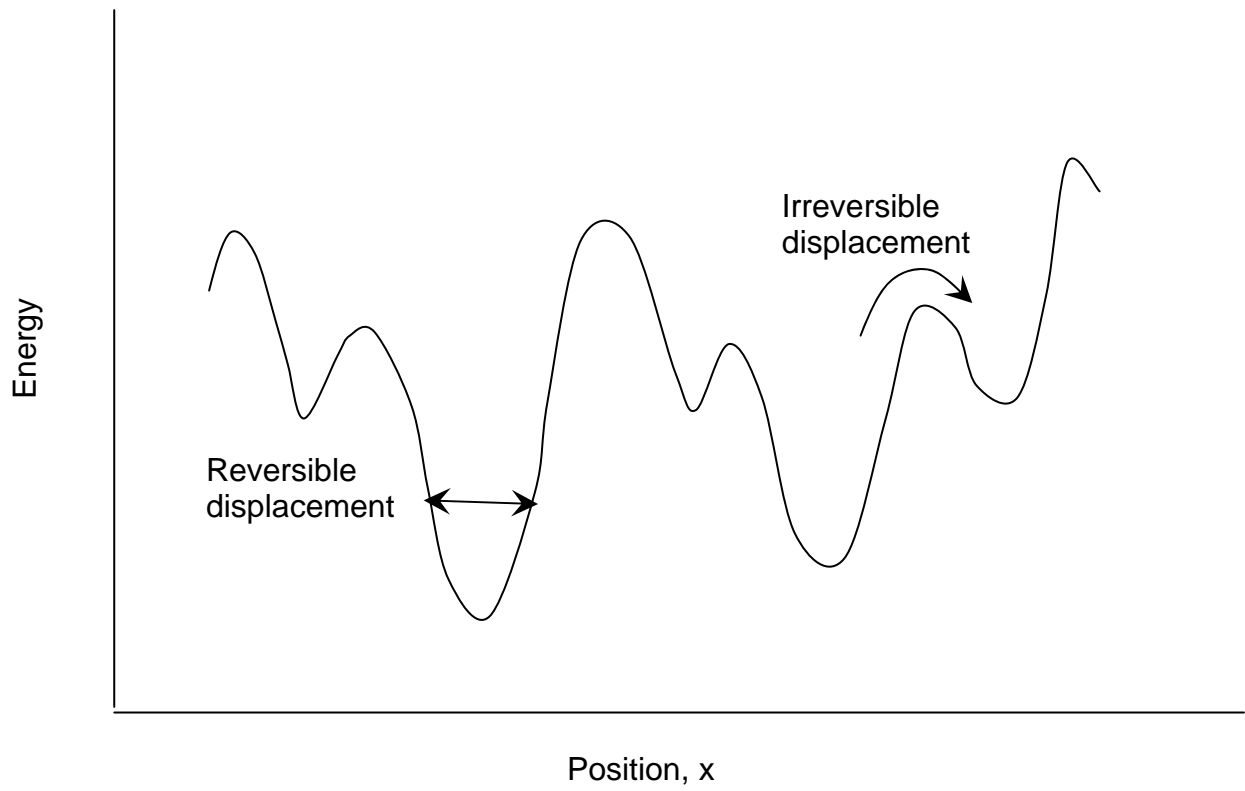
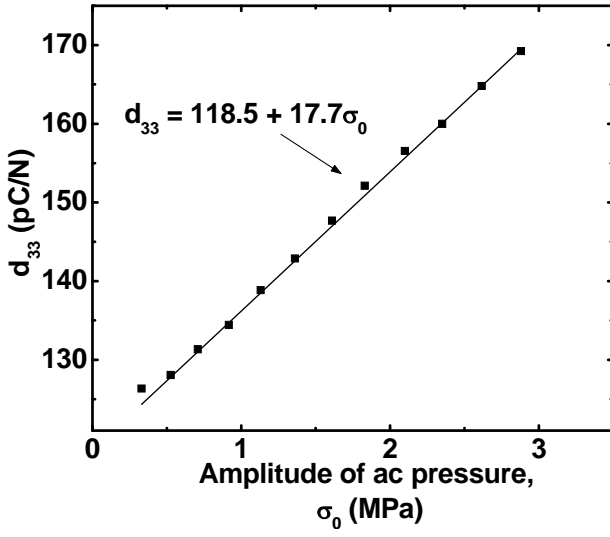
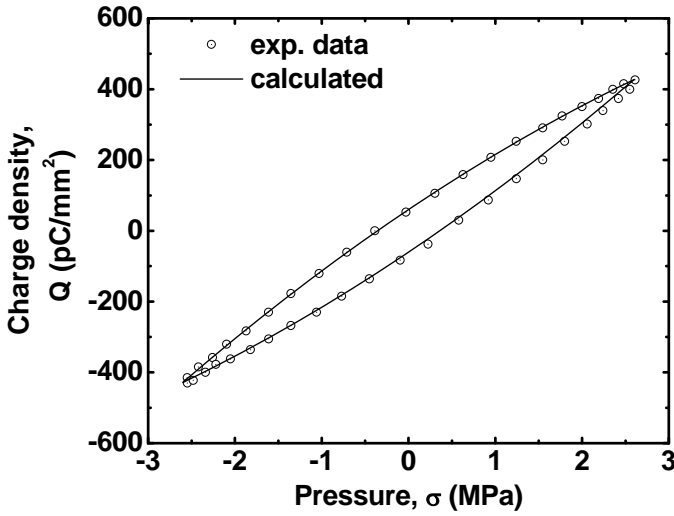


Figure 1-7. Illustration of energy profile for domain wall motion in a medium with random pinning centers



A



B

Figure 1-8. Application of Rayleigh law for direct piezoelectric behavior of 4 atomic % Nb-doped PZT ceramics with Zr/Ti ratio of 63/37. A) Linear variation of the longitudinal piezoelectric d_{33} coefficient with respect to the amplitude of applied a.c. pressure. The d.c. bias pressure is 15 MPa. B) The corresponding hysteresis loop calculated for $\sigma_0 \approx 2.6$ MPa, using Eq. 1-5 [from ref.43].

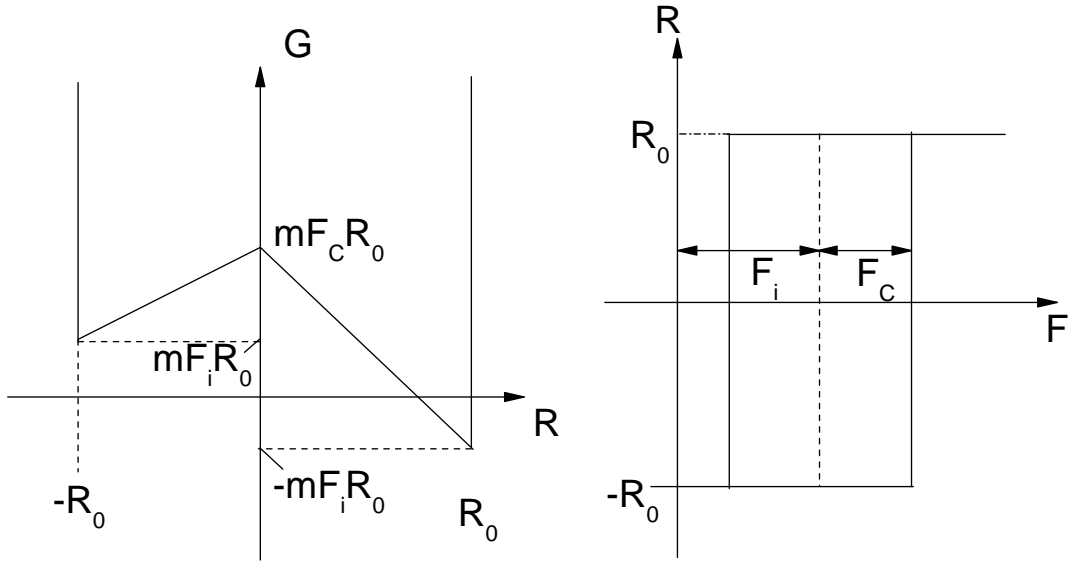
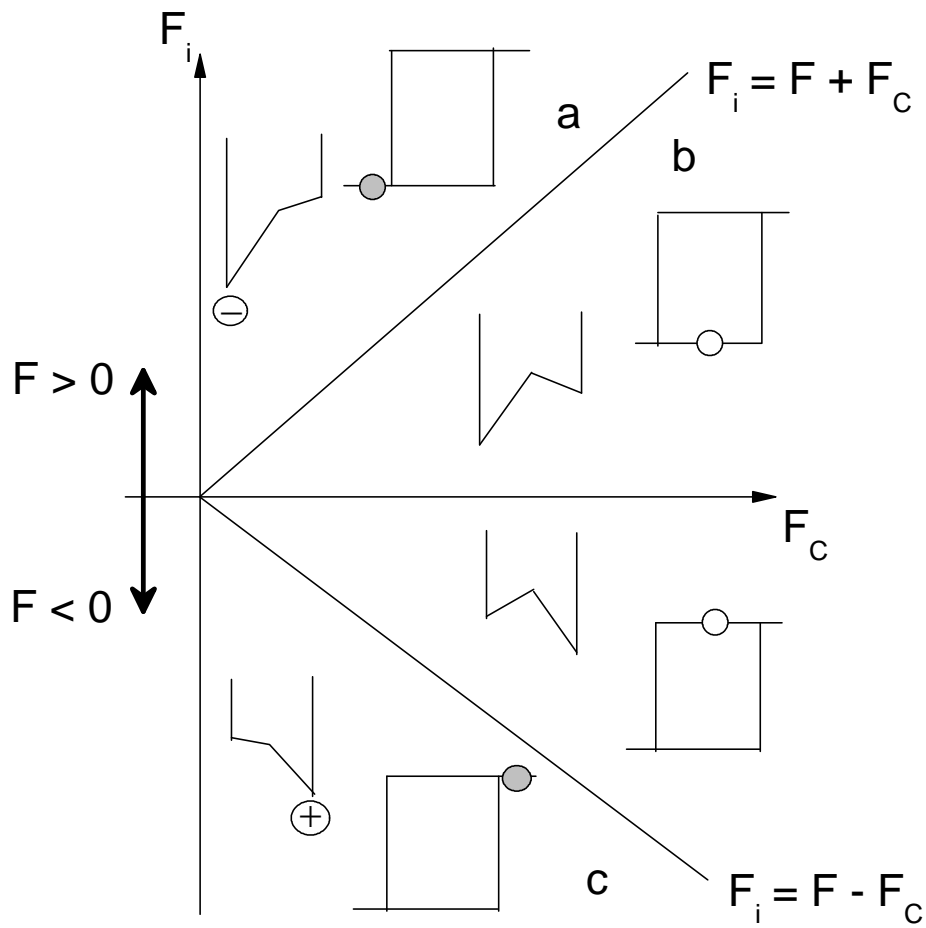
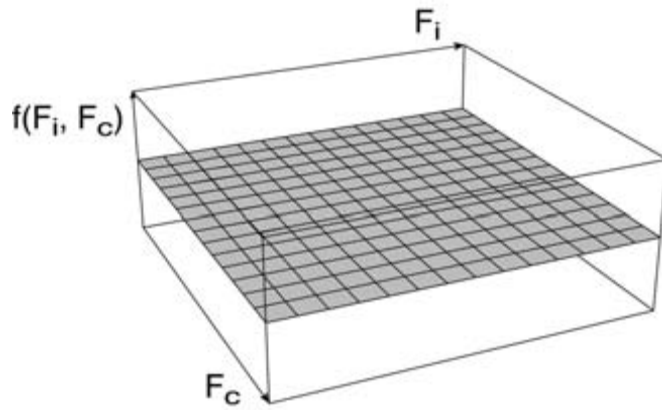


Figure 1-9. Energy profile (left), and square hysteresis (right) of an elementary bistable unit, as assumed in Preisach model for hysteresis. m represents generalized susceptibility [from ref. 4].

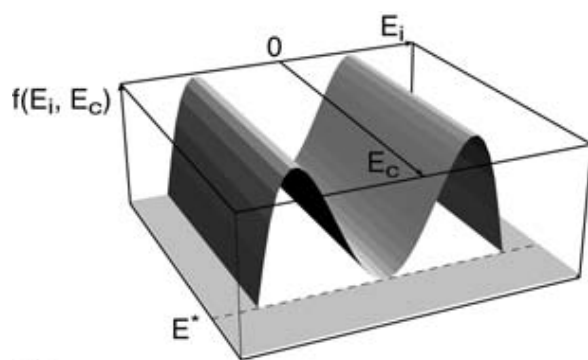


A

Figure 1-10. Energy profile and hysteresis of bistable units as a function of their position on the Preisach plane at zero applied field [from ref. 4].



A



B

Figure 1-11. Preisach distribution function for different characteristic piezoelectric behaviors. A) Flat (uniform) Preisach distribution function corresponding to Rayleigh relations [from ref. 4]. B) Proposed polynomial Preisach distribution function for pinched hysteresis loops as is observed for ferroelectrics containing defect dipoles with two preferred directions. [from ref. 4].

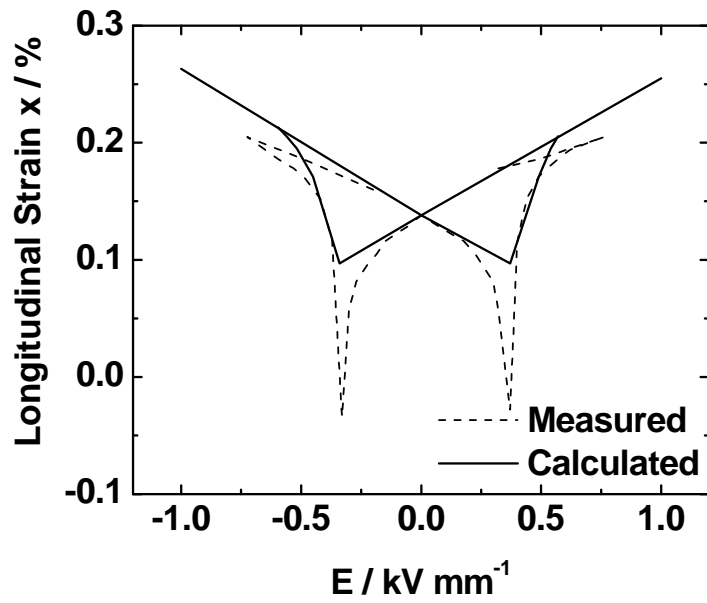


Figure 1-12. Simulated and measured x - E hysteresis loops for La-doped PZT ceramics using micro-mechanical models based on energy criterion for switching, as described in Eq. 1-7 [from ref. 61].

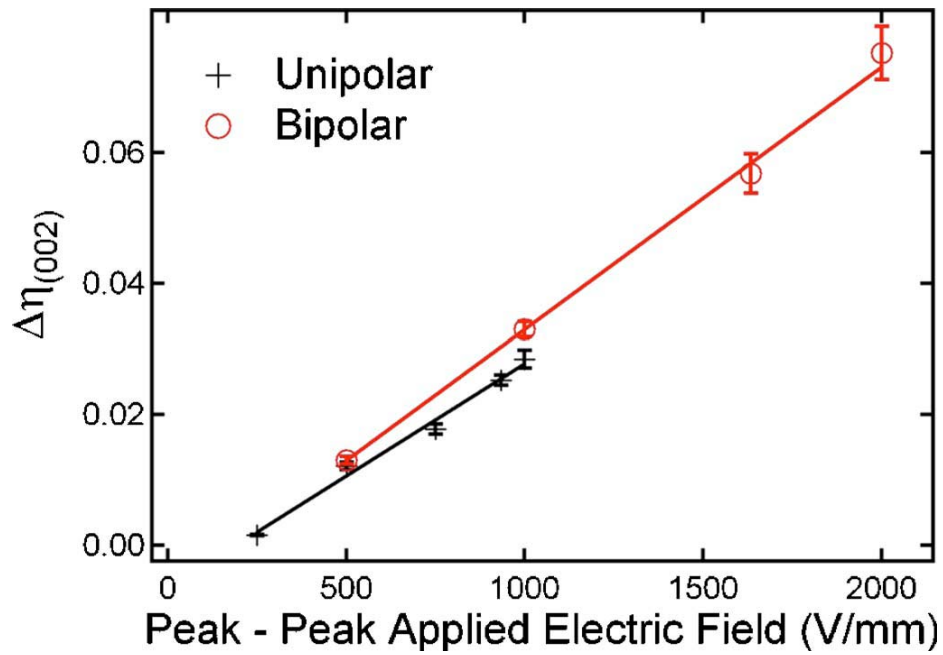


Figure 1-13. Non-180° domain switching fraction ($\Delta\eta_{002}$) in tetragonal PZT ceramics under applied unipolar and bipolar electric fields, as a function of field amplitude [from ref. 73].

CHAPTER 2 OBJECTIVE AND OVERVIEW

As described in Chapter 1, both intrinsic structural mechanisms (such as piezoelectric lattice strains) and extrinsic structural mechanisms (such as displacement of domain walls) can contribute to the overall piezoelectric response in ferroelectric ceramics. Extrinsic structural mechanisms are believed to cause piezoelectric nonlinearity. However, the relative contributions of different extrinsic mechanisms towards macroscopic piezoelectric nonlinearity are currently not well understood.

The objective of this dissertation is to reconcile converse piezoelectric nonlinearity and hysteresis in ferroelectric ceramics with respect to the induced crystallographic and microstructural changes that occur during application of cyclic electric fields. In order to perform such an analysis, measurements of macroscopic piezoelectric properties as well as time-resolved diffraction under the application of cyclic electric fields are performed for ferroelectric PZT ceramics of different compositions (i.e., Zr/Ti ratio) and dopant variants (i.e., undoped, La, and Fe). These various compositions were chosen because they yield different crystal structures and different amounts of domain wall displacements. In order to measure crystallographic and microstructural changes under the application of cyclic electric fields, time-resolved diffraction techniques are developed and utilized at both laboratory and synchrotron X-ray sources.

The layout of the rest of the dissertation is provided below.

Chapter 3 describes the phase diagram of the PZT solid solution and the procedure followed for synthesis of PZT ceramics. The crystallographic phases of the PZT ceramics of different compositions are analyzed from their respective X-ray diffraction patterns. A general description of ferroelectric and piezoelectric properties of the synthesized ceramics is also included.

The nonlinearities and losses in the converse piezoelectric effect of PZT ceramics are presented in Chapter 4. For describing piezoelectric nonlinearity and hysteresis, Rayleigh law is mostly adopted. In addition, complex piezoelectric coefficients are calculated from a Fourier expansion of relations describing piezoelectric hysteresis. It is shown that the separate components of piezoelectric coefficients, from Rayleigh relations and possible viscoelastic mechanisms, can be computed using such an approach.

Measurements of electric-field-induced structural changes under the application of cyclic electric fields are presented in Chapters 5 and 6. Chapter 5 describes the development of a stroboscopic time-resolved diffraction technique for a laboratory diffractometer. This technique is used to measure the structural changes in PZT ceramics under the application of cyclic electric fields. In Chapter 6, a similar structural characterization of PZT ceramics using high-energy X-ray diffraction is presented. High-energy X-ray diffraction in the transmission mode is used to obtain structural information from the bulk of a ceramic in different sample directions. In both Chapters 5 and 6, particular relationships between the measured structural changes and the applied electric field amplitudes are evaluated.

Chapter 7 provides a reconciliation of the macroscopic piezoelectric properties presented in Chapter 4 and the electric-field-induced structural changes presented in Chapters 5 and 6. The relative contributions from non-180° domain switching and lattice distortions towards macroscopic piezoelectric nonlinearity are subsequently evaluated using similar formulations developed in Chapter 4.

A summary of all the results is provided in Chapter 8. The significance and implication of the findings, in the context of piezoelectric properties of ferroelectric ceramics, are discussed. In addition, some potential areas of future investigations are suggested where an approach of

reconciling macroscopic properties with time-resolved structural measurements can provide valuable insights into the material physics of ferroelectrics.

CHAPTER 3 SYNTHESIS OF LEAD ZIRCONATE TITANATE CERAMICS

Lead zirconate titanate (PZT) ceramics are chosen as the model system in this work for investigation of structure-property correlations in piezoelectric ceramics. The solid solution of lead zirconate (PbZrO_3) and lead titanate (PbTiO_3) is a well known ferroelectric system with widespread technological applications [7]. A brief description of the phase diagram of the system is provided here, along with the synthesis procedure followed for producing PZT ceramics with different crystallographic phases and with different dopants.

3.1 Phase Diagram and Dopants for PZT

A portion of the phase diagram for the solid solution of lead zirconate and lead titanate is shown in Figure 3-1. The ratio of mole percentages of PbTiO_3 and PbZrO_3 can be equivalently described in terms of Zr/Ti molar ratio. Depending on the Zr/Ti ratio, a $\text{Pb}(\text{Zr},\text{Ti})\text{O}_3$ solid solution undergoes a specific phase transformation when cooled from its cubic phase to below its Curie temperature (T_C). At room temperature, for compositions $\text{Zr}/\text{Ti} \leq (0.53/0.47)$, a tetragonal phase is observed whereas for compositions $\text{Zr}/\text{Ti} > (0.53/0.47)$, a rhombohedral phase is observed [6]. A monoclinic phase separating tetragonal and rhombohedral regions has been reported in PZT [75]. However, the presence of a monoclinic phase in PZT remains controversial, since the appearance of a monoclinic phase has also been explained by tetragonal/rhombohedral nanodomains [76].

The crystallographic phase of PZT highly influences its piezoelectric properties. For example, Figure 3-1 shows the portion of phase diagram of PZT around MPB and the piezoelectric coefficient d_{33} of PZT bulk ceramics as a function of Zr/Ti ratio at room temperature [6].

For a particular crystallographic phase, the overall piezoelectric response is also influenced by domain wall motion under an applied external field. The contribution from domain wall motion and therefore the total piezoelectric response of a PZT ceramic can be modified by addition of small amounts of impurities or dopants. The displacement of domain walls can be enhanced by substitution of Pb^{2+} or $\text{Zr}^{4+}/\text{Ti}^{4+}$ with dopants of higher valence (donor dopants) like La^{3+} (for Pb^{2+}) and Nb^{5+} (for $\text{Zr}^{4+}/\text{Ti}^{4+}$). Substitution of Pb^{2+} or $\text{Zr}^{4+}/\text{Ti}^{4+}$ with dopants of lower valence (acceptor dopants) like Na^+ (for Pb^{2+}) and Fe^{3+} (for $\text{Zr}^{4+}/\text{Ti}^{4+}$) can restrict the displacement of the domain walls. The effect of the dopants on domain wall displacements is not well understood, however this maybe related to the concentration of oxygen vacancies in the material. While addition of donor dopants reduces the concentration of the existing oxygen vacancies in the system, addition of acceptor dopants creates new oxygen vacancies [6,7].

3.2 Synthesis of PZT Ceramics

Dense ceramics of the following nominal compositions were produced by solid state synthesis route: $\text{Pb}(\text{Zr}_x\text{Ti}_{1-x})\text{O}_3$ (PUZT, undoped) with $x = 0.52$, $\text{Pb}_{1-1.5z}\text{La}_z(\text{Zr}_x\text{Ti}_{1-x})\text{O}_3$ (PLZT, La-doped) with $x = 0.60, 0.52, 0.40$ and $z = 0.02$, and $\text{Pb}_{1+0.5z}[(\text{Zr}_x\text{Ti}_{1-x})_{1-z}\text{Fe}_z]\text{O}_3$ (PFZT, Fe-doped) with $x = 0.47$ and $z = 0.02$. The powders of these compositions were produced by reactive calcination method [24,25] from reagent grade oxides: TiO_2 (Fisher Scientific), ZrO_2 (Alfa-Aesar), PbO (Alfa-Aesar), La_2O_3 (Alfa-Aesar) and Fe_2O_3 (Alfa-Aesar). The stoichiometric amounts of the different oxide reagents for synthesis of the desired final compositions were obtained from their respective chemical formulas. In addition, loss of ignition (LoI) at particular calcination temperatures and purity of the reagent oxides were taken into account while preparing each batch of powder mixtures for further processing. Precursors of compositions $(\text{Zr}_x\text{Ti}_{1-x})\text{O}_2$ and $[(\text{Zr}_x\text{Ti}_{1-x})_{1-z}\text{Fe}_z]\text{O}_2$ were first obtained by ball milling with ZrO_2 milling media in ethanol for at least 12 hours and calcining the stoichiometric mixtures of the oxides at 1300°C

for 4 hours in closed alumina crucibles of volume 10 ml and 40 ml. Stoichiometric amounts of PbO (and La₂O₃ for La-doped compositions) were subsequently mixed with the precursors using ball milling with ZrO₂ milling media in ethanol for at least 12 hours and the mixtures were calcined at 950°C for 2 hours in closed alumina crucibles of volume 10 ml and 40 ml. During the final calcination step, the heating rate was maintained at 10°C/minute. The calcined powders were cooled at a rate of 10°C/minute above 600°C and were subsequently furnace cooled to room temperature. The final PZT powders obtained were ball milled an additional time with ZrO₂ milling media in ethanol for at least 12 hours.

For all ball milling procedures, the powders in batches of about 15-30 grams were added inside a Nalgene jar (500 ml) containing equal volume fractions of spherical ZrO₂ milling media of diameters 5 mm and 10 mm and subsequently about 75-85 ml of ethanol was poured inside the jar. The milling media covered about one-third volume of the Nalgene jar. The milling media was cleaned in de-ionized water subsequent to ball milling powder mixtures each time. Separate Nalgene jars were used for powders of different compositions. Subsequent to ball milling, the slurry was poured into a Polytetrafluoroethylene (PTFE) sheet placed over a glass pan. The glass pan along with the slurry on the PTFE sheet was covered with perforated aluminum sheet and put inside an oven at 100°C for at least 3 hours to vaporize ethanol. The powder obtained from the dried slurry was ground using a porcelain mortar and pestle and the ground powder was sieved through a 212 µm test sieve (Fisher Scientific).

Green pellets were obtained by mixing the powders with organic binder polyvinyl acetate (PVA) using a mortar and pestle (typically 4-5 drops of PVA for 5 grams of PZT) and pressing first uniaxially in 10 mm dies using a force of 3 metric tones (stress of 400 MPa) and then isostatically using 200 MPa. A CARVER 3850 press was used for uniaxial pressing while a

Fluitron press was used for isostatic pressing of pellets; in each batch up to 4 pellets were pressed inside the chamber. For each pellet, approximately 0.5 grams total of the powder and binder blend was used. The green pellets were sintered at 1200°C for 2 hours in a bed of PbZrO_3 + 8 weight % ZrO_2 in a closed alumina circular dish, with a heating/cooling rate of 4°C/minute. During sintering the pellets were covered sufficiently within the bed. The particular composition of the bed is chosen to prevent loss of PbO from the material and to maintain Zr/Ti ratio during sintering. The size of the circular dish used for sintering was 10 ml in volume. The sintered pellets were disc shaped with ~1 mm thickness and were ~8 mm in diameter.

A scanning electron micrograph (JEOL JSM 6400, operating voltage of 15kV) of fracture surface of PLZT5248 is shown in Figure 3-2A. The estimated grain size, based on visual examination, is of the order of 1-2 μm .

The crystallographic phases of the processed ceramics were determined from their respective X-ray diffraction patterns, shown in Figure 3-2B. The crystallographic phase of the sintered ceramics is tetragonal for compositions with $x \leq 0.52$, and rhombohedral for compositions with $x = 0.6$.

The densities of the sintered ceramics were measured using the Archimedeian immersion method. The theoretical densities for the different compositions were calculated from the lattice parameters determined from (002)-type X-ray diffraction peaks. For tetragonal crystal structures, the volume of the unit cell was calculated as (a^2c) where a and c are the interplanar spacings for the (100) and (001) planes, respectively. For rhombohedral crystal structure, the volume of the unit cell was calculated as a^3 , while assuming a pseudocubic structure with a lattice parameter of a . Table 3-1 lists the actual measured densities and the percent theoretical densities for the different samples.

The sintered pellets were polished to a final thickness of 0.75 - 1 mm using SiC grinding papers (Buehler P1200 and P4000). The polished ceramics were subsequently annealed, at 600° C for 2 hours, to relieve surface residual stresses. Gold was deposited, in an Argon atmosphere using a sputter coater, on the top and bottom surfaces of the disc samples in order to get 300-400 nm thick electrodes.

The polarization-electric field and strain-electric field hysteresis loops for the ceramics were measured using a Sawyer-Tower circuit and a linear variable displacement transducer (LVDT), respectively. The applied electric fields were of sinusoidal waveforms with a frequency of 100 mHz. The polarization-electric field and strain-electric field hysteresis loops are shown in Figures 3-3A and 3-3B, respectively. The coercive field (E_C) of ceramics of a particular composition was determined from the macroscopic strain-electric field hysteresis loops. E_C was determined to be equal to the non-zero amplitude of the applied electric field when the field-induced strain is minimum. For samples with a broad minimum for the field-induced strain, E_C was not defined.

The samples were then poled under high electric fields at elevated temperatures using a hot plate and a high voltage power supply. The electric fields used for poling were chosen for the different samples based on data in prior literature regarding poling characteristics of donor- and acceptor-doped ferroelectrics [6-8], experimental trial and error and electrical breakdown strengths. Table 3-2 lists all the materials synthesized for this work, the coercive fields E_C of the samples, the conditions under which they were poled and their direct piezoelectric coefficients measured using an APC International YE2730A Berlincourt meter. The measurements for the piezoelectric measurements were made 24 hours after poling.

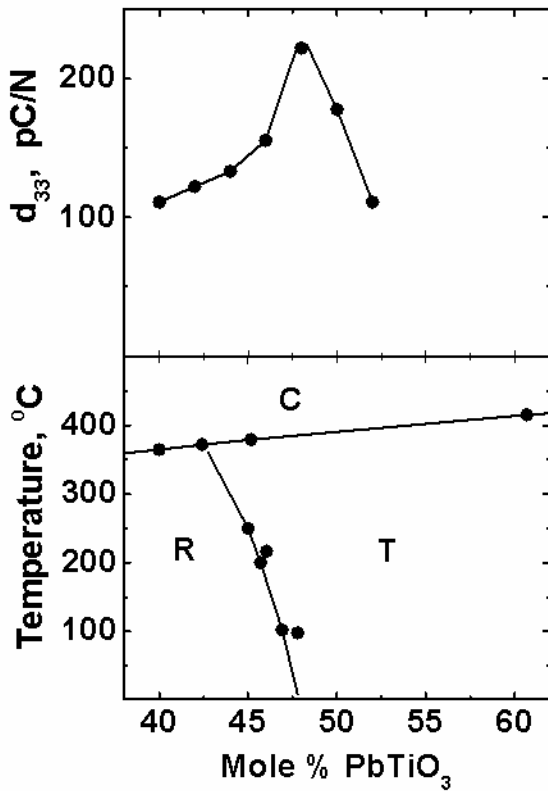
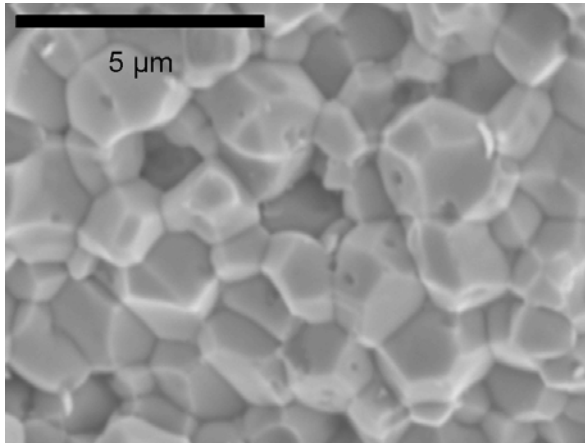
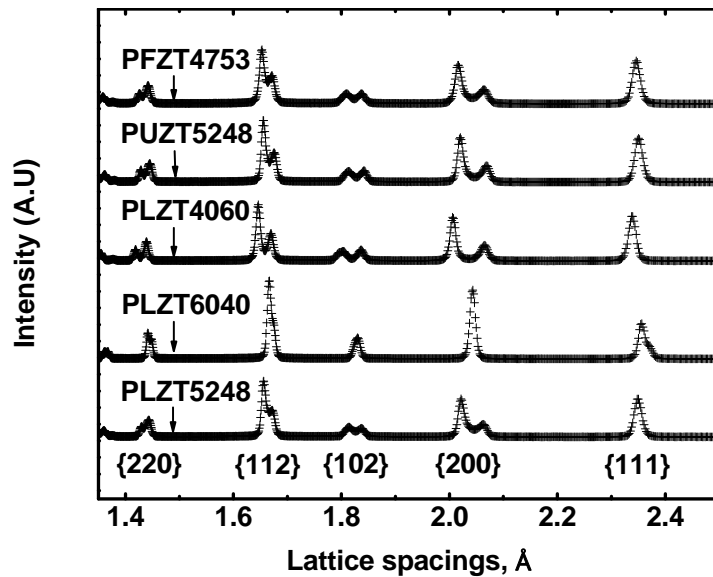


Figure 3-1. Phase diagram and piezoelectric coefficients of PZT ceramics. $\text{PbZrO}_3 - \text{PbTiO}_3$ phase diagram over compositional range close to the morphotropic phase boundary (MPB) is shown in the bottom half of the plot. The MPB for the system is ~ 47 mole % PbTiO_3 ($x=0.53$) at room temperature. The region for the different phases are indicated by the following letters: T (tetragonal), R (rhombohedral) and C (cubic). The plot on the top shows the piezoelectric coefficient d_{33} of undoped PZT ceramics as a function of composition, at room temperature, adapted from Ref. [6].

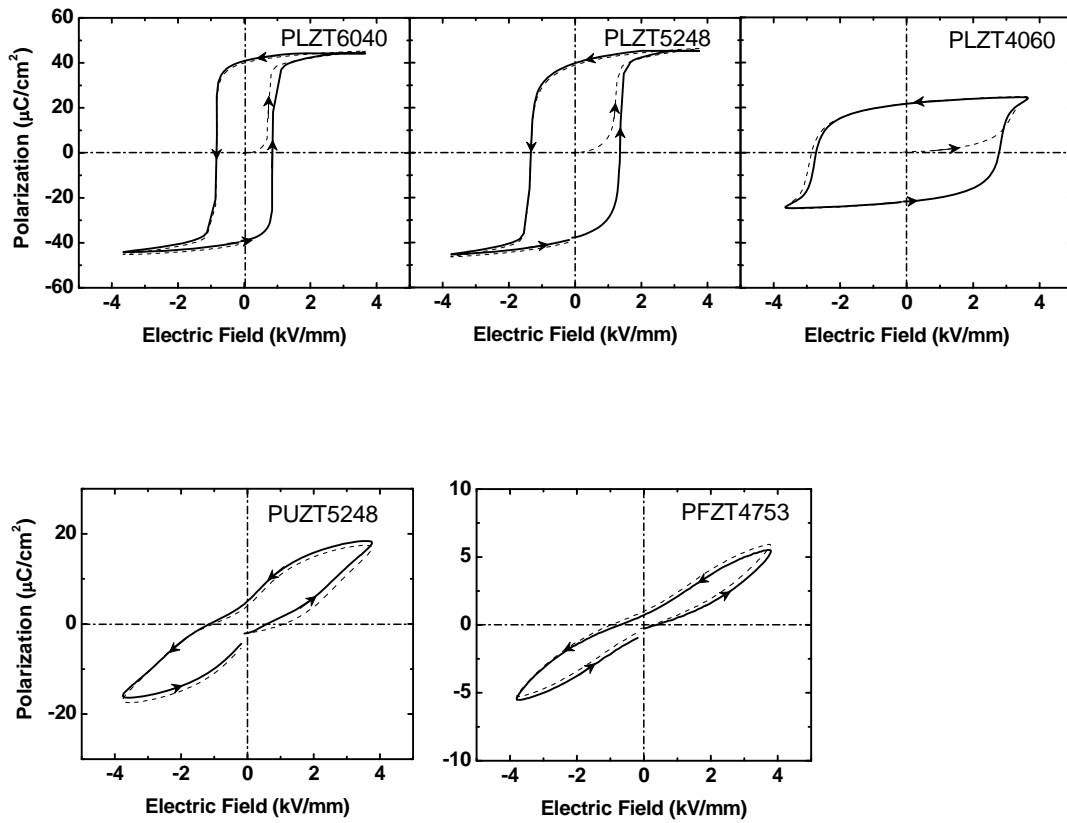


A



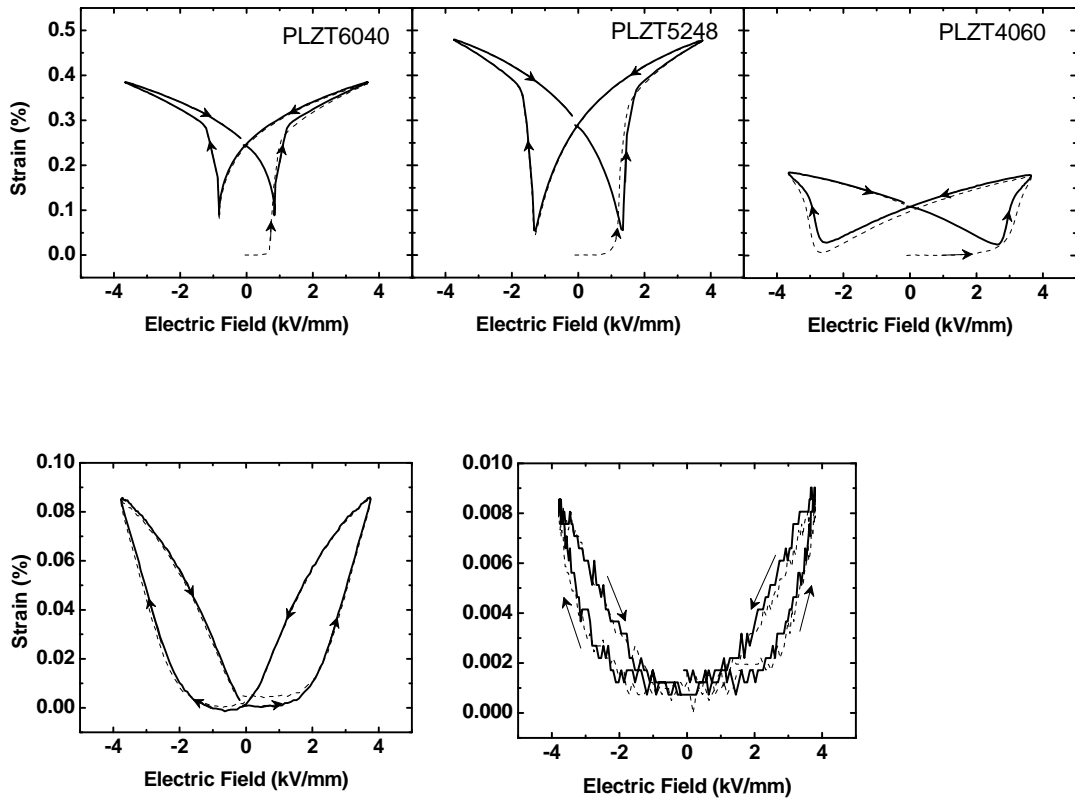
B

Figure 3-2. A) Scanning electron micrograph of fracture surface of PLZT5248; the grain size is of the order of 1-2 μm . B) X-ray diffraction patterns of the sintered ceramics. The different $\{hkl\}$ peaks are consistent with a tetragonal phase for compositions with $\text{Zr}/\text{Ti} \leq 52/48$, and a rhombohedral phase for compositions with Zr/Ti ratio equal to 60/40. The legends for the different ceramic samples are provided in Table 3-1.



A

Figure 3-3. A) Polarization-electric field, and B) strain-electric field hysteresis loops of the various samples. The dotted lines represent polarization/strain measurements for the first applied electric field cycle on an as-sintered ceramic and the solid line represent measurements for subsequent cycles.



B

Figure 3-3. Continued

Table 3-1. The measured densities and the percent theoretical densities for the different samples

Sample notation	Dopants	Zr/Ti ratio	Measured density (g/cm ³)*	Percent theoretical density*
PUZT5248	Undoped	52/48	7.64 (±0.05)	95.7 (±0.66)
PLZT6040	2 at. % La-doped	60/40	7.72 (±0.03)	97.1 (±0.43)
PLZT5248	2 at. % La-doped	52/48	7.77 (±0.04)	97.1 (±0.50)
PLZT4060	2 at. % La-doped	40/60	7.62 (±0.08)	95.3 (±1.00)
PFZT4753	2 at. % Fe-doped	47/53	7.81 (±0.02)	97.8 (±0.20)

* The numbers in the braces indicate the standard deviation for the reported values. The standard deviation for each composition was calculated from the densities measured on three different samples of the same composition.

Table 3-2. List of the samples used for experiments in this work. The d_{33} values were measured using a Berlincourt-type d_{33} meter.

Sample notation	Coercive field, E_C	Poling conditions	d_{33} (pC/N)
PUZT5248	not defined	4 kV/mm at 100° C for 60minutes	180
PLZT6040	~ 0.85 kV/mm	3.5 kV/mm at 50° C for 15minutes	208
PLZT5248	~ 1.35 kV/mm	3.5 kV/mm at 50° C for 15minutes	480
PLZT4060	~ 2.6 kV/mm	3.5 kV/mm at 50° C for 15minutes	130
PFZT4753	not defined	4 kV/mm at 100° C for 60minutes	204

CHAPTER 4 NONLINEARITIES AND LOSSES IN CONVERSE PIEZOELECTRIC EFFECT OF PZT CERAMICS

Converse piezoelectric response of $\text{Pb}(\text{Zr}_x\text{Ti}_{1-x})\text{O}_3$ ceramics is investigated as a function of material composition. The effects of crystallographic phase and different dopants on piezoelectric nonlinearity are separately examined. For a linear dependence of d_{33} on E_0 , Rayleigh law is applied to describe the material behavior. The observed piezoelectric nonlinearities are described in terms of contributions from extrinsic mechanisms. The effect of piezoelectric nonlinearities on strain-electric field hysteresis is subsequently examined. In order to calculate the complex piezoelectric coefficients, a method based on Fourier expansion of the Rayleigh relations is adopted. Finally, a description of first and higher order harmonics is used to show that Rayleigh component is dominant in the overall piezoelectric strain of the material.

4.1 Experimental Procedure

4.1.1 Converse Piezoelectric Measurements

The experimental setup for converse piezoelectric measurements under cyclic electric fields is shown in Figure 4-1. A Trek 609C-6 high-voltage amplifier driven by a Stanford Research System DS360 function generator was used to apply sinusoidal electric fields of frequency 1 Hz across the thickness of a ceramic sample. The expansion and contraction of the sample along the direction of the applied electric field was measured by detecting the vertical displacement of the sample surface using a MTI 2000 photonic sensor. The signals from the function generator and the photonic sensor were measured with a Tektronix TDS410 oscilloscope connected to a computer. Acquisition of the measured signals on the oscilloscope was performed using a National Instruments Labview program. Figure 4-2 shows a typical strain-electric field hysteresis loop obtained using this experimental setup. The longitudinal

piezoelectric coefficient d_{33} was calculated from the strain-electric field hysteresis loop using the following equation:

$$d_{33} = \frac{x_{max}}{2E_0}, \quad (4-1)$$

where x_{max} is the peak-to-peak longitudinal measured strain and E_0 is the amplitude of the applied bipolar electric field $\pm E_0$ parallel to the direction of the measured strain. This is illustrated in Figure 4-2. Since only this coefficient was measured in the present work, d_{33} and d are used interchangeably throughout this dissertation.

In order to determine the electric field dependence of the piezoelectric coefficient d_{33} , the amplitude of the applied electric field E_0 was steadily increased after each successive measurement. The maximum value of E_0 was limited to below the macroscopic coercive field of the sample, E_C .

4.1.2 Application of Rayleigh Law

The following Rayleigh relations have been previously observed to satisfactorily describe the linear dependence of converse longitudinal piezoelectric coefficients in certain ferroelectric ceramics:

$$d(E_0) = d_{init} + \alpha_d E_0, \quad (4-2)$$

$$x = (d_{init} + \alpha_d E_0)E \pm \frac{\alpha_d}{2}(E_0^2 - E^2), \quad (4-3)$$

where d_{init} is the piezoelectric coefficient at the limit of zero applied field amplitude E_0 , x is the measured macroscopic strain response under applied field E , and α_d describes the linear dependence of the piezoelectric coefficient d on the amplitude of the applied field E_0 [46,47]. In effect, d_{init} is the contribution to the piezoelectric coefficient from intrinsic lattice strains and reversible domain wall displacements, and $\alpha_d E_0$ is the contribution originating from the

irreversible displacement of domain walls. Relations similar to Eqs. 4-2 and 4-3 have also been used to describe the direct piezoelectric effect [42,43].

The applicability of the Rayleigh relations, Eqs. 4-2 and 4-3, was investigated for the longitudinal converse piezoelectric properties of all the measured data. The fractional contribution to piezoelectric nonlinearity from irreversible extrinsic mechanisms was calculated as $\Delta d_{33}/d_{33}(E_0)$, where $d_{33}(E_0)$ is the measured piezoelectric coefficient at electric field amplitude E_0 . For materials which were observed to follow Rayleigh law, Δd_{33} was calculated as $[d_{33}(E_0) - d_{init}]$; otherwise Δd_{33} was calculated as $[d_{33}(E_0) - d_{33,min}]$, where $d_{33,min}$ is the piezoelectric coefficient measured for applied electric field of lowest amplitude. Δd_{33} is expected to be equal to $\alpha_d E_0$ when Rayleigh behavior is followed.

4.1.3 Calculation of Piezoelectric Losses and Complex Coefficients

The operation of piezoelectric ceramics under cyclic electric fields of amplitude $0 < E_0 < E_C$ can involve significant energy dissipation. The total energy dissipation or piezoelectric loss per unit volume of the material can be correlated to the total area of the piezoelectric strain-field hysteresis loop [4]. The total area of the strain-electric field hysteresis loop and the various contributing factors are calculated following the method described in reference [3]. For a material that follows Rayleigh law, the hysteresis area A_R can be calculated from the integral of the hysteresis loop as predicted by the Rayleigh relation Eq. 4-3,

$$A_R = \oint_{cycle} dE = \frac{4\alpha_d E_0^3}{3}. \quad (4-4)$$

However, in reality there can be additional non-Rayleigh contributions to the total area of the strain-electric field hysteresis loop from the generalized susceptibility of the material [80]. For the converse piezoelectric effect, this additional contribution can be present due to the linear viscoelastic component of domain wall motion which is not represented in the Rayleigh law.

The response of a linear viscoelastic system with a certain phase lag δ , under the application of a sinusoidal electric field $E = E_0 \sin(\omega t)$, can be described by

$$x = x_0 \sin(\omega t - \delta), \quad (4-5)$$

where x_0 is the amplitude of the piezoelectric strain response of the system. The piezoelectric coefficient d_{lin} of this system can be represented as a complex variable

$$d_{lin}^* = d_{lin}' - i d_{lin}'', \quad (4-6)$$

where d' and d'' are respectively the real and imaginary components and d^* is the modulus of the complex piezoelectric coefficient. The hysteresis area for such a system A_{lin} is given by the integral of Eq. 4-5,

$$A_{lin} = \oint_{cycle} dE = \pi x_0 E_0 \sin \delta = \pi d_{lin}'' E_0^2. \quad (4-7)$$

The total area of strain-electric field hysteresis loop of a nonlinear viscoelastic piezoelectric material can therefore be represented as a sum of the areas contributed due to Rayleigh-type nonlinearity and due to linear viscoelastic effects,

$$A_{total} = A_R + A_{lin}. \quad (4-8)$$

Eq. 4-8 is valid if there is no coupling between the different loss contributions. This is a reasonable first approximation and has been previously made in magnetic materials [51]. The application of this equation in present work is an assumption, but does not significantly affect the conclusions drawn in this dissertation.

The different contributions to the overall electric-field-induced response of a material can also be identified from the real and imaginary components of its complex piezoelectric coefficient. The real and imaginary components of piezoelectric coefficient of a material that follows Rayleigh law, can be identified from a Fourier expansion of Eq. 4-3 for $E = E_0 \sin(\omega t)$

$$x(t) = (d_{ini} + \alpha_d E_0) E_0 \sin(\omega t) - \frac{4\alpha_d E_0^2}{3\pi} \cos(\omega t) - \frac{4\alpha_d E_0^2}{3\pi} \left[\frac{1}{5} \cos(3\omega t) - \frac{1}{35} \cos(5\omega t) + \dots \right]. \quad (4-9)$$

By combining Eqs. 4-5 and 4-9, the total strain of a nonlinear piezoelectric under the application of electric field $E = E_0 \sin(\omega t)$ can be expressed as

$$x(t) = [d'_R(E_0)] E_0 \sin(\omega t) - [d''_R(E_0)] E_0 \cos(\omega t) - [d''_{lin}(E_0)] E_0 \cos(\omega t) + \dots, \quad (4-10)$$

where d'_R and d''_R are the real and the imaginary components of the piezoelectric coefficient of an ideal Rayleigh system, respectively, and d''_{lin} is the imaginary component of the viscoelastic susceptibility of the material.

The terms in Eq. 4-10 associated with an ideal piezoelectric material following Rayleigh law can be compared with the corresponding terms in Eq. 4-9. If the first harmonic component in Eq. 4-9 is over an order of magnitude greater than the higher order harmonics, we may further assume that the higher order harmonics are relatively insignificant in the description of the complex piezoelectric coefficients and therefore can be neglected. We can then arrive at the following relations

$$\begin{aligned} d'_R(E_0) &= (d_{ini} + \alpha_d E_0), \\ d''_R(E_0) &= \frac{4\alpha_d E_0}{3\pi}. \end{aligned} \quad (4-11)$$

A summary of the data analysis routine is described below. The piezoelectric coefficient $d'_R(E_0)$ is calculated from the peak-to-peak amplitude of the measured strain-electric field hysteresis loop at electric field amplitude E_0 , as shown in Figure 4-2. The Rayleigh coefficient α_d is obtained from a linear fit of multiple measurements of $d'_R(E_0)$ at several the electric field amplitudes E_0 . The area of the strain-electric field hysteresis loop for an ideal Rayleigh type response is then calculated using Eq. 4-4 and the complex coefficient associated with Rayleigh

behavior is given by Eq. 4-11. The area associated with viscoelastic nature of the material deformation, A_{lin} is obtained from the difference between the area of the experimental hysteresis loop and the area predicted by Eq. 4-4. The imaginary component of the viscoelastic susceptibility of the material at electric field amplitude E_0 is obtained using Eq. 4-7 as

$$d''_{lin} = \frac{A_{lin}}{\pi E_0^2}. \quad (4-12)$$

Note that since A_R is proportional to E_0^3 and A_{lin} is proportional to E_0^2 , a distinction between the contributions of each to the overall strain-electric field hysteresis area can be obtained.

4.1.4 Measurement of the Harmonic Components of Converse Piezoelectric Strain

The other essential characteristics of a material system following Rayleigh law can be identified from Eq. 4-9 [4]. First, it can be observed that the Fourier expansion of the Rayleigh law for a sinusoidal electric field contains only odd harmonics. Further, the amplitude of the third and higher harmonics should be proportional to the square of the amplitude of the applied electric field. Moreover, since the third and all other higher harmonics have no component in phase with the applied electric field, their phase angle should be $\pm 90^\circ$ for ideal Rayleigh behavior. For such an ideal Rayleigh behavior, every domain wall displacement needs to be hysteretic as well as also contribute to a linear increase in piezoelectric coefficient with applied electric field amplitude. All of the above features of Rayleigh-type behavior can therefore be experimentally verified from the measured piezoelectric strains.

In order to measure the harmonics, the electronic signals from the photonic sensor were measured using a Stanford Research System SR830 lock-in amplifier. The amplitude and phase of the first, second and third harmonics of the piezoelectric strain were measured under sinusoidal electric fields and are presented in the section 4.2.3.

4.2 Results and Discussion

4.2.1 Piezoelectric Nonlinearity and Application of Rayleigh Law

The piezoelectric coefficients measured at increasing amplitudes of subcoercive cyclic electric fields for the ceramic materials listed in Table 3-1 are presented in this section.

4.2.1.1 Effect of crystal structure on nonlinear behavior

Figure 4-3 shows the measured converse piezoelectric coefficients d_{33} of 2 at% La-doped PZT ceramic samples identified as PLZT6040, PLZT5248 and PLZT4060. The piezoelectric coefficients of all the three compositions show linear dependence on the amplitude of the applied electric field over a wide range, as indicated in Figure 4-3. Eq. 4-2 is therefore applied to describe the converse piezoelectric coefficients under subcoercive electric fields for these materials. The value of the parameter α_d is ~ 0.43 , ~ 0.36 , and ~ 0.07 (pm/V)(V/mm) $^{-1}$ for PLZT5248, PLZT6040 and PLZT4060 respectively. [The unit of (pm/V)(V/mm) $^{-1}$ is equivalent to 10^{-15} m 2 /V 2]. The linear increase in the piezoelectric coefficients can be explained by irreversible motion of non-180° domain walls in a medium with randomly distributed pinning centers [44]. In a polycrystalline ceramic, these pinning centers can be point defects such as vacancies or line defects such as dislocations. La-doping is generally understood to promote the displacement of the non-180° domain walls [6,7]. With increasing amplitude of applied electric fields, motion of the domain walls is increasingly promoted and therefore higher contributions from domain wall motion to the macroscopic field-induced strains are made. While non-180° domain wall displacement may be the dominant influencing factor for the increase in piezoelectric coefficient with increasing electric field amplitude, other extrinsic contributing factors cannot be ruled out. This includes 180° domain wall motion through dynamic poling [81] and nonlinear misfit lattice strains arising due to non-180° domain wall displacement in neighboring grains [30].

In order to estimate the absolute and the fractional amounts of irreversible extrinsic contributions to the total electric-field-induced strain, the factor Δd_{33} and the ratio $\Delta d_{33}/d_{33}(E_0)$ are calculated for all samples. The values are plotted in Figure 4-4A and Figure 4-4B. The amount of irreversible extrinsic contribution can be seen to steadily increase with the amplitude of the electric field. The largest fractional extrinsic contribution is found to be about 55% for La-doped rhombohedral PZT ceramics, for an applied electric field amplitude of ± 750 V/mm. For all amplitudes of applied electric fields, the largest and smallest fractions of irreversible extrinsic contributions are observed for the rhombohedral PLZT6040 and the tetragonal PLZT4060 samples, respectively. The difference in irreversible extrinsic contributions for the different samples can be interpreted in terms of strain contributions due to non-180° domain wall displacement in the material.

For the rhombohedral phase the number of possible spontaneous ferroelastic distortions is 4 whereas in tetragonal phase this number is 3. In other words, more alternate ferroelastic states are available for domains with non-180° domain walls in the rhombohedral phase as compared to the tetragonal phase. This may imply comparatively greater possible non-180° domain wall motion in the rhombohedral phase. However, the amount of strain created due to non-180° domain wall motion will also depend on the spontaneous strain associated with a rhombohedral or tetragonal ferroelastic distortion, which can be determined from crystallographic lattice parameters. The specific lattice spacings of the different ceramics were determined from their respective X-ray diffraction patterns. In the rhombohedral phase, the spontaneous strain is defined by the ratio of the lattice spacings $d_{111}/d_{1\bar{1}\bar{1}}$ which is equal to 1.0068(1) for PLZT6040. In the tetragonal phase, the spontaneous strain is defined by the ratio of the lattice spacings d_{002}/d_{200} which are equal to 1.0209(1) and 1.0290(1) for PLZT5248 and PLZT4060,

respectively. The values for $d_{111}/d_{\bar{1}\bar{1}\bar{1}}$ and d_{002}/d_{200} were calculated from the position of the (111)-type and the (002)-type diffraction peaks of these ceramics, as presented in Figure 3-2B. Therefore the same amount of non-180° domain wall displacement in the tetragonal phase would create a greater strain as compared to a rhombohedral phase. The observed trends in Figure 4-4A and Figure 4-4B are therefore contributed by both factors discussed here, namely amount of non-180° domain wall motion and spontaneous strains. Further elaboration on this point will be provided in Chapter 6.

Since the rhombohedral phase with the smallest spontaneous distortion shows relatively higher values of extrinsic contributions, a high degree of non-180° domain wall motion in this material is implied. Among the samples with a tetragonal phase, PLZT5248 shows high degree of extrinsic contributions as compared to PLZT4060. This trend when interpreted in conjunction with the fact that PLZT4060 has a higher spontaneous strain than PLZT5248 would indicate comparatively less amount of non-180° domain wall displacement in PLZT4060. This can be explained due to greater clamping of 90° domain walls due to internal stresses caused by high spontaneous distortion in PLZT4060 ($d_{002}/d_{200} = 1.0290$) as compared to PLZT5248 ($d_{002}/d_{200} = 1.0209$). Another possible interpretation for this effect could be lower domain wall energies in materials with compositions near the MPB [82], which makes domain wall displacement easier in PLZT5248 as compared to PLZT4060. Additional improvements in micromechanical models [61,62] can help to understand the predominance of either of the above listed mechanisms.

4.2.1.2 Effect of dopants on nonlinear behavior

As indicated in Chapter 3, the domain wall displacements are known to be highly influenced by the addition of dopants. While addition of La as a donor dopant is known to enhance the displacement of the domain walls, addition of Fe as an acceptor dopant is known to

have an opposite effect [6,7]. The influence of dopants on the amount of irreversible extrinsic contributions to the converse piezoelectric strain for tetragonal PZT ceramics with compositions close to the MPB is discussed in this section.

Figure 4-5A shows the field dependent converse piezoelectric coefficients of PZT ceramics with compositions slightly on the tetragonal side of the MPB. It is observed that for MPB-adjacent tetragonal phases the piezoelectric coefficients show drastic increase with the addition of La. Though both undoped and La-doped compositions can be seen to follow Rayleigh type behavior, there is more than a three-fold increase in the Rayleigh coefficient α_d with La-doping and consequently an increase in the amount of extrinsic contributions. For MPB-adjacent tetragonal PZT ceramics, irreversible extrinsic contributions for the highest applied electric field amplitudes increases from ~25% in undoped composition to ~45% in La-doped compositions (Figure 4-5B). For Fe-doped compositions, dependence of the piezoelectric coefficient on the amplitude of the electric field is not described by Rayleigh law. The fraction of irreversible extrinsic contributions, calculated from $[d_{33}(E_0) - d_{33,\min}]$, is a maximum of ~8% at the highest applied electric field amplitude for Fe-doped MPB-adjacent tetragonal ceramics. The effect of dopants on the irreversible extrinsic contributions is therefore clearly noted for piezoelectric ceramics with similar crystallographic phases.

4.2.1.3 Prediction of piezoelectric hysteresis from Rayleigh relations

As indicated in section 4.1.2, the strain-electric field hysteresis loops at subcoercive electric fields can be calculated using the second Rayleigh relation, Eq. 4-3. The measured hysteresis loops were compared with the hysteresis loops calculated using Eq. 4-3 for undoped and La-doped PZT ceramics. Measured and calculated hysteresis loops for La-doped and undoped PZT ceramics are presented in Figure 4-6 as examples. For Fe-doped PZT ceramics, no significant hysteresis was observed.

4.2.2 Piezoelectric Losses and Complex Coefficients

The method for calculating the different contributions to the overall piezoelectric losses, as described in section 4.1.3, is applied here for the sample PLZT5248. The areas of the measured strain-electric field hysteresis loops at different amplitudes were obtained using numerical integration and are shown in Figure 4-7A. The linear slope of the log-log plot of the measured areas with respect to the electric field amplitude should be 3 for a nonlinear piezoelectric material following Rayleigh law, according to Eq. 4-4. However, this slope is approximately 2.84 for the experimentally determined hysteresis areas. The differences between the measured hysteresis areas and the calculated areas in this case can arise from additional non-Rayleigh mechanisms for domain wall motion. One such possible non-Rayleigh mechanism can be viscoelastic motion of domain walls, as described in section 4.1.3.

The differences between the measured hysteresis areas and the calculated areas from Eq. 4-4 are shown by the square data points in Figure 4-7A. The best fit for the square data points with respect to field amplitudes is obtained with a linear slope of 1.7 ± 0.3 on a log-log plot. If we assume that the non-Rayleigh contribution to the hysteresis area comes solely from a linear viscoelastic process, the slope of the difference plot should be equal to 2 according to Eq. 4-7. The observed non-Rayleigh contributions to the hysteresis area could deviate from the predictions of Eq. 4-7 due to additional non-Rayleigh mechanisms that are not described by a linear viscoelastic process. Nevertheless, it can be observed that additional mechanisms, not described by Rayleigh law, contribute to the total piezoelectric hysteresis in the material. However, at field amplitudes > 650 V/mm the measured hysteresis areas closely correspond to the predictions of Eq. 4-4 which implies that Rayleigh type nonlinearity becomes more dominant at higher amplitudes of applied electric field.

In order to calculate the complex piezoelectric coefficients of this material, Eq. 4-11 is applied. This is justified by the general observation that the component of the first order harmonic is two orders of magnitude higher than the second and third order harmonics, as presented in the following section 4.2.3. The imaginary piezoelectric coefficient associated with Rayleigh-type nonlinearity, d_R'' , is plotted as a function of electric field amplitude in Figure 4-7B. In order to make an estimate of the imaginary piezoelectric coefficients associated with non-Rayleigh processes, Eq. 4-12 is applied while assuming that the non-Rayleigh losses can be described mostly by a linear viscoelastic process. The average value for the coefficient d_{lin}'' , calculated from the difference plot of Figure 4-7A and using Eq. 4-12, is observed to be 6.5 pm/V. The calculated average value for d_{lin}'' is one order of magnitude less than the estimated values of d_R'' , particularly for $E_0 > 500$ V/mm. Since $d_{lin}'' \ll d_R''$ for moderate to high amplitudes of applied electric field, it is therefore concluded that approximate values of the complex piezoelectric coefficients can be calculated using Eq. 4-11 under such conditions. It should be noted from the above discussion that d_{lin}'' can be disregarded in the description of complex piezoelectric coefficients, only if a Rayleigh-type nonlinear process is the dominating mechanism for the overall electric-field-induced strain.

4.2.3 Harmonics of the Converse Piezoelectric Strain

In this work, the harmonics are measured only for the sample PLZT5248 which has the highest piezoelectric coefficients. General agreement between nonlinearity and hysteresis in other samples are noted and further investigation into the harmonic components of their strain responses was not undertaken.

The amplitudes and the phase angles of the first three harmonics of the converse piezoelectric strains for sample PLZT5248 at three different electric field amplitudes are listed in Table 4-1. The most dominant is the first harmonic with phase angle close to 0° . The third

harmonic is proportional to the square of the amplitude of the applied electric field and has a phase angle $\sim 75^\circ$. This is different from 90° as predicted for ideal Rayleigh behavior described in Eq. 4-9. A significant presence of the second harmonic is also observed – likely as an effect of 180° domain wall displacement in the material [4]. Deviation of the phase angle of the third harmonic from 90° and the presence of the second harmonic indicate deviation of the material behavior from an ideal Rayleigh response. However, since the phase angle of the third harmonic is closer to 90° than 0° , it can be concluded that the Rayleigh component is dominant in the description of the piezoelectric strain.

Further, according to Eq. 4-9, the value for the amplitude of the third harmonic divided by the square of the amplitude of the applied electric field should be a constant. As shown in Table 2, the value of this factor is $\sim 3 \cdot 10^{-17} \text{ m}^2/\text{V}^2$, which is consistent with the value of $3.6 \cdot 10^{-17} \text{ m}^2/\text{V}^2$ for the factor $(4\alpha_d/15\pi)$ in Eq. 11 calculated using $\alpha_d = 0.43 \cdot 10^{-15} \text{ m}^2/\text{V}^2$ (the value of α_d used here is the Rayleigh coefficient for the sample PLZT5248).

4.3 Conclusions

The converse piezoelectric response of PZT ceramics of different compositions was examined under the application of cyclic electric fields. The effects of crystal structure and addition of different dopants on d_{33} were studied. The fractional nonlinear contributions from irreversible extrinsic mechanisms for all the investigated materials were calculated from the variation of d_{33} with the driving electric field amplitude, E_0 .

For La-doped PZT ceramics, the longitudinal piezoelectric coefficient is observed to follow Rayleigh law. The largest irreversible extrinsic contribution is found to be about 55% for La-doped rhombohedral PZT ceramics. In general, the fraction of irreversible extrinsic contributions is found to be greater for the rhombohedral phase than the tetragonal phase. This

has been interpreted due to the greater possibility of non-180° domain wall displacement in the rhombohedral phase.

Extrinsic contributions are also observed to be greatly enhanced with La doping in comparison to undoped and Fe-doped ceramics. For compositions near the MPB, a maximum of 45% contribution from irreversible extrinsic mechanisms can be estimated for La-doped ceramics as compared to a maximum of 25% and 8% for undoped and Fe-doped ceramics respectively. This is consistent with the prior understanding that La-doping promotes while Fe-doping restricts domain wall motion in PZT ceramics.

The piezoelectric losses for La-doped tetragonal PZT ceramics of compositions adjacent to the MPB were described from the area of the strain-electric field hysteresis loops. Although Rayleigh-type nonlinearity is found to be the dominating mechanism for piezoelectric hysteresis, it is observed that the total hysteresis area is inadequately described from the Rayleigh relations. It is proposed that additional mechanisms, possibly in the form of the viscoelastic nature of domain wall motion in the material, contribute to the total hysteresis area. In order to calculate the complex piezoelectric coefficients, the components from Rayleigh relations and viscoelastic mechanisms were considered. An approximate description of the complex coefficients is provided from the Rayleigh relations.

Finally, in order to further investigate the applicability of the Rayleigh law, the harmonics of the converse piezoelectric strain were analyzed for La-doped tetragonal ceramics with compositions adjacent to the MPB. The Rayleigh component is found to be dominant in the prediction of the amplitude and the phase of the piezoelectric strain components.

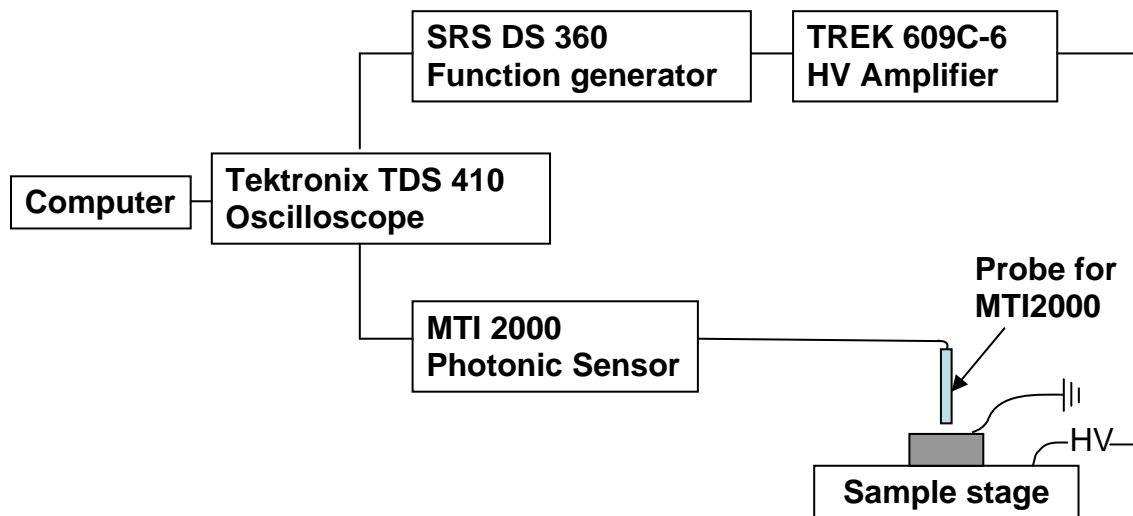


Figure 4-1. Experimental setup for measuring converse piezoelectric strain.

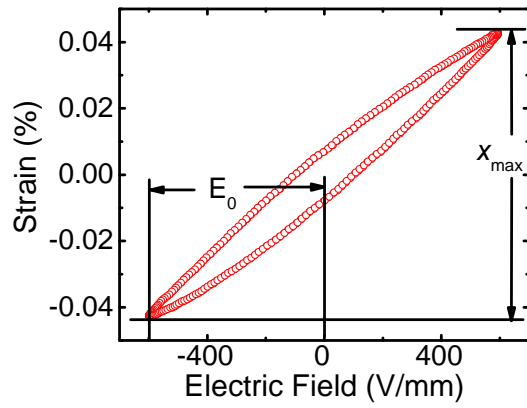


Figure 4-2. The piezoelectric coefficient d_{33} was calculated from the measured peak-to-peak longitudinal strain, indicated as x_{\max} , using Eq. 4-1.

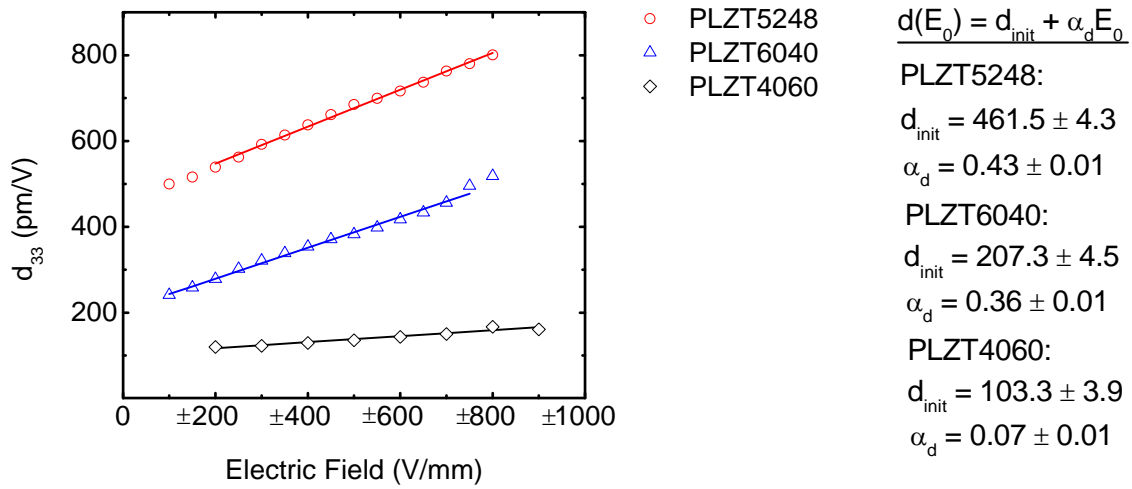
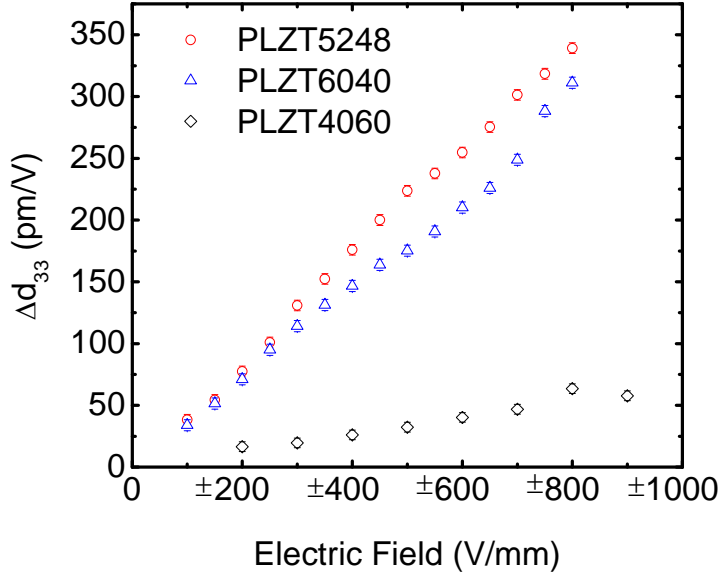
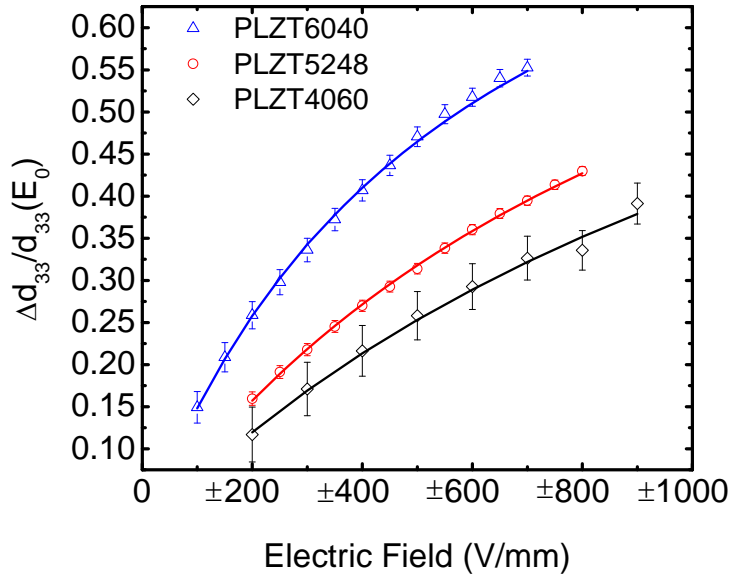


Figure 4-3. Converse piezoelectric coefficients of PLZT6040, PLZT5248 and PLZT4060 as a function of applied sinusoidal electric field amplitudes. The fits to Eq. 4-2 are shown with bold lines. The maximum Rayleigh coefficient of $\sim 0.43 \text{ (pm/V)(V/mm)}^{-1}$ is observed for the sample PLZT5248.

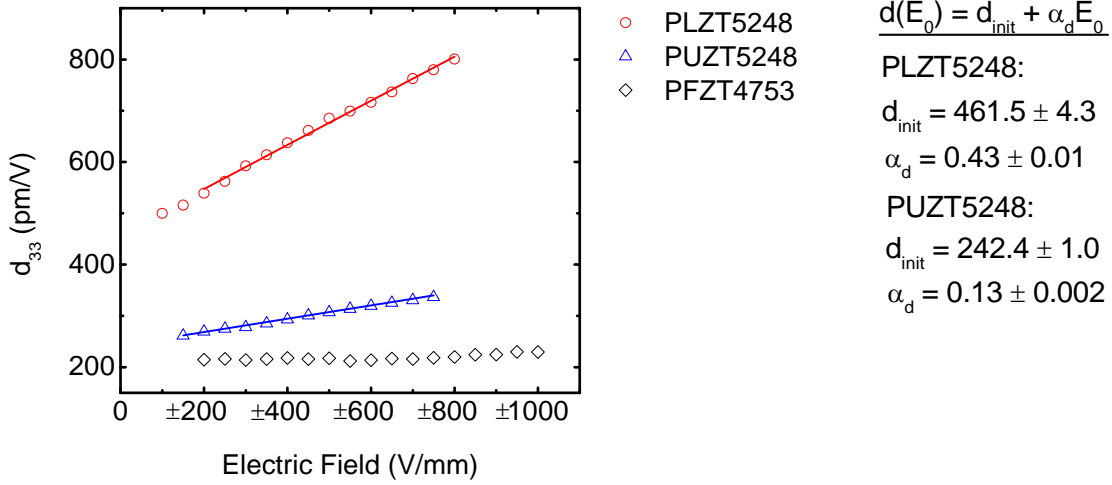


A

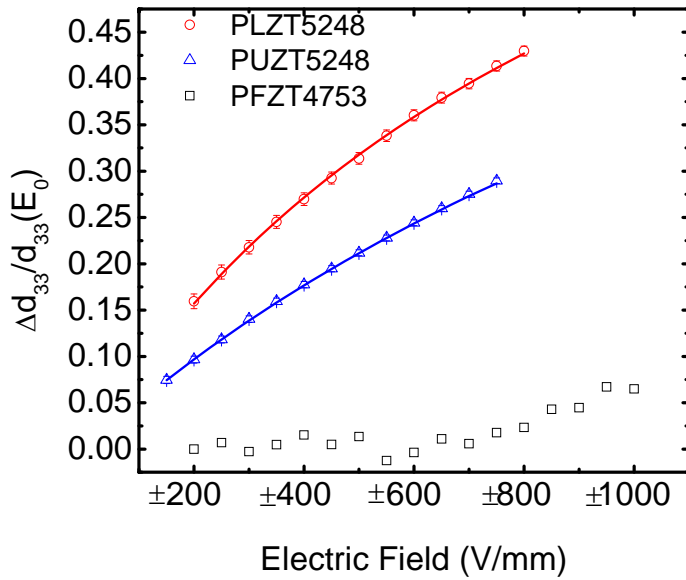


B

Figure 4-4. Estimate of the irreversible extrinsic contributions for La-doped PZT ceramics as a function of applied sinusoidal electric field amplitudes. A) Absolute irreversible extrinsic contributions Δd_{33} B) Fractional irreversible extrinsic contributions $\Delta d_{33}/d_{33}(E_0)$; the solid lines show the predictions from the Rayleigh relation described in Eq. 4-2.

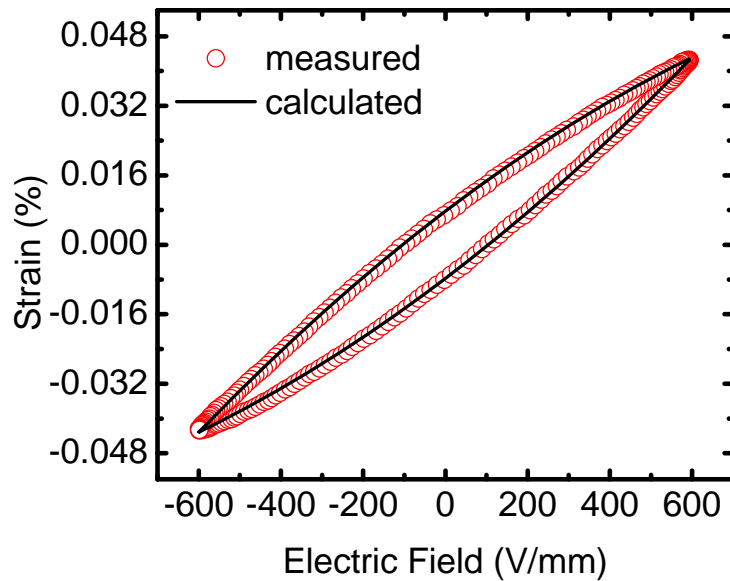
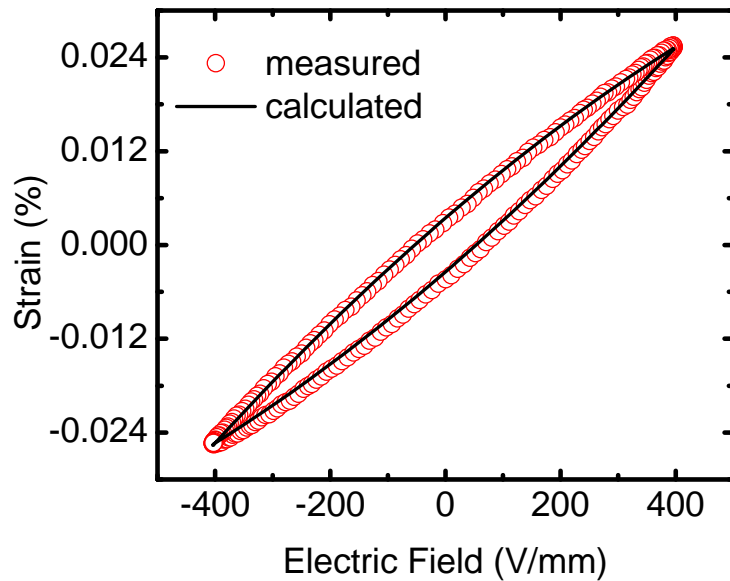


A



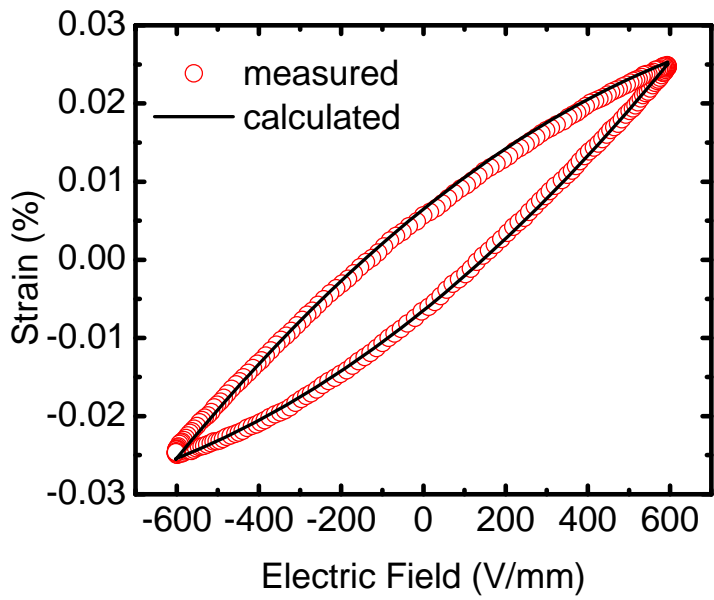
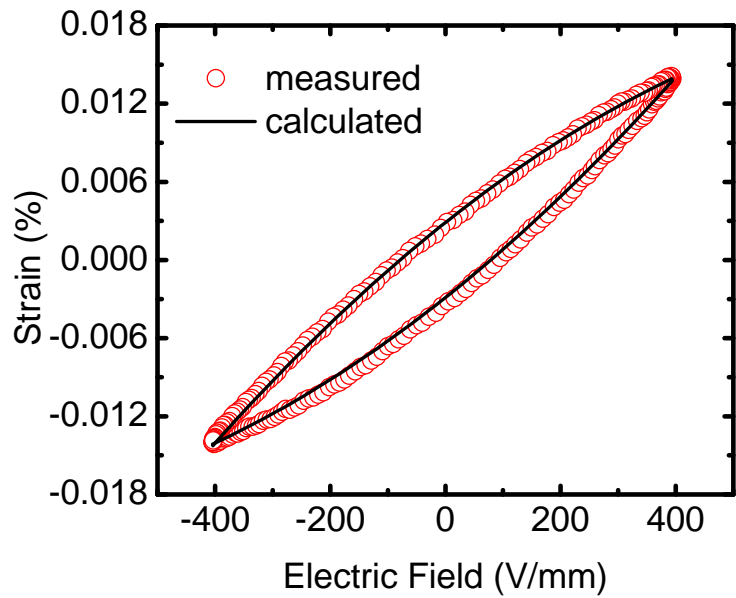
B

Figure 4-5. Converse piezoelectric coefficients and fractional extrinsic contributions for PLZT5248, PUZT5248 and PFZT4753. A) Converse piezoelectric coefficients as a function of applied sinusoidal electric field amplitudes. B) fractional extrinsic contributions $\Delta d_{33}/d_{33}(E_0)$. The solid lines show the predictions from the Rayleigh relation described in Eq. 4-2.



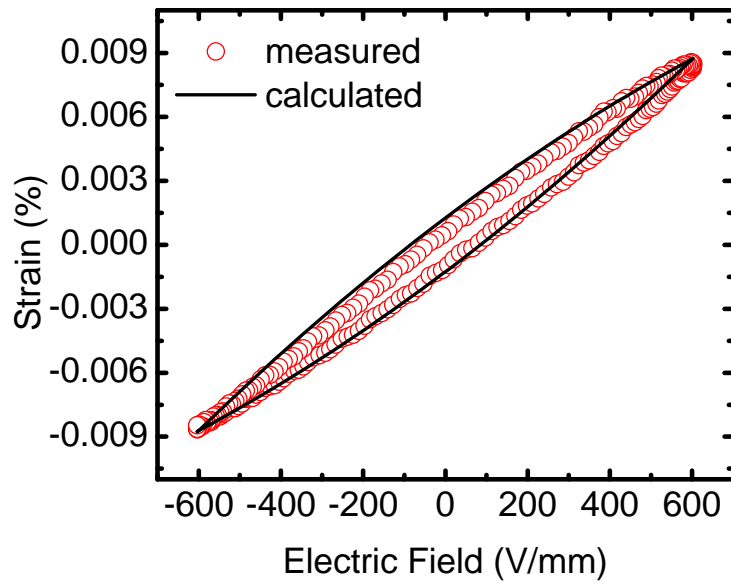
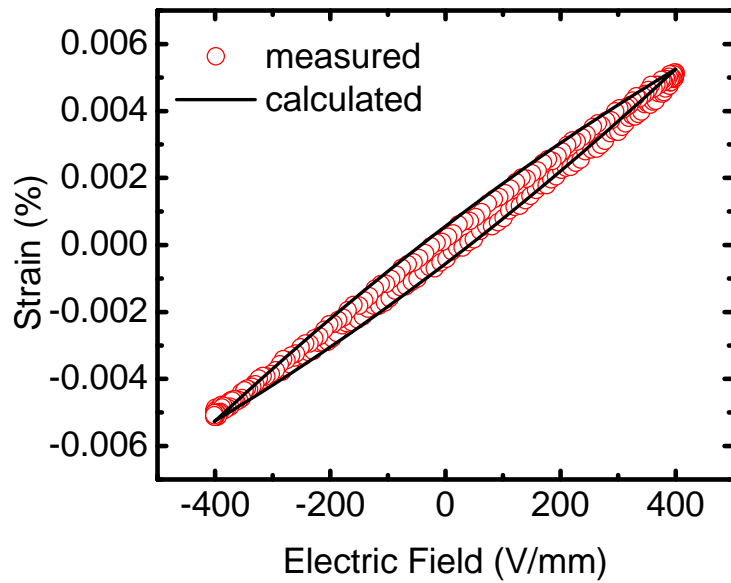
A

Figure 4-6. The strain-electric field hysteresis loops for the PZT ceramic samples at electric field amplitudes 400 V/mm and 600 V/mm: A) PLZT5248, B) PLZT6040, C) PLZT4060, D) PUZT5248. The measured loops and the loops calculated using Eq. 4-3 are in general agreement with each other.



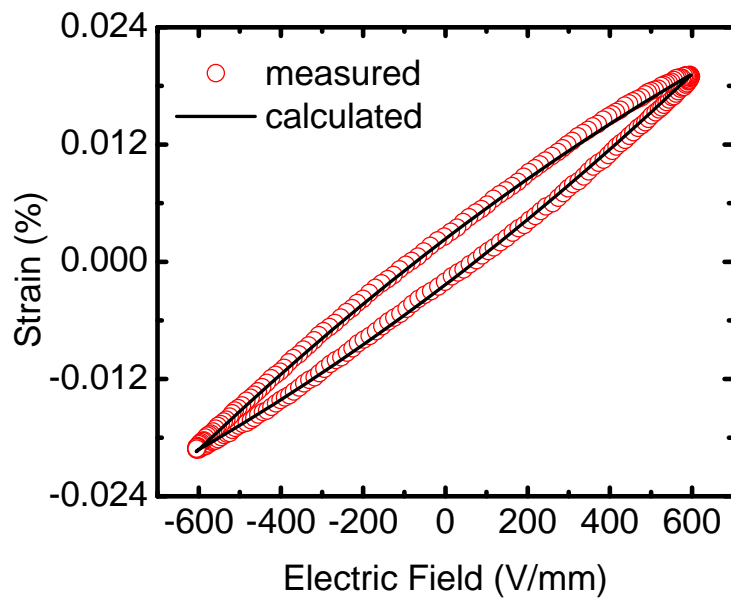
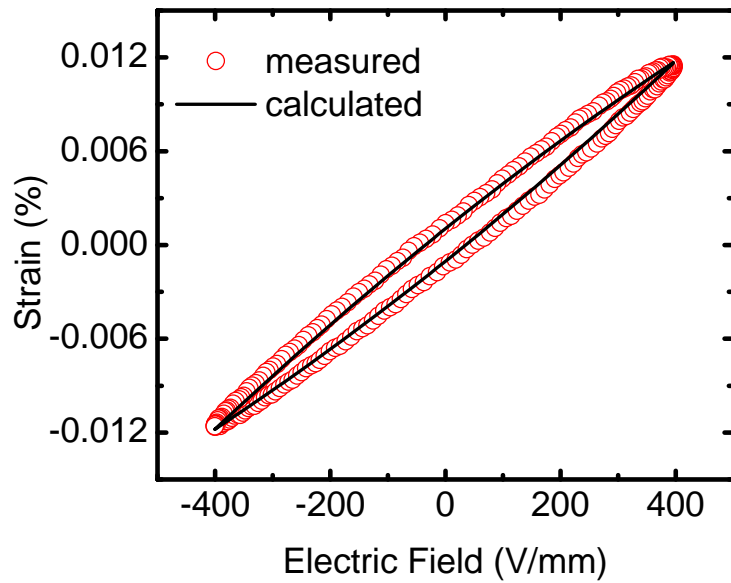
B

Figure 4-6. Continued



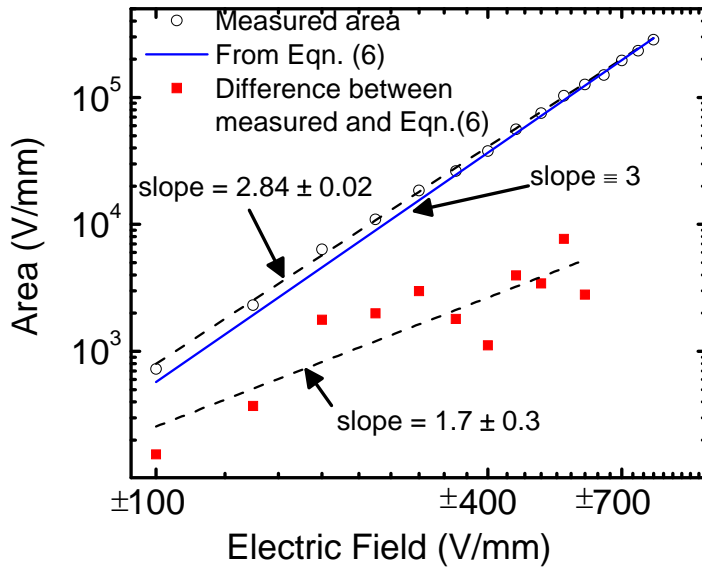
C

Figure 4-6. Continued

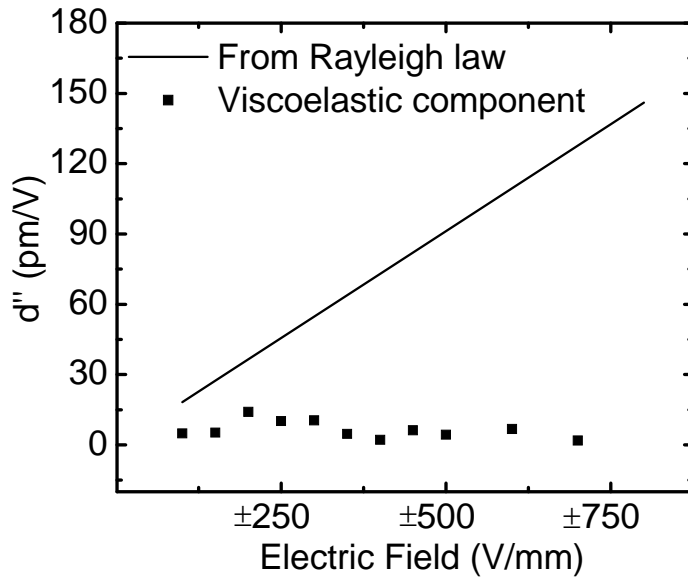


D

Figure 4-6. Continued



A



B

Figure 4-7. Hysteresis area and imaginary piezoelectric coefficient. A) Contribution to strain-field hysteresis area from different mechanisms B) imaginary piezoelectric coefficient due to Rayleigh-type nonlinearity and viscoelastic losses, for sample PLZT5248, at different amplitudes of applied sinusoidal electric fields.

Table 4-1. Harmonics of the converse piezoelectric strains for PLZT5248. Note that the phase angle of third harmonic is close to -90° for the three different amplitudes of applied electric field. Also, the value for the amplitude of the third harmonic divided by the square of the applied electric field is $\sim 3 \cdot 10^{-17} \text{ m}^2/\text{V}^2$ which is consistent with the Rayleigh coefficient of the material.

Harmonics	Electric Field Amplitudes (E_0)					
	500 V/mm		600 V/mm		700 V/mm	
	Strain amplitude (10^{-5})	Phase	Strain amplitude (10^{-5})	Phase	Strain amplitude (10^{-5})	Phase
1 st	34.04	-8°	42.9	-8.8°	53.9	-9.6°
2 nd	0.34	-105°	0.354	-128°	0.41	-160°
3 rd	0.73	-73°	1.11	-72.5°	1.4	-74.7°
3 rd harmonic/ E_0^2 ($10^{-17} \text{ m}^2/\text{V}^2$)	2.94		3.08		2.86	

CHAPTER 5 CHARACTERIZATION OF ELECTRIC-FIELD-INDUCED STRUCTURAL CHANGES USING LABORATORY X-RAY DIFFRACTION

In order to gain insight into the relative electromechanical contributions from intrinsic and extrinsic mechanisms, both in situ and ex situ diffraction experiments in PZT ceramics have been carried out in the past [30,63-71]. Recently, in situ neutron and diffraction experiments under cyclic electric fields using time-resolved stroboscopic techniques have been reported [72-74]. In the next chapter, use of high-energy X-ray diffraction for time-resolved structural characterization of piezoelectrics is described. However, over subscription of various neutron and high-energy X-ray sources can be a limiting factor towards a wider adoption of time-resolved techniques for structural characterization of piezoelectrics. Development of time-resolved diffraction capabilities at smaller-scale laboratory X-ray systems is therefore necessary. The objective of this chapter is to present the development of time-resolved diffraction techniques for a laboratory X-ray source and its utilization for in situ characterization of piezoelectrics under static and dynamic electric fields.

An in-house experimental setup is developed for collection of time-resolved X-ray diffraction patterns in synchronization with an applied periodic stimulus. Using this technique, structural changes in tetragonal La-doped PZT ceramics are measured under different electrical loading conditions. In particular, non-180° domain switching and lattice strains are measured parallel to the direction of the applied electric field of the following types: (1) static electric fields of amplitudes up to 2 kV/mm and (2) subcoercive ($< E_C$) cyclic electric fields. Correlations between the structural changes and the amplitude of the applied electric field are also studied.

5.1 Experimental Procedure

Sintered pellets of nominal composition $\text{Pb}_{0.97}\text{La}_{0.02}(\text{Zr}_{0.52}\text{Ti}_{0.48})\text{O}_3$ were polished down to thickness in the range of 0.65 - 1 mm and were subsequently annealed above the Curie

temperature to relieve surface residual stresses. Gold electrodes were sputtered on the top and bottom surfaces of the disc samples. Some of the samples were then poled using an electric field of 3.5 kV/mm at 50°C for 15 minutes. Unpoled and poled ceramics were used for all the experiments described here.

5.1.1 In situ X-ray Diffraction Under Application of Electric Field

In situ X-ray diffraction of the ceramic samples under the application of electric fields was performed using a INEL CPS120 diffractometer in reflection geometry. The diffractometer is equipped with a curved position sensitive (CPS) detector for simultaneous measurement of multiple diffraction peaks. The incident radiation used for the experiments was a monochromatic $\text{CuK}\alpha_1$ X-ray beam. The samples were positioned with respect to the incident beam such that the 002 and 111 diffraction vectors were oriented to within 5° of the applied electric field, as is illustrated in Figure 5-1A. The different techniques adopted for in situ diffraction under static and cyclic electric fields are described below.

5.1.1.1 Diffraction under static electric fields

Disc-shaped ceramic samples in their unpoled state were loaded under static electric fields of incremental amplitudes using a Stanford Research System PS350 high voltage supply. Diffraction patterns were collected in situ as a function of the amplitude of the applied electric field. The amplitude of the applied static field was stepwise and was varied within the range ± 2 kV/mm. The collection time for the diffraction patterns at each field amplitude was 720 seconds after an initial delay time of 60 seconds at each electric field amplitude.

5.1.1.2 Diffraction under cyclic electric fields

In situ diffraction of poled ceramics under cyclic electric fields were performed using the following experimental technique. A sample was driven with cyclic square-wave electric fields and simultaneous diffraction patterns were collected at pre-defined time intervals. In order to

achieve synchronization between the data acquisition and the applied electric fields the following scheme was adopted. The CPS detector of the diffractometer was connected to a computer through a data acquisition board (P7889 PCI board, FAST ComTec GmbH). The acquisition electronics of the instrument outputs a logical signal each time the acquisition of a new diffraction pattern commences. This signal was used to trigger the start of a square waveform from an Agilent 33220A function generator at specified intervals. The waveform from the function generator was used to drive a DEI PVX-4140 pulse generator which was further used to obtain a high voltage square waveform across the sample. The high-voltage input to the pulse generator was switched between two Stanford Research System (SRS PS350) high-voltage supplies in accordance with the signals received from the function generator. A cyclic square wave electric waveform was therefore obtained across the sample at intervals defined by the acquisition sequence of the diffraction patterns. The layout of the various components of the experimental setup is shown in Figure 5-1A.

An acquisition cycle was programmed so that ten diffraction patterns at equal intervals were obtained within each cycle of an applied electric field waveform of frequency ~ 0.3 Hz. The acquisition sequence of the diffraction patterns with respect to the applied electric field is illustrated in Figure 5-1B. For the specified settings, the total length of a single cycle of the applied electric field waveform is equal to the total time for ten acquisition windows as well as the delay time between each acquisition window.

In order to improve the statistics of the collected diffraction patterns, the process of data collection was repeated over multiple cycles and the diffraction patterns collected during similar time intervals with respect to the applied electric field waveform were summed. This method of data collection resulted in ten high-statistics time-resolved diffraction patterns which are

representative of the material structure at various instants within a single cycle of a continuous square wave electric field. Summation of diffraction patterns over multiple cycles of applied electric fields can be adopted if the measured structural changes are repeatable on average over multiple cycles of applied electric fields. This is a reasonable assumption for structural changes such as domain wall displacement and lattice strains under subcoercive bipolar cyclic electric fields, and has been adopted in earlier works [69,72-74].

Further details about the settings used in the software (MCDWIN) for stroboscopic data collection are provided in APPENDIX B.

5.1.2 Quantification of Structural Changes

The intensities of the different (hkl) diffraction peaks of a material are representative of the structure factor, multiplicities, and the volume fractions of the corresponding (hkl) lattice planes along their respective diffraction vectors. In tetragonal PZT, the 90° domains can be defined by the orientation of their 002 and 200 crystallographic poles. Therefore, in the absence of changing volume fractions of any coexisting phases and/or any large structural distortions, the volume fractions of the existing 90° domains along a particular specimen direction can be correlated to the intensities of the (002) and (200) diffraction peaks. In an earlier work [69], the particular correlation between the (002)-type diffraction peak intensities and the volume fraction of the 002 domains (v_{002}) along a specimen direction has been shown to be given by

$$v_{002} = \frac{\frac{I_{002}}{I'_{002}}}{\frac{I_{002}}{I'_{002}} + 2 \frac{I_{200}}{I'_{200}}}, \quad (5-1)$$

where I_{hkl} is the integrated area of the (hkl) diffraction peak for a given sample with a preferred orientation of 90° domains and I'_{hkl} is the integrated area of the same peak for a sample with no

preferred orientation of 90° domains. Eq. 5-1 takes into account the different structure factors and multiplicities of the (002) and (200) planes while calculating the domain volume fractions.

As v_{002} is equal to 1/3 for a random distribution of 90° domains, the volume fraction of the domains switched by 90° under a given condition is given by [69]

$$\eta_{002} = \frac{\frac{I_{002}}{I'_{002}}}{\frac{I_{002}}{I'_{002}} + 2 \frac{I_{200}}{I'_{200}}} - \frac{1}{3}. \quad (5-2)$$

According to Eq. 5-2, $\Delta\eta_{002}$ can have a maximum value of 2/3 (0.67) for a complete reorientation of all the 002 domains parallel to the measured direction. In order to estimate the volume fraction of the 90° switched domains parallel to an applied electric field, the value of η_{002} was calculated from the measured intensities of the (002)-type diffraction peaks with their diffraction vectors oriented parallel to the electric field. The integrated intensities of the 002 and 200 peaks were obtained from the best fit of the (002)-type diffraction peaks using two asymmetric Pearson VII functions [83]. Using asymmetric Pearson VII functions, the fit for the (002)-type diffraction peaks for an unpoled sample of the type PLZT5248 is shown in Figure 5-2.

Under the application of cyclic electric fields, the amount of 90° domain switching between the positive and negative electric field states ($\Delta\eta_{002}$) was further obtained by [72,73]

$$\Delta\eta_{002} = \eta_{002}^{positive} - \eta_{002}^{negative}. \quad (5-3)$$

The term “90° domain switching” is not intended here to necessarily imply crystallographic reorientation of entire domains. Instead, in the present context, 90° domain switching refers to a change in the crystallographic orientation of certain material volume fraction as a result of both reversible and irreversible 90° domain wall displacements.

In addition to the changing volume fractions of the non-180° domains, expansion or contraction of the lattice planes also contribute to the macroscopic electric-field-induced strain in a piezoelectric material. The component of lattice strain for the grains with their hkl poles oriented parallel to the direction of the applied electric field can be obtained from the change in the (hkl) lattice plane spacings measured parallel to the same direction. Following Bragg's law for diffraction, the change in the (hkl) lattice plane spacing is obtained from the shift in the angular position of the (hkl) diffraction peak. For tetragonal PZT ceramics, the largest lattice strains are observed away from the polarization axis of $[001]$ [66,30,74]. Therefore, in order to perform a comparative analysis of lattice strains in PZT ceramics under different electrical loading conditions, the component of lattice strain was measured for the grains with their 111 poles oriented parallel to the direction of the applied electric field. This was ensured by orienting the sample such that the 111 diffraction vector was within 5° of the direction of the applied electric field. The 111 lattice plane spacings were obtained from the best fit of the (111) diffraction peaks using a pseudo-Voigt function. A symmetric pseudo-Voigt function was adopted due to the symmetric nature of the (111) diffraction peaks. For static electric fields, the 111 lattice strain, ε_{111} , is defined as

$$\varepsilon_{111}(E_0) = \frac{d_{111}(E_0) - d_{111}(0)}{d_{111}(0)}, \quad (5-4)$$

where $d_{111}(E_0)$ is the (111) lattice spacing under an static electric field of amplitude E_0 and $d_{111}(0)$ is the (111) lattice spacing for an unpoled sample with no applied electric field. Under the application of cyclic bipolar electric fields, the 111 lattice strain is calculated from the measured (111) lattice spacings under the positive and negative parts of the applied electric field waveform and is given by

$$\varepsilon_{111}(E_0) = \frac{d_{111}(+E_0) - d_{111}(-E_0)}{d_{111}(-E_0)}, \quad (5-5)$$

where $d_{111}(+E_0)$ and $d_{111}(-E_0)$ are the 111 lattice spacings under positive and negative electric fields respectively.

It should be mentioned here that, for the diffraction geometry used in this work, a vertical displacement of the diffraction volume results in a change of the 2θ position of the diffraction peaks. APPENDIX A presents typical expected shifts in the 2θ positions caused by a vertical displacement of diffraction volume due to electric-field-induced macroscopic strain in PZT ceramics. As explained in APPENDIX A, peak shifts due to this effect are at least two orders of magnitudes less than the peak shift due to electric-field-induced lattice strains and are therefore neglected in the current calculation of 111 lattice strains.

5.2 Results and Discussions

5.2.1 Structural Changes Under Static Electric Fields

Figure 5-3A shows the variation of η_{002} during the application of static electric fields. As discussed in the preceding section, η_{002} represents the volume fraction of existing domains in the material that reorient by 90° under an applied electric field. During the initial application of positive electric fields of increasing amplitude across an unpoled sample, a sharp increase in η_{002} (from ~ 0.06 to ~ 0.17) is observed between the field amplitudes of 0.8 kV/mm and 0.9 kV/mm. This indicates that a threshold field, $E_{\text{threshold}}$, of ~ 0.9 kV/mm exists for initial 90° switching of domains in an unpoled sample. The maximum volume fraction of domains that switch by 90° (η_{002}) under an electric field of amplitude 2 kV/mm is observed to be ~ 0.35 . This is consistent with the values reported earlier for similar materials [69]. Upon subsequent decrease of the amplitude of the applied electric field to zero, η_{002} decreases from 0.35 to 0.24, which indicates

that 30% of the domains that initially switched forward switch to a perpendicular direction upon release of the electric field. Further decrease in η_{002} is observed with a reversal in the direction of the applied electric field and the minimum value of η_{002} is observed to be 0.09 at a negative field amplitude of 1 kV/mm, beyond which another sharp increase in η_{002} is evident. This indicates that with increasing negative electric fields, an increasing number of domains reorient away from the direction of the applied electric field. At negative electric fields exceeding 1 kV/mm, the material becomes polarized in the opposite direction, achieving the same ferroelastic domain state that was observed in the previous electric field direction. This is illustrated in Figure 5-4. The critical field at which η_{002} is found to be the minimum upon reversal of field direction is defined here as the coercive field E_C of the material, which is observed to be equal to 1 kV/mm. In general, Figure 5-3A closely resembles the butterfly shape of the macroscopic strain-electric field loop of sample PLZT5248 shown in Figure 3-3B. However, a few discrepancies between the two can be noted. Under a sinusoidal electric field of frequency 100 mHz, the threshold field, $E_{\text{threshold}}$, is observed to be about 1.2 kV/mm which is higher than the value of ~ 0.9 kV/mm observed from in situ X-ray diffraction experiments under static electric fields. Similarly, the macroscopic coercive field of 1.35 kV/mm is higher than the coercive field of 1 kV/mm observed with X-ray diffraction. The coercive field E_C is not an absolute threshold field but depends on the rate or frequency of the applied electric field under which it is determined [4]. Therefore the currently observed difference in E_C , determined from macroscopic and X-ray diffraction measurements, may be contributed by the fact that the X-ray measurements are taken under static electric fields unlike a continuous cyclic field as adopted for macroscopic measurements. This point further emphasizes the importance of characterizing the structural response of these materials under cyclic electric fields.

The component of lattice strain for the grains with their 111 poles oriented parallel to the direction of the applied electric field is calculated from the (111) lattice plane spacings using Eq. 5-4. Figure 5-3B shows the 111 lattice strains, ε_{111} , as a function of the applied electric field amplitude. The effect of the electric field amplitude on ε_{111} correlates with the field-dependent 90° domain switching shown in Figure 5-3A. Such behavior for 111 lattice strains in PZT ceramics have been reported previously [66]. The 111 lattice strains in poled PZT ceramics were previously described in terms of misfit strains between the differently oriented grains in the material which undergoes different amounts of 90° domain switching under the application of electric fields [30]. In particular, since the grains with their 111 poles oriented parallel to the applied electric field do not have an energetic preference for domain switching, they experience tensile or compressive stresses due to the extension or compression of the neighboring grains that are more favorably oriented for 90° domain switching. It is therefore possible that the 111 lattice strains under the application of static electric fields are influenced by 90° domain switching in the neighboring grains.

5.2.2 Structural Changes Under Cyclic Electric Fields

Figure 5-5A shows the (002) and (200) diffraction peaks as a function of time during the application of a cyclic square wave electric field of amplitude ± 650 V/mm and frequency 0.3 Hz. It is observed that the intensity of the (002) peak increases during the positive part of the applied electric field waveform along with a simultaneous decrease in the intensity of the (200) peak. During the negative part of the electric field waveform the situation is reversed whereby the (200) peak increases in intensity at the expense of the (002) peak. The observed intensity interchanges between the (002) and (200) diffraction peaks clearly indicate changes in the volume fraction of the 90° domains in the material under the application of subcoercive cyclic electric fields. It should be stated here that no measurable amount of strain can be observed for

the (002) and (200) lattice planes, within the error of the peak fitting procedure. Instead, a significant strain for (111) planes under the same electrical loading conditions is observed, as is indicated by arrows in the contour plot of Figure 5-5B. It is evident from Figure 5-5B, that the (111) peak position shifts to a lower 2θ angular position during the positive part of the applied electric field waveform, indicating an increase in the (111) lattice plane spacings.

In both Figures 5-5A and 5-5B, discrete changes in the diffraction patterns can be observed when the polarity of the electric field is reversed within the applied waveform. The timing resolution of the collected diffraction patterns was inadequate to quantify the time-dependence of the measured structural changes. Therefore, in order to quantify the measured structural changes, two representative diffraction patterns corresponding to the positive and the negative states of the applied square waveform were obtained by a summation of the diffraction patterns during the corresponding portions of the applied waveform.

Figure 5-6A shows the (002)-type diffraction peaks during the positive and negative states of the applied square wave electric field of amplitude ± 650 V/mm. The volume fractions of the 90° domains in the material were determined from the integrated areas of the (002) and the (200) diffraction peaks. Using Eqs. 5-2 and 5-3, the change in the volume fraction of the 90° domains, $\Delta\eta_{002}$, is found to be ~ 0.05 or 5% parallel to the applied electric field. This value is consistent with previous measurements of domain switching under cyclic electric fields in commercial PZT ceramics [72,73].

The 111 lattice strain measured under the same electrical loading conditions is highlighted in Figure 5-6B. The 111 lattice strain parallel to the applied electric field is calculated to be $\sim 0.07\%$ using Eq. 5-5. This value corresponds to a lattice strain coefficient of 530 pm/V, a value

of comparable magnitude to the direct piezoelectric coefficient of 480 pC/N measured for this material using a Berlincourt d_{33} meter.

In order to investigate the relationship between the amplitude of the applied square wave electric field and the different structural changes, the amount of 90° domain switching ($\Delta\eta_{002}$) and the 111 lattice strains (ε_{111}) were measured as a function of field amplitude. The measured values for $\Delta\eta_{002}$ and ε_{111} are plotted in Figures 5-7A and 5-7B, respectively. It is observed that $\Delta\eta_{002}$ monotonically increases with increasing electric field amplitude. This is in agreement with the generally accepted understanding of nonlinear electromechanical contributions from non- 180° domain wall motion in polycrystalline piezoelectric ceramics under subcoercive electric fields [3-5]. It is generally understood that the contributions of non- 180° domain wall motion to the macroscopic properties can increase with the amplitude of the applied external field.

In order to understand the field-dependence of ε_{111} , the coefficient of the electric-field-induced 111 lattice strain, β_{111} , is calculated from ε_{111} and the electric field amplitude E_0 using

$$\beta_{111} = \frac{\varepsilon_{111}(E_0)}{2E_0}. \quad (5-6)$$

It should be noted here that a value of two is in the denominator because the electric field is bipolar and the value of E_0 represents only half of the total electric field amplitude. The values of $\beta_{111}(E_0)$ calculated from Eq. 5-6 are shown in Figure 5-6B. It is observed that β_{111} increases with an increase in E_0 . A linear equation of the type

$$\beta_{111}(E_0) = \beta_{111}^{init} + \alpha E_0 \quad (5-7)$$

is used to fit the linear dependence of the strain coefficient with respect to the electric field amplitude. In Eq. 5-7, $\beta_{111}(E_0)$ is the 111 lattice strain coefficient for an electric field amplitude of $\pm E_0$, α is the coefficient for the linear dependence, and the value of β_{111}^{init} represents the value

of β_{111} as $E_0 \rightarrow 0$. The values of β_{111}^{init} and α are 117 pm/V and $0.7 \text{ (pm/V)} \cdot (\text{V/mm})^{-1}$ respectively. Eq. 5-7 implies a 111 lattice strain dependence of $\varepsilon_{111}(E_0) = 2(d + \alpha E_0)E_0$.

The observed changes in the 111 lattice strain and 111 lattice strain coefficients under static and cyclic electric fields may indicate that, in addition to their dependence on thermodynamic variables [17-27], the lattice strain coefficients in a polycrystalline matrix may be influenced by other extrinsic factors such as misfit elastic strains arising from non-180° domain switching [30].

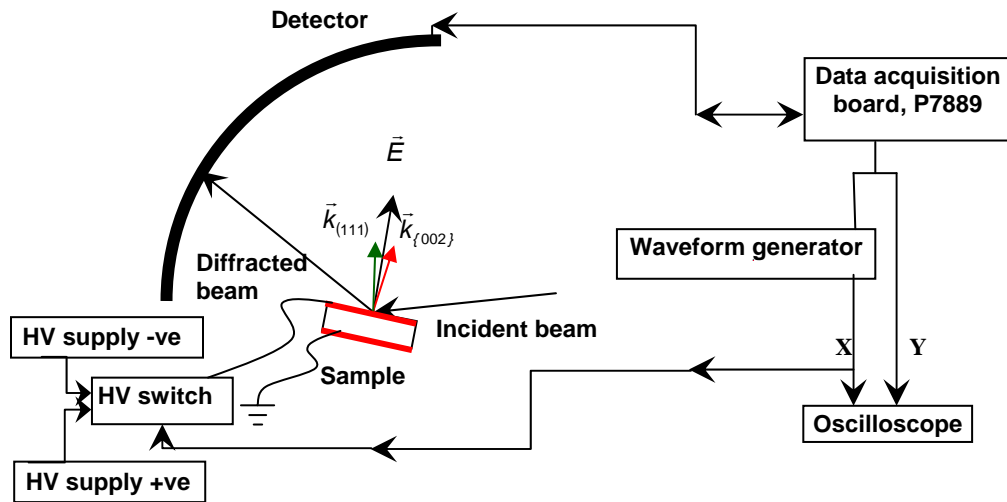
5.3 Conclusions

A laboratory X-ray diffractometer was used to measure the structural changes in tetragonal La-doped PZT ceramics under the application of static and dynamic electric fields in situ. The amount of 90° domain switching parallel to the applied field was calculated from the intensity interchange between the 002 and 200 diffraction peaks. In addition, in order to calculate the electric field induced lattice strains under certain applied electric fields, the change in the 111 lattice spacings were measured.

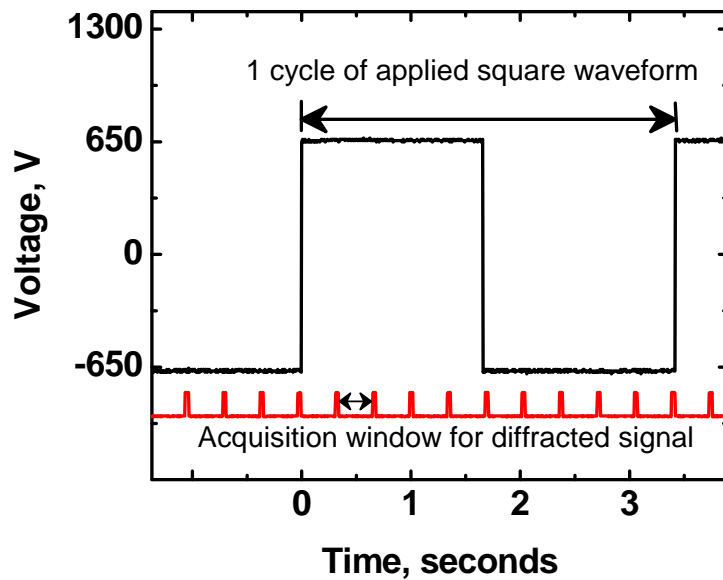
Under application of static electric fields, η_{002} is found to have a maximum value of 0.35 for an electric field of amplitude 2 kV/mm. In general, under static electric fields, the 90° domain switching and the 111 lattice strains are observed to correlate with the macroscopic strain-electric field hysteresis loop. However, differences in $E_{\text{threshold}}$ and E_C calculated from macroscopic strain measurements and X-ray diffraction analysis are noted, which are attributed to the frequency dependence of the coercive field E_C .

A time-resolved X-ray diffraction technique was adopted to measure the structural changes under applied cyclic electric fields in situ. For a square wave electric field of amplitude ± 650 V/mm and frequency 0.3 Hz, $\Delta\eta_{002}$ is observed to be 0.05, along with $\sim 0.07\%$ strain for the 111

lattice planes. Both the amount of 90° domain switching and the 111 lattice strains are observed to increase with an increase in the amplitude of the cyclic electric field. The field dependence of the 111 lattice strains are described in terms of misfit strains between the differently oriented grains under the application of electric fields.



A



B

Figure 5-1. Experimental setup and synchronization settings for *in situ* diffraction experiments. A) Schematic layout of the experimental setup for *in situ* diffraction under applied electric field. The sample is oriented such that the 002 and the 111 diffraction vectors are oriented to within 5° of the applied electric field. B) The sequential acquisition windows (shown at the bottom) for the collected diffraction patterns with respect to the applied electric field (shown on the top).

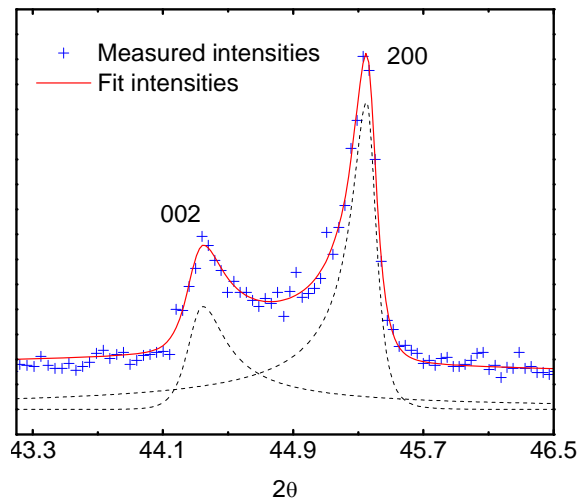
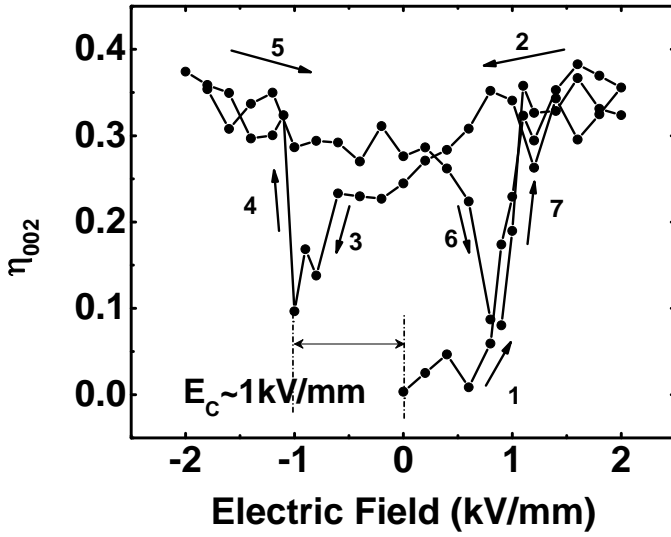
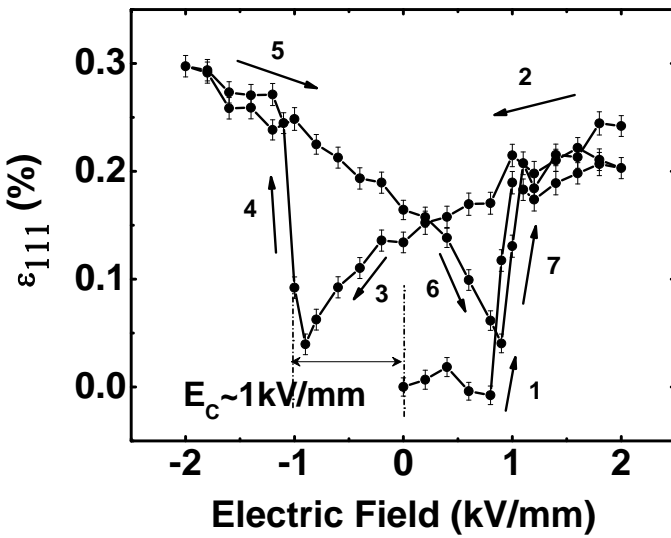


Figure 5-2. The fit for the (002)-type diffraction peaks for an unpoled sample of the type PLZT5248. Two asymmetric Pearson VII functions were used for peak fitting in order to account for 002 and 200 diffraction peaks (shown by dotted lines in black).



A



B

Figure 5-3. Structural changes measured under the application of stepwise static electric fields: A) η_{002} and B) ε_{111} , as a function of the field amplitude. The path followed for incrementing electric field amplitude is indicated by the arrows sequenced 1 to 7. The coercive field E_C for domain switching is observed to be ~ 1 kV/mm from the plot of η_{002} vs the electric field amplitude.

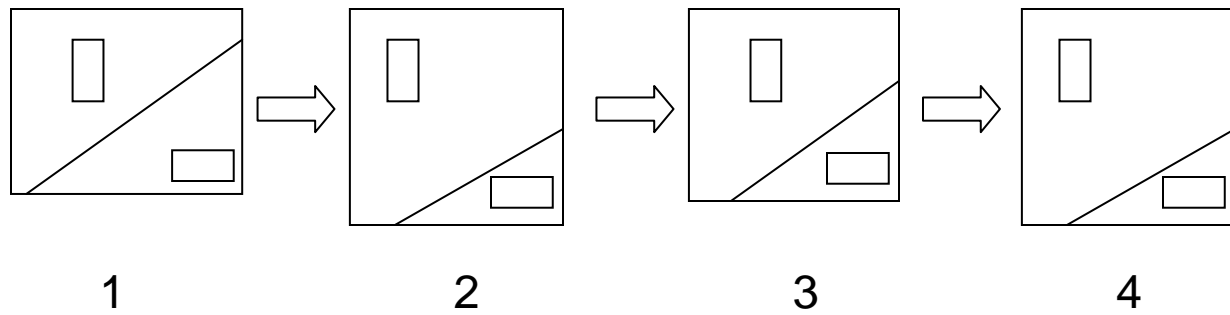
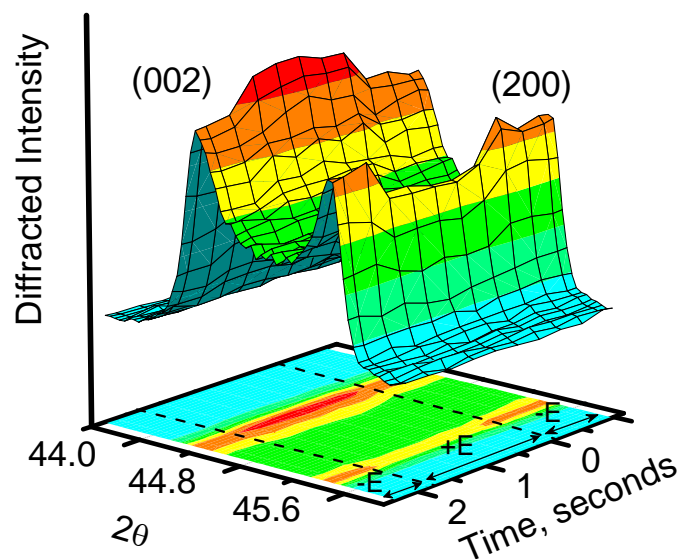
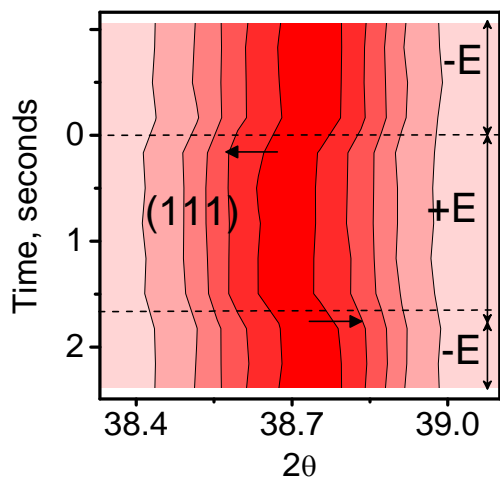


Figure 5-4. Schematic of the proposed 90° domain switching process under static electric fields E_0 . The 90° domain states are indicated by the orientation of the rectangles. The numbers refer to the specific region of the η_{002} -electric field plot shown in Figure 5-3A: (1) $0 < E_0 < +E_C$, (2) $E_C < E_0 < +E_{\max}$, (3) $-E_C < E_0 < 0$, (4) $-E_{\max} < E_0 < -E_C$; E_{\max} refers to the maximum amplitude of applied electric field.

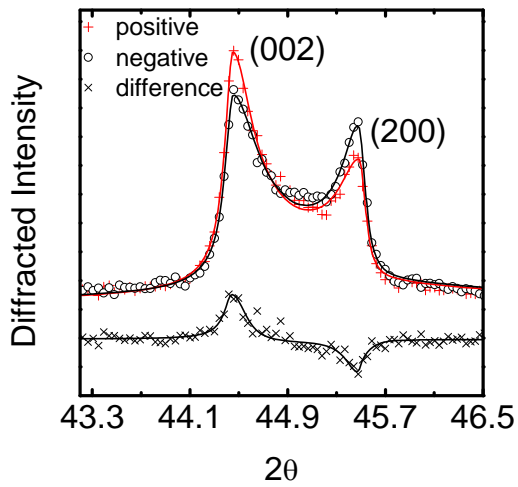


A

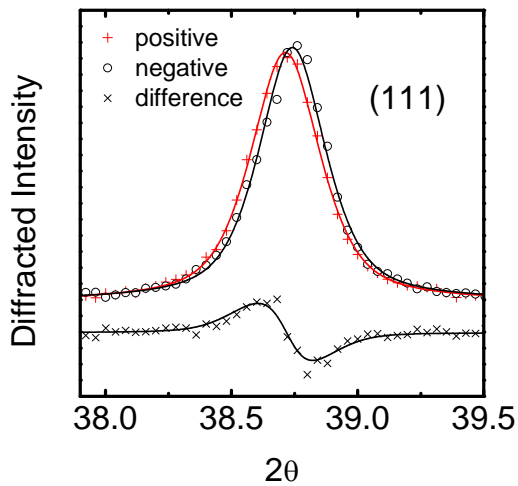


B

Figure 5-5. Structural changes as a function of time during the application of cyclic square wave electric field of amplitude ± 650 V/mm and of frequency 0.3 Hz. A) Intensity interchange between the (002) and (200) peaks can be observed indicating change in volume fraction of 90° domains. B) Contour plot of the (111) diffraction peak shows a shift towards lower 2θ under positive state of the applied electric field waveform.

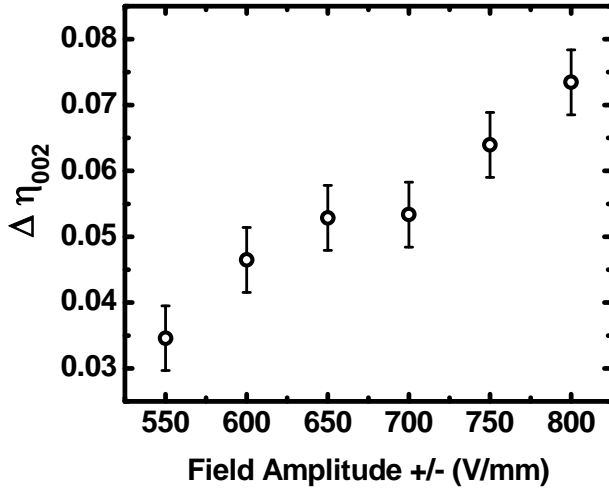


A

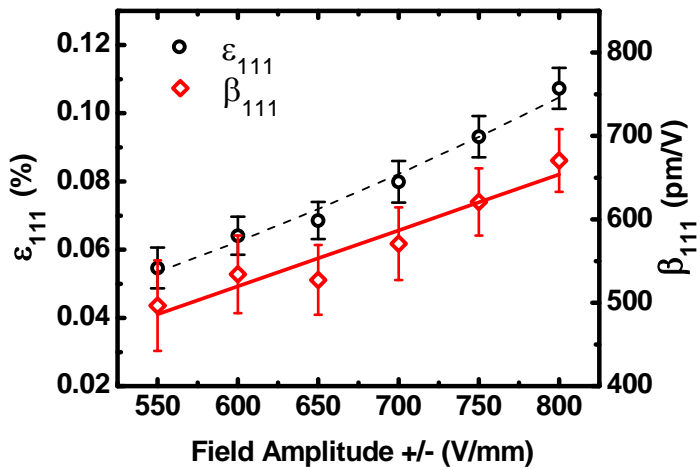


B

Figure 5-6. Measured and fit patterns of the A) (002)-type, and B) (111) diffraction peaks, during the positive and the negative parts of the applied electric field waveform. The difference between the positive and the negative states are plotted at the bottom of the each plot. The difference plot in A demonstrates an intensity interchange between the (002) and the (200) peaks, whereas the difference plot in B demonstrates a shift of (111) peak with no apparent change in peak profile.



A



B

Figure 5-7. Dependence of non-180° domain switching and 111 lattice strains on amplitude of applied cyclic electric fields. A) $\Delta \eta_{002}$ as a function of the amplitude of the applied square wave electric field. A monotonic increase in the amount of non-180° domain switching can be observed with increasing field amplitude. B) 111 lattice strain and lattice strain coefficient as a function of the applied square wave electric field amplitude. The dashed line in black and the bold line in red shows the corresponding fits for ϵ_{111} and β_{111} , respectively.

CHAPTER 6 CHARACTERIZATION OF ELECTRIC-FIELD-INDUCED STRUCTURAL CHANGES USING HIGH-ENERGY SYNCHROTRON X-RAY DIFFRACTION

In situ diffraction experiments using a laboratory X-ray source provide an understanding of the nature of different structural changes contributing to the overall electric-field-induced strain in piezoelectric ceramics, as presented in Chapter 5. However, the penetration depth of Cu-K α radiation in PZT ceramics is of the order of micrometers. In contrast, high-energy X-rays (~80 keV) have much larger penetration depths of the order of millimeters in PZT ceramics (See APPENDIX B). Therefore, diffraction in transmission mode using high-energy X-rays is necessary for measuring electric-field-induced structural changes from the bulk of these materials.

Measurement of structural changes such as non-180° domain switching and lattice strains in Pb(Zr,Ti)O₃ ceramics, using time-resolved high-energy X-ray diffraction, are presented in this chapter. The contributions to the electric-field-induced strains from non-180° domain switching and lattice distortions are calculated as a function of material composition and dopants. Correlations between the structural changes and the amplitude of the applied electric fields are also studied.

6.1 Experimental Procedure

6.1.1 Sample Synthesis and Preparation

The sintered and poled ceramics were cut in dimensions of 1 mm \times 1 mm \times 3 mm for *in situ* electric field induced structural studies. In order to verify any possible change in the poled state of the materials subsequent to cutting, piezoelectric measurements were taken before and after the cutting process. No changes were observed in the piezoelectric coefficient d_{33} of the ceramic samples subsequent to their dimensioning. Electric fields were to be applied across the 1

mm × 3 mm faces. The surfaces across which electric fields were to be applied during *in situ* studies were coated with an air-dry commercial silver paint (RS components 186-3600).

6.1.2 Time-Resolved Diffraction

High-energy X-ray diffraction experiments were carried out at beamline ID15B of the European Synchrotron Radiation Facility (ESRF), located at Grenoble, France. A beam energy of 87.80 keV was generated from a bent Laue (511) silicon monochromator. A schematic of the experimental setup and sample diffraction image are shown in Figure 6-1. The incident beam size was set to $300 \times 300 \mu\text{m}^2$ using a set of Tungsten slits just prior to the sample stage. An *in situ* electric field cell was used, whereby an electric field of up to 3 kV/mm can be applied to a sample in air [84]. Diffracted intensities were collected using a Pixium 4700 flat panel detector [85] at a distance of approximately 1130 mm. The center of the Debye rings was approximately coincident with the center of the detector panel, as shown in Figure 6-1A.

Time resolved diffraction images were collected during cyclic actuation of the sample. The stroboscopic data acquisition process was achieved by the following process. An electric field signal was applied across the sample using a function generator (FLUKE PM5193) and a high-voltage amplifier (TREK 10/10B). A delay generator was simultaneously triggered by this signal and applied a set delay (Δt in Figure 6-1B). This delayed signal was then used to trigger a detector frame, the length of which decided the time resolution of the experiments (Frame Length in Figure 6-1B). A number of detector frames were then summed together into a single image, and the delay signal (Δt), adjusted. In this way, large area detector images are collected as a function of time, and can be represented in a single electric field cycle [84].

6.2 Analysis of Diffraction Data

6.2.1 Binning of Diffraction Data at Different Azimuthal Angles

The 2-D images from the area detector were first analyzed using software *Fit2D Ver. 11.012* [86]. The beam center and tilt were refined for each pattern with respect to a standard diffraction pattern of CeO_2 (part of standard reference material 674b from National Institute of Standards and Technology), collected under identical settings. The Debye-Scherrer diffraction rings from the sample were segmented into azimuthal sectors of 10° width (as indicated in Figure 6-1). The pattern within each azimuthal sector Φ was integrated to obtain equivalent diffracted intensities as a function of 2θ [87]. The pattern of the hkl diffracted intensity within each azimuthal sector Φ is indicative of the structural state of grains with their hkl poles approximately parallel to an angle Φ to the applied electric field (within $\pm 5^\circ$). This effect is highlighted in Figure 6-1C where the induced domain texture is clearly visible at selected azimuthal bins.

6.2.2 Fitting of (hkl) Diffraction Peaks

In order to measure the structural changes in piezoelectric ceramics during the application of cyclic electric fields, calculations of the intensities and the 2θ positions of the different (hkl) diffraction peaks are necessary. Two different approaches can be taken to obtain the relevant information from the measured diffraction patterns. In one approach, a least-square fitting of the entire diffraction pattern over a large 2θ range can be performed such as Rietveld refinement [88]. However, it is known that stresses along non- 180° domain walls [89-91] as well as intergranular strains [30] in polycrystalline ferroelectrics can lead to different asymmetric distortions of specific (hkl) diffraction peaks. The asymmetric nature of the different (hkl) diffraction peaks can be difficult to take into account for the Rietveld refinement approach. Fitting of individual (hkl) diffraction peaks can instead be applied to model the diffraction

patterns in these materials [83]. In this approach, each individual (*hkl*) diffraction peak can be fit separately using a suitable profile shape function in order to obtain information about the 2θ position and intensity of the corresponding peak. In the current work, the structural information of the state of the non-180° domains and lattice strains are obtained from the best fits of the individual (*hkl*) diffraction peaks.

The different (*hkl*) diffraction peaks were fit using split Pearson VII peak profile functions [83,92]. Peak fitting routines for the different (*hkl*) peaks were executed within the commercial software package *Igor Pro 5.05A*.

6.2.3 Analysis of Ferroelectric Phases

Diffraction patterns of all the ceramic samples were found to be consistent with a pseudocubic perovskite structure; no impurities or secondary phases were identified from the measured diffraction patterns. An analysis of the crystallographic phases present in the synthesized ceramics is necessary prior to their structural characterization under applied electric fields. This was performed by analyzing the various diffraction peaks of the unpoled and poled ceramic samples.

The (002)-type and the (111)-type diffraction peaks of the different ceramic samples in their unpoled state are shown in Figures 6-2A and 6-2B, respectively. Ceramics with Zr/Ti ratio less than or equal to 52/48 show a single (111) and two (002)-type diffraction peaks, while the ceramics with Zr/Ti ratio equal to 60/40 show a single (002) and two (111)-type diffraction peaks. These observations are consistent with the presence of a tetragonal phase for compositions with Zr/Ti ratio $\leq 52/48$ and a rhombohedral phase for compositions with Zr/Ti ratio equal to 60/40. The coexistence of tetragonal and rhombohedral phases is not evident from the collected diffraction patterns in any of the ceramic samples. These results agree with the phase diagram of

Pb(Zr,Ti)O₃ solid solution (Figure 3-1) and the diffraction patterns reported elsewhere for materials with similar compositions [93].

Recently, a monoclinic phase has been proposed for PZT ceramics with compositions close to the morphotropic phase boundary (MPB) and Zr/Ti ratio equal to 53/47 [94]. In order to verify the presence or absence of any monoclinic phase, the (022)-type diffraction peaks of the different ceramic samples were analyzed. A monoclinic phase would be evident with the splitting of the (022)-type diffracted intensities into three different peaks. Figure 6-2C shows the (022)-type diffraction peaks of the samples PLZT5248, PUZT5248 and PFZT4753, none of which show this characteristic. The presence of a monoclinic phase in samples with compositions close to the MPB is therefore not considered here.

The diffraction of the poled samples under cyclic electric fields showed similar characteristics with regard to their phase analysis. Therefore, the coexistence of different crystallographic phases or the presence of a monoclinic phase was not considered in further analysis of electric field induced structural changes for the ceramics used in this study.

6.2.4 Binning of Diffraction Data with Respect to Time

The time dependence of the structural changes in the material within each cycle of an applied electric field was characterized from the time-resolved diffraction patterns. During the *in situ* X-ray diffraction experiments, the applied electric fields across the ceramic samples were monitored using a Tektronix TDS3012 oscilloscope. The waveforms for the bipolar electric fields were observed to have a square profile with complete positive-to-negative transition within one microsecond.

Figure 6-3A shows time-resolved (002)-type diffraction peaks of the sample PLZT5248 during the application of a cyclic square wave electric field of amplitude ± 750 V/mm and frequency 1 Hz, for $\Phi = 0^\circ$, an angle approximately parallel to the applied electric field. It is

observed that the (002) diffraction peak intensity increases during the positive segment of the applied electric field waveform along with a simultaneous decrease in the intensity of the (200) diffraction peak. The situation is reversed during the negative segment of the applied electric field waveform, i.e., the (200) peak intensity increases at the expense of the intensity of the (002) peak. The time dependence of the intensity interchange between the (002) and the (200) peaks was obtained from a simple ratio of their integrated peak intensities I_{002}/I_{200} . Figure 6-3B shows the values for I_{002}/I_{200} as a function of time and as a function of angle to the direction of the applied electric field. A transition period of < 0.05 s is observed for the measured intensity interchanges between the (002)-type peaks, as illustrated by the shaded portion in Figure 6-3B. I_{002}/I_{200} is observed to be generally stable beyond this time period, as is illustrated in the unshaded portions in Figure 6-3B. The time dependence of the (111) lattice spacings d_{111} parallel to the electric field is shown in Figure 6-3C. d_{111} shows a time dependence similar to one observed for I_{002}/I_{200} . In general, a transition period of < 0.05 s is also observed for the 2θ positions of all other (hkl) peaks analyzed for this material. The time dependence of the diffraction patterns described here for the sample PLZT5248 is also observed for other materials investigated in the work, under cyclic square-wave electric fields of frequency 1 Hz.

From the above discussion, it is evident that the structural changes in the investigated materials is quite rapid and shows a transition period of less than 0.05 s under the conditions of the applied electric fields. For statistical advantages in subsequent analyses, two representative diffraction patterns corresponding to the positive and the negative states of an applied square wave electric field were obtained by summing diffraction data within each portion of the electric field. For each state of applied electric field, the representative diffraction pattern was obtained

by a summation of the diffraction patterns during the last 0.045 s of the corresponding section of the electric field waveform, after the region of transition.

6.2.5 Quantification of Structural Changes

6.2.5.1 Non-180° domain switching

In earlier works, the volume fraction of non-180° domains has been shown to be a function of the intensities of characteristic diffraction peaks [30,63-69]. The relation between the intensities of the (002)-type diffraction peaks and the volume fraction of the 90° domains in tetragonal ceramics were introduced in Chapter 5. The relation between the intensities of certain characteristic diffraction peaks and volume fraction of non-180° domains in tetragonal and rhombohedral perovskites are reintroduced here for the benefit of the reader.

In perovskite ferroelectric materials with a tetragonal crystal structure, the volume fraction of the 002 domains along a particular specimen direction is given by

$$v_{002} = \frac{\frac{I_{002}}{I'_{002}}}{\frac{I_{002}}{I'_{002}} + 2 \frac{I_{200}}{I'_{200}}}, \quad (6-1)$$

where I_{hkl} is the integrated area of the (hkl) diffraction peak for a given sample with a preferred orientation of 90° domains and I'_{hkl} is the integrated area of the same peak for a sample with no preferred orientation of 90° domains. The volume fraction of the 111 domains along a particular specimen direction for a rhombohedral perovskite ferroelectric is obtained by the following modification of Eq. 6-1,

$$v_{111} = \frac{\frac{I_{111}}{I'_{111}}}{\frac{I_{111}}{I'_{111}} + 3 \frac{I_{\bar{1}\bar{1}\bar{1}}}{I'_{\bar{1}\bar{1}\bar{1}}}}, \quad (6-2)$$

where lattice spacings for (111) planes are larger than that of $(11\bar{1})$ planes. In Eqs. 6-1 and 6-2, the numerical factors in the denominator account for the multiplicities of the particular (hkl) lattice planes.

For a random distribution of non-180° domains, v_{002} is equal to 1/3 and v_{111} is equal to 1/4, corresponding to equal distribution of possible ferroelastic domain variants. Therefore, the volume fraction of the domains reoriented by non-180° along a specimen direction, under a certain condition, is given by

$$\eta_{002} = v_{002} - \frac{1}{3}, \quad (6-3)$$

for a tetragonal perovskite, and

$$\eta_{111} = v_{111} - \frac{1}{4}, \quad (6-4)$$

for a rhombohedral perovskite.

Under the application of cyclic electric fields of subcoercive amplitudes, switching of non-180° domains results in dynamic changes in η_{002} and η_{111} . The term “non-180° domain switching” is not intended here to necessarily imply crystallographic reorientation of entire domains. Instead, in the present context, non-180° domain switching refers to a change in the crystallographic orientation of certain material volume fraction as a result of both reversible and irreversible non-180° domain wall displacements. The change in the volume fractions of the non-180° domains under bipolar square-wave electric fields can be given by,

$$\Delta\eta = \eta^+ - \eta^-, \quad (6-5)$$

where η^+ and η^- are values of η for maximum positive and minimum negative electric fields, respectively, within a cyclic square-wave electric field.

The use of a 2-D detector allows calculation of η and $\Delta\eta$ at different angles with respect to the direction of the applied electric field. This introduces an extra dimension for characterizing electric-field-induced non-180° domain switching in the material, in addition to the amplitude of the applied electric field. For example, Figure 6-4 shows η_{002} as a function of field amplitude as well as orientation with respect to the direction of applied field, for an unpoled La-doped tetragonal PZT ceramic under the application of static electric fields. The measurements for non-180° domain switching provided in this chapter are therefore complementary to the measurements provided in Chapter 5. The advantage of this added dimension of orientation towards complete characterization of material behavior will be apparent in the later sections of this chapter.

In all the ceramic samples, $\Delta\eta$ were calculated for orientations corresponding to $0 < \Phi < 90^\circ$. The sample symmetry for a poled polycrystalline ceramic is given by ∞mm , with the ∞ -fold rotation axis parallel to the poling direction. In all the experiments, the direction of the applied electric field was kept parallel to the poling direction. It is therefore expected that during cyclic electrical loading of the poled ceramics, the structural state for the following quadrants are symmetric with respect to the quadrant $0 < \Phi < 90^\circ$: $90^\circ < \Phi < 180^\circ$, $180^\circ < \Phi < 270^\circ$, and $270^\circ < \Phi < 360^\circ$. Therefore, $\Delta\eta$ were calculated only for orientations corresponding to $0 < \Phi < 90^\circ$.

6.2.5.2 Electric-field-induced lattice strains

Following Bragg's law for diffraction, the change in the (hkl) plane spacing can be determined from the change in the 2θ position of the (hkl) diffraction peak. The peak-to-peak electric-field-induced lattice strains were then calculated following

$$\varepsilon_{hkl} = \frac{d_{hkl}^+ - d_{hkl}^-}{d_{hkl}^-}, \quad (6-6)$$

where d_{hkl}^+ and d_{hkl}^- are the (hkl) lattice spacings during the application of maximum positive and minimum negative electric fields, respectively, within a cyclic square-wave electric field. The (hkl) lattice plane spacings were determined from the best fits of the (hkl) diffraction peaks measured during the application of electric fields.

Piezoelectric properties are more often represented in terms piezoelectric coefficients rather than electric-field-induced strains. In order to make direct comparison with macroscopic piezoelectric coefficients, the measured lattice strains were subsequently transformed to equivalent lattice strain coefficients d_{hkl} , as given by

$$d_{hkl} = \frac{\varepsilon_{hkl}}{2E_0}, \quad (6-7)$$

for an applied electric field of amplitude $\pm E_0$.

In Eq. 6-7, the letter d in d_{hkl} is chosen because it represents an electric-field-induced strain coefficient. The commonly accepted variable in the field of piezoelectric materials for such a coefficient is “d.” Unfortunately, the same letter is used in the field of crystallography to represent interplanar lattice spacing, e.g. d in d_{hkl} .

6.3 Results and Discussions

6.3.1 Non-180° Domain Switching

Figure 6-5A shows the (002)-type diffracted intensities of the sample PLZT5248, corresponding to the positive and the negative segments of an applied square wave electric field of amplitude ± 750 V/mm and frequency 1 Hz, parallel to the direction of the applied electric field. As described in Section 6.2.5.1 the observed intensity interchange between the (002) and (200) diffraction peaks in Figure 6-5A correlates to the amount of 90° domain switching in the material induced parallel to the applied electric field direction. For $0 < \Phi < 90^\circ$, $\Delta\eta_{002}$ were

calculated from the observed intensity interchanges between the (002)-type diffraction peaks using Eqs. 6-3 and 6-5. Figure 6-5B shows the results of these calculations as a function of applied electric field amplitude for sample PLZT5248. It can be observed from Figure 6-5B that for all amplitudes of the applied electric field, $\Delta\eta_{002}$ decreases with increasing Φ and becomes negative for $\Phi > 50^\circ$.

In PLZT6040, the intensity interchanges between the (111)-type diffraction peaks are used to calculate the amount of $71^\circ/109^\circ$ domain switching, following Eqs. 6-4 and 6-5. In PLZT4060, the amount of 90° domain switching under cyclic electric fields is calculated from the intensity interchanges between the (002)-type diffraction peaks following Eqs. 6-3 and 6-5. The angular and amplitude dependence of $\Delta\eta_{111}$ for PLZT6040 and of $\Delta\eta_{002}$ for PLZT4060 are shown in Figure 6-5C and Figure 6-5D, respectively. For PLZT6040, $\Delta\eta_{111}$ beyond $\Phi > 70^\circ$ could not be calculated due to significantly decreased intensity of the $(11\bar{1})$ diffraction peak for these angles. Similar to the observed trends for PLZT5248, $\Delta\eta$ is observed to decrease with Φ for both PLZT4060 and PLZT6040 and becomes negative for $\Phi > 50^\circ$ (PLZT4060) and for $\Phi > 40^\circ$ (PLZT6040).

Figures 6-6A and 6-6B show the angular dependence of $\Delta\eta_{002}$ at different amplitudes of applied bipolar electric fields for undoped and Fe-doped varieties of MPB-adjacent tetragonal compositions. For both the samples PUZT5248 and PFZT4357, it is again observed that $\Delta\eta_{002}$ show an inverse dependence on Φ , and $\Delta\eta_{002}$ becomes negative for $\Phi > 50^\circ$.

For Figures 6-4 and 6-5, the errors in the reported values for $\Delta\eta$ were calculated from the estimated standard deviations in the measured intensities of the diffraction patterns. The error

bars for $\Delta\eta$ are of the order of the size of the data points for $\Phi = 0^\circ$ and about three times the size of the data points for $\Phi = 90^\circ$, with a gradual transition through $0^\circ < \Phi < 90^\circ$.

The angular dependence of $\Delta\eta_{002}$ indicates the energetic preference for non-180° domain switching for different crystallographic orientations of grains with respect to the applied electric field. Non-180° switching of domains is most favored when the polar axis after switching is parallel to the direction of the applied electric field. For $\Phi > 50^\circ$ in tetragonal ceramics and for $\Phi > 40^\circ$ in rhombohedral ceramics, a reverse trend in non-180° domain switching is observed which indicates a decreasing preference for the polar axis for these orientations. This is similar with observed trends for preferred orientation of ferroelastic domains in poled piezoelectric ceramics [30,67,68,69].

In addition to angular dependence, it can also be inferred from the above observations that the amount of non-180° domain switching in the different ceramic samples is a function of the amplitude of the applied cyclic electric field. In La-doped PZT ceramics, a monotonic increase in $\Delta\eta$ can be observed with increase in the amplitude of the applied electric field. Among the compositions studied, PLZT6040 shows the highest amount of non-180° domain switching, with a value of ~ 0.09 for $\Delta\eta_{111}$ parallel to the direction of an applied cyclic electric field of amplitude ± 800 V/mm. Under the same conditions of applied electric fields, the measured value for $\Delta\eta_{002}$ parallel to the electric field direction is ~ 0.08 for PLZT5248. For PLZT4060, $\Delta\eta_{002}$ is measured to be only ~ 0.015 parallel to the direction of the applied cyclic electric field of amplitude ± 1350 V/mm, indicating less extent of non-180° domain switching as compared to PLZT6040 and PLZT5248.

The observed values of $\Delta\eta_{002}$ for the samples PUZT5248 and PFZT4753 are less dependent on the amplitude of the applied electric field as compared to the observed behavior for

PLZT5248. Further, the amount of 90° domain switching in samples PUZT5248 and PFZT4753 are at least three times lower than what is observed for PLZT5248.

6.3.2 Calculation of Strain from Non-180° Domain Switching

Non-180° reorientations of ferroelastic domains within different grains should contribute to the macroscopic material strain as a result of anisotropic dimensional changes based on spontaneous crystallographic strains. The spontaneous crystallographic strain S_t (or S_r) is given by

$$S_t = \frac{d_{00l} - d_{l00}}{d_{l00}} \quad (6-8)$$

in tetragonal crystals, and

$$S_r = \frac{d_{kkk} - d_{kk\bar{k}}}{d_{kk\bar{k}}} \quad (6-9)$$

in rhombohedral crystals, where d_{hkl} is the spacing of the (hkl) lattice planes.

The contribution to the electric-field-induced macroscopic strain from non-180° domain switching within a grain will depend on the orientation of the grain with respect to the applied electric field direction. For example, this is illustrated in Figure 6-7 for a grain with 90° domains which has some of its domains aligned with their 001 poles oriented at angle Φ with respect to the electric field direction. Under the application of electric field, displacement of domain walls will cause an increase in the volume fraction of the domains which are favorably oriented with respect to the applied field at the expense of the less favorably oriented domains. This will cause a change in the dimension of the grain, an exaggerated illustration of which is shown in Figure 6-7. The projection of this distortion parallel to the direction of the electric field can be obtained by a second-order tensorial transformation [95].

The macroscopic strain due to all non-180° domain-wall induced distortions within a polycrystalline sample can be calculated by

$$\varepsilon_{non-180^\circ} = S \int_0^{\pi/2} [m\Delta\eta(\alpha)\cos^2\alpha] \sin\alpha d\alpha, \quad (6-10)$$

where $m=3$ for tetragonal ceramics and $m=4$ for rhombohedral ceramics. The factor $m\Delta\eta$ is the change in the multiple of random distribution (MRD) of the ferroelastic hkl crystallographic pole, along the sample direction α with respect to the applied electric field. The geometrical factor of $\cos^2\alpha$ in the integrand arises from a tensorial transformation of the domain-switching strain along the direction of the applied electric field. The factor $\sin\alpha$ describes the transformation from an elemental volume in the orientation space to an effective volume fraction within the sample [69,95].

Eq. 6-11 is applied to calculate the amount of strain due to non-180° domain switching in the different samples at various amplitudes of applied electric field. The coefficient of electric-field-induced strain due to non-180° domain switching $d_{non-180^\circ}$ is subsequently obtained following

$$d_{non-180^\circ} = \frac{\varepsilon_{non-180^\circ}}{2E_0}, \quad (6-11)$$

for an applied electric field of amplitude $\pm E_0$. The dependence of $d_{non-180^\circ}$ on the amplitude of applied electric fields is analyzed to understand the nonlinear field dependence of the non-180° domain switching strains.

6.3.3 Field Dependence of Non-180° Domain Switching Strains

Figure 6-8A shows the non-180° domain switching strain coefficient, $d_{non-180^\circ}$, for PZT ceramics with different crystallographic phases: PLZT6040 (rhombohedral), PLZT5248 (tetragonal with composition close to MPB with a c/a ratio equal to 1.0209) and PLZT4060

(tetragonal with a larger c/a ratio equal to 1.029). The largest strain contributions from non-180° domain switching are observed for tetragonal ceramics close to the MPB, with $d_{\text{non-180}^\circ}$ ranging from ~185 pm/V to ~352 pm/V, for applied electric field amplitudes of $\pm 100 < E_0 < \pm 850$ V/mm. Significant strain contributions due to non-180° domain switching are also observed for PLZT6040 ceramics with a rhombohedral phase, with a maximum $d_{\text{non-180}^\circ}$ of ~160 pm/V for an applied electric field of amplitude ± 800 V/mm. Due to the extremely small amount of non-180° domain switching in the highly tetragonal ceramics with a large c/a ratio, significant conclusions from diffraction experiments on these ceramics could only be determined at electric field amplitudes greater than ± 950 V/mm. The maximum $d_{\text{non-180}^\circ}$ measured for PLZT4060 is ~66 pm/V, for applied electric field of amplitude ± 1350 V/mm, which is significantly lower than the non-180° domain switching strains measured for rhombohedral and MPB-adjacent tetragonal PZT ceramics.

The effect of different dopants on the amount of non-180° domain switching strains can be observed from Figure 6-8B. Undoped and Fe-doped tetragonal PZT ceramics, with compositions close to MPB, show comparable non-180° domain switching strains under cyclic electric fields. In comparison, La-doping for MPB-adjacent tetragonal compositions lead to a more than three fold increase in the amount of non-180° domain switching strains. For example, under cyclic electric field of amplitude ± 800 V/mm, the values for $d_{\text{non-180}^\circ}$ are ~339 pm/V for PLZT5248, ~71 pm/V for PUZT5248 and ~57 pm/V for PFZT4753. This is not unexpected, as La-doping is known to enhance displacement of non-180° domain walls in PZT ceramics [6,7].

The coefficient of linear increase in $d_{\text{non-180}^\circ}$ with respect to the amplitude of the applied electric field $\pm E_0$ is determined by fitting the calculated values of $d_{\text{non-180}^\circ}$ following

$$d_{\text{non-180}^\circ}(E_0) = d_{\text{non-180}^\circ}^0 + \alpha_{\text{non-180}^\circ} E_0, \quad (6-12)$$

where $d_{non-180^\circ}^0$ is the intercept at zero amplitude of applied electric field. A non-zero value of $\alpha_{non-180^\circ}$ implies a nonlinear dependence of the non-180° domain switching strains on the amplitude of the applied electric fields. The electric-field-induced non-180° domain switching strains in La-doped PZT ceramics of rhombohedral and MPB-adjacent tetragonal compositions show nearly the same amount of nonlinearity with $\alpha_{non-180^\circ} \sim 0.2 \text{ (pm/V)(V/mm)}^{-1}$. Further, for MPB-adjacent tetragonal PZT ceramics, La-doping leads to a more than two fold increase in $\alpha_{non-180^\circ}$ as compared to undoped compositions, leading to greater nonlinearity in strain due to non-180° domain switching. A linear relationship is not observed between $d_{non-180^\circ}^0$ and E_0 for PLZT4060 and PFZT4753 – in both cases the displacement of non-180° domain walls are restricted, possibly due to internal stresses as a result of clamping due to large spontaneous strains (PLZT4060) or due to pinning of domain walls due to oxygen vacancies (PFZT4753), as mentioned in Chapter 4.

6.3.4 Electric-Field-Induced Lattice Strains

The different (hkl) lattice strain coefficients d_{hkl} for sample PLZT5248, parallel to the direction of applied electric field of amplitude $\pm E_0$, are shown in Figure 6-9A. It can be observed that the lattice strain coefficients increase with the amplitude of the applied electric field. The total electric-field-induced lattice strain is given by the product of $d_{hkl}(E_0)$ and E_0 . Consequently, if $d_{hkl}(E_0)$ increases with E_0 , hkl lattice strain is no longer a linear function of E_0 .

The coefficient of linear increase in d_{hkl} with respect to the electric field amplitude $\pm E_0$ is obtained through the following equation

$$d_{hkl}(E_0) = d_{hkl}^0 + \alpha_{hkl} E_0, \quad (6-13)$$

where d_{hkl}^0 is the intercept at zero amplitude of applied electric field. The degree of nonlinearity for the electric-field-induced lattice strains is provided by the parameter α_{hkl} .

For PLZT5248, the largest lattice strains are observed for the (111) crystallographic planes. As described in Section 1.2.1, in tetragonal PZT ceramics, the largest piezoelectric constants can be expected parallel to the polar axis of [001]. In contrast to general expectation, no significant amount of strain can be measured for the (00*h*) crystallographic planes, the normal to which is parallel to the polar axis. It is also noted that the largest nonlinearity is observed for the (111) lattice strains, with $\alpha_{hkl} \sim 0.4 \text{ (pm/V)(V/mm)}^{-1}$.

For samples PLZT6040 (rhombohedral) and PLZT4060 (tetragonal), some of the (*hkl*) lattice strains cannot be quantified since changes in the (*hkl*) peak positions were within the errors of measurement as obtained from the fitting of the *hkl* diffraction peaks. However, it is observed that the largest (*hkl*) lattice strains are observed for the (002) crystallographic planes for PLZT6040 and the (111) planes for PLZT4060. These observations are in agreement with previously reported experimental results for directions of maximum lattice strains in rhombohedral and tetragonal PZT ceramics [66,30,70,73,74]. The maximum lattice strain coefficients for the different samples are shown in Figure 6-9B. The maximum lattice strain coefficient for PLZT5248 is greater than that observed in PLZT6040 and PLZT4060. In addition, d_{111} in PLZT5248 and d_{002} in PLZT6040 exhibit larger nonlinearity than d_{002} in PLZT4060.

The (111) lattice strain coefficients for undoped, La-doped and Fe-doped tetragonal PZT ceramics with compositions close to the MPB are shown in Figure 6-9C. d_{111} in La-doped ceramics are more than three times than d_{111} in undoped and Fe-doped ceramics. Moreover, d_{111} in La-doped ceramics show a larger nonlinearity as compared to the undoped and Fe-doped ceramics.

The observed nonlinear (*hkl*) lattice strain coefficients are in contrast with the conventional assumption of linear piezoelectric lattice strains for ceramics. By comparing

Figures 6-7 and 6-8, it can be noted that field dependence of the largest lattice strains closely corresponds to the field dependence of the non-180° domain switching strains for the different samples. This could imply that non-180° domain switching affects the amount of electric-field-induced lattice strains in the material. The implications for this observation are further discussed in Chapter 7.

6.4 Conclusions

Using high-energy time-resolved X-ray diffraction, structural changes in PZT ceramics were evaluated under the application of cyclic electric fields. Non-180° domain switching within a material was measured at different angles with respect to the direction of the applied electric field. The total amount of strain in a sample due to the displacement of non-180° domain walls was evaluated through integration of the amount of non-180° domain switching over the complete orientation space. The amount of non-180° domain switching strain in PZT ceramics is found to be dependent on the crystal structure and composition of the material. The largest non-180° domain switching strains are measured for La-doped tetragonal ceramics with a composition close to the MPB; a maximum non-180° domain switching strain coefficient of ~352 pm/V was measured for an applied cyclic electric field of ±850 V/mm. In addition, for MPB-adjacent tetragonal PZT ceramics, La-doping is observed to increase the amount of non-180° domain switching strains by more than three times over the corresponding strains in undoped and Fe-doped compositions. This is observed from their respective values of non-180° domain switching strain coefficients, such as ~339 pm/V for PLZT5248 as compared to ~71pm/V for PUZT5248 and ~57 pm/V for PFZT4753. Evaluation of lattice strains under the application of cyclic electric fields shows that the maximum (*hkl*) lattice strain in a sample can be correlated to the amount of strain due to non-180° domain switching.

An important observation from the current investigation is that both the non-180° domain switching strain coefficients and the lattice strain coefficients can be functions of the amplitude of the applied electric field.

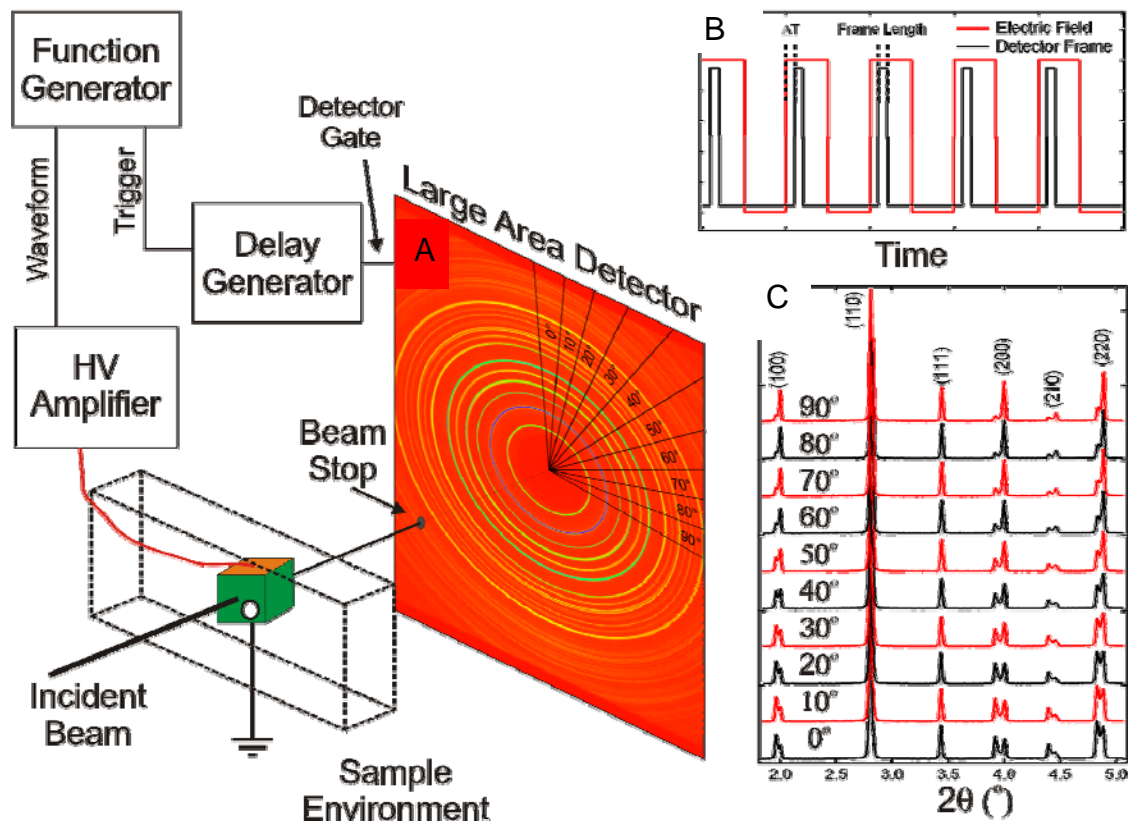


Figure 6-1. Details about experimental setup and timing electronics for *in situ* diffraction experiments. A) Schematic of time-resolved diffraction experimental setup showing an example large area diffraction image from a poled tetragonal PZT and the timing electronics. B) timing diagram for electric field waveform and detector frames. C) Individual “cakes” of the detector represent diffraction patterns with scattering vectors at various angles to the applied electric field. This is outlined when observing the integrated patterns of a poled ceramic.

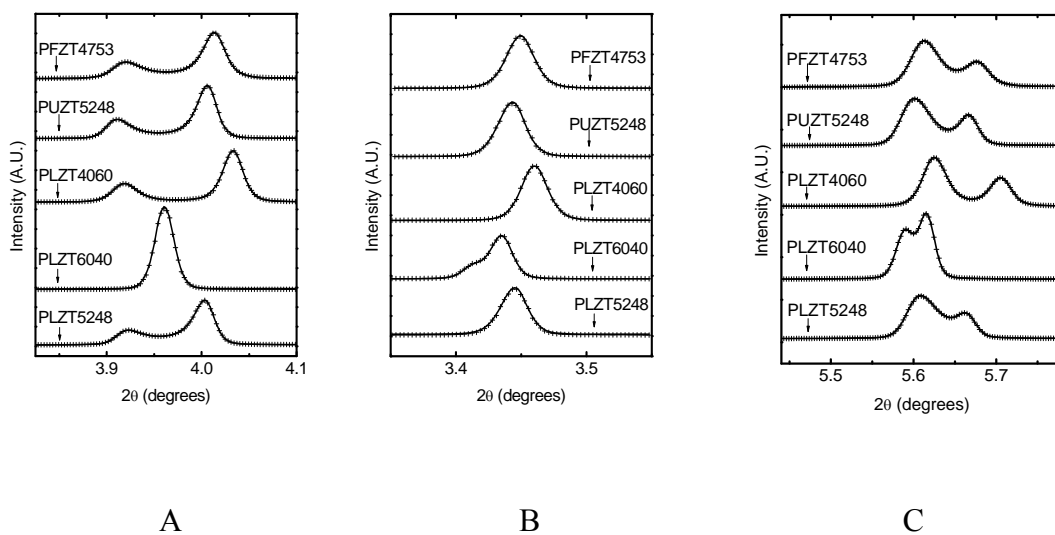
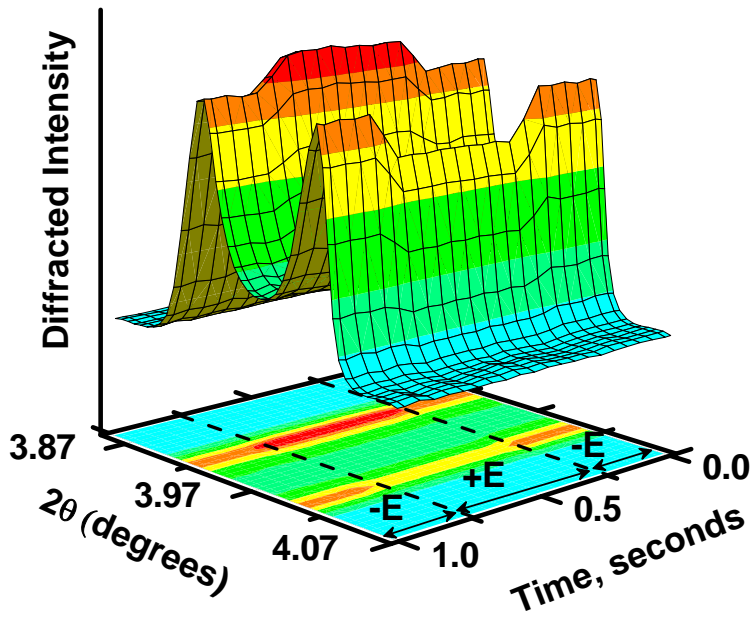
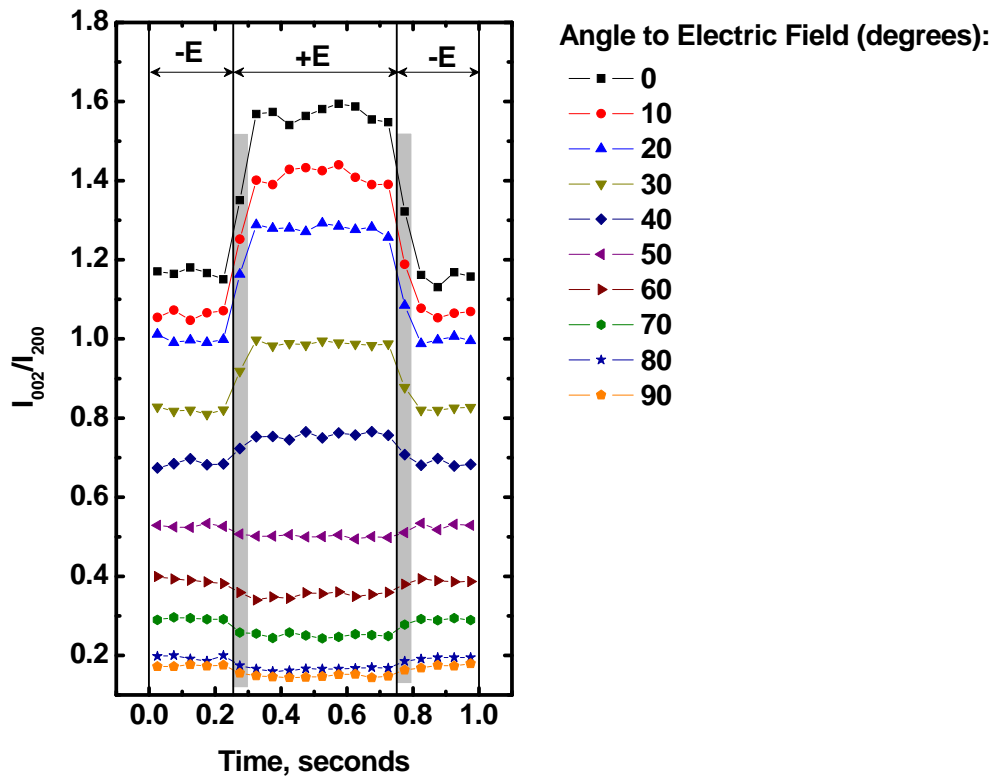


Figure 6-2. Specific diffraction peaks for the different samples used in the current experiments. A) (002)-type, B) (111)-type and C) (022)-type diffraction peaks. The diffraction patterns show a tetragonal phase for sample compositions with $Zr/Ti \leq 52/48$ and a rhombohedral phase for Zr/Ti ratio equal to 60/40.



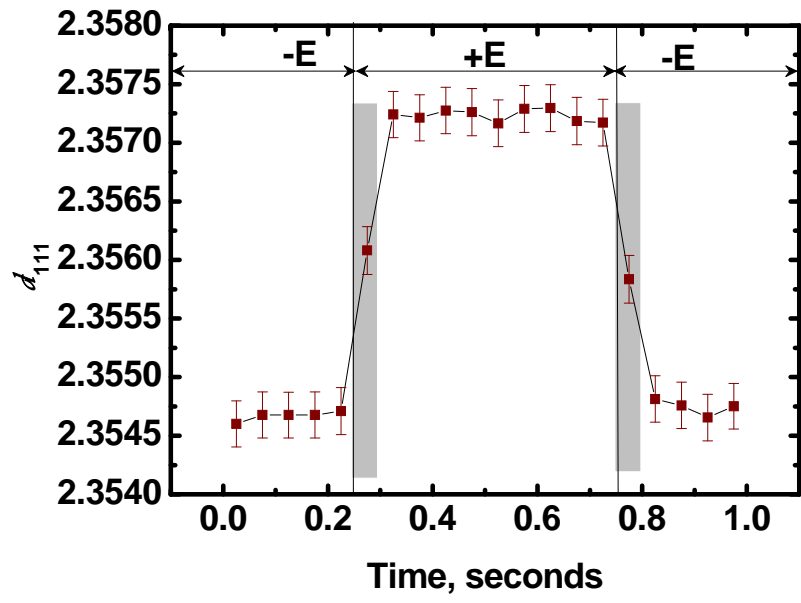
A

Figure 6-3. Time-resolved structural changes under cyclic electric fields. A) Time-resolved (002) and (200) diffraction peaks for the sample PLZT5248 during the application of a cyclic square wave electric field of amplitude ± 750 V/mm and frequency 1 Hz, along the direction of the applied electric field. Intensity interchange between the (002) and (200) diffraction peaks occur for positive and negative segments of the applied electric field cycle. B) The time dependence of the ratio of the integrated intensities of the (002) and (200) diffraction peaks, plotted as I_{002}/I_{200} . C) Time-dependent (111) lattice spacings d_{111} , parallel to the electric field direction. For both I_{002}/I_{200} and d_{111} , a transition period of < 0.05 s is observed during a change in the direction of the applied electric field.



B

Figure 6-3. Continued



C

Figure 6-3. Continued

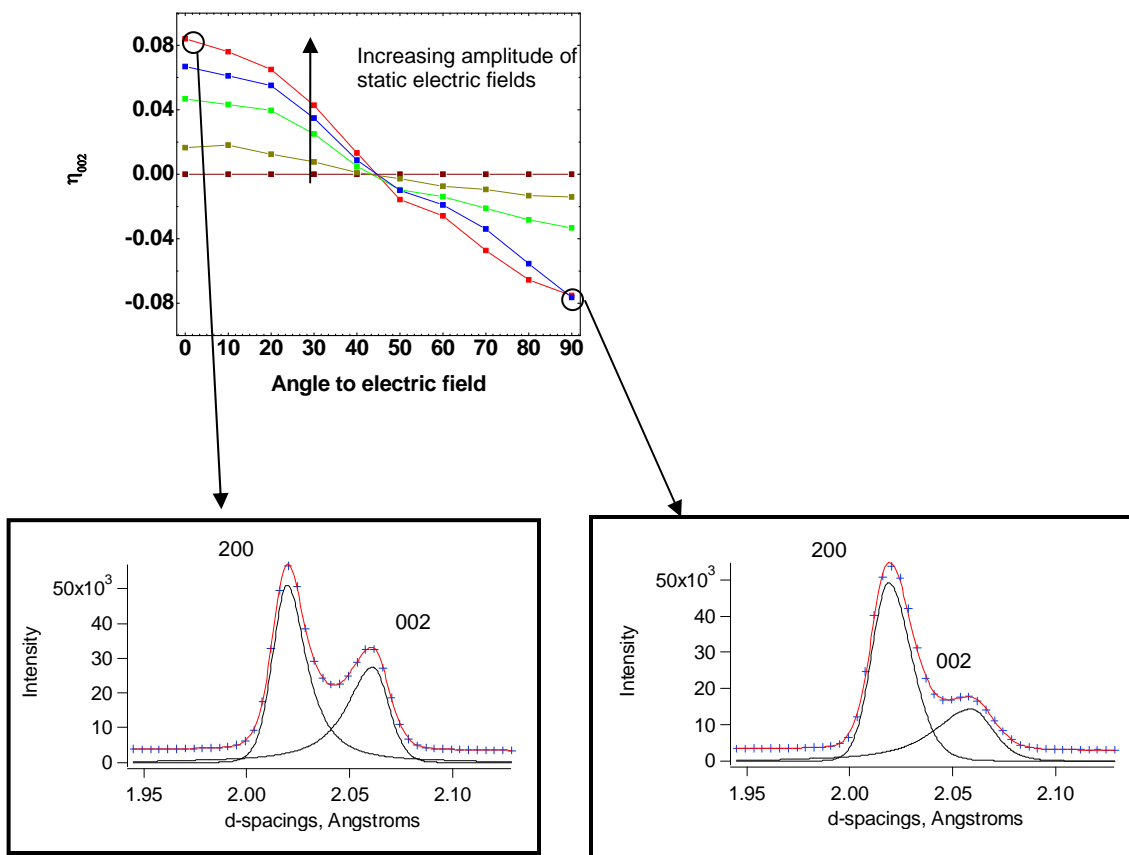
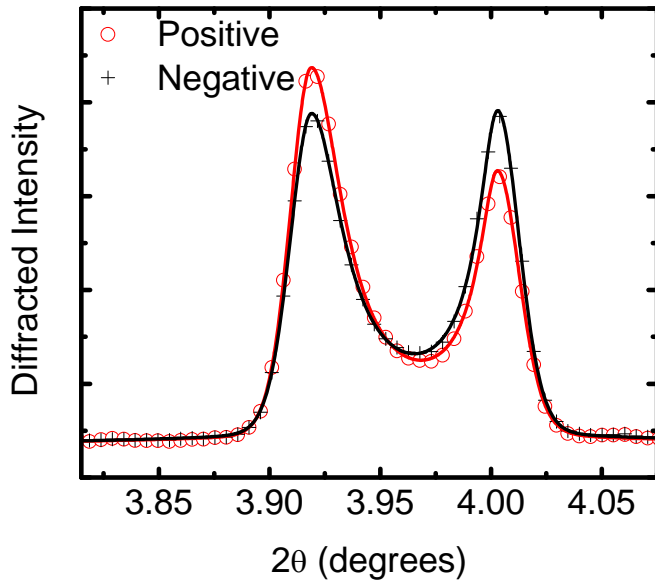
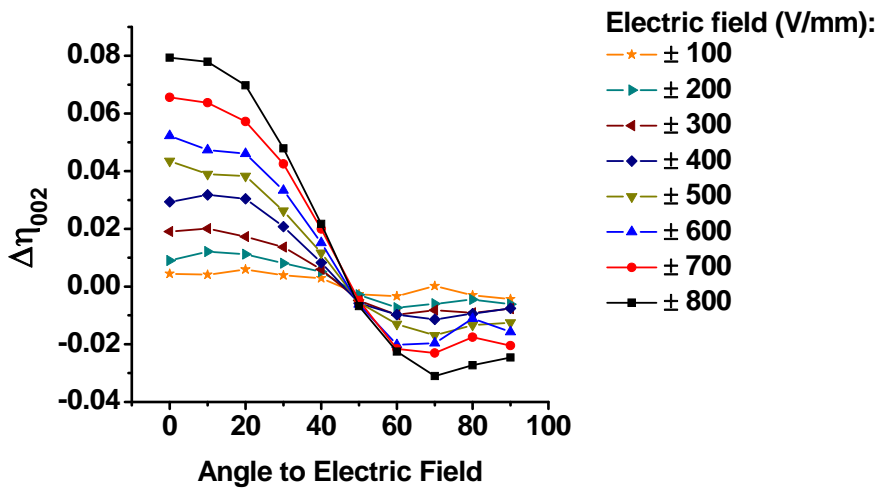


Figure 6-4. η_{002} as a function of field amplitude as well as orientation with respect to the direction of applied field, for an unpoled La-doped tetragonal PZT ceramic under the application of static electric fields. The measured and fitted (002)-type diffraction peaks corresponding to the particular values of η_{002} (marked by circles and indicated by arrows) are shown in the bottom section of the figure. For the fitted diffraction patterns, the deconvoluted 200 and 002 peaks are shown in black solid lines.



A

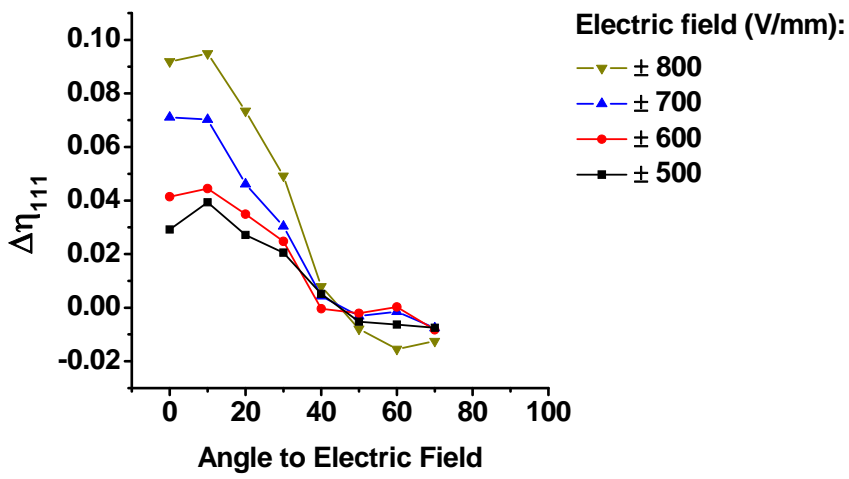


B

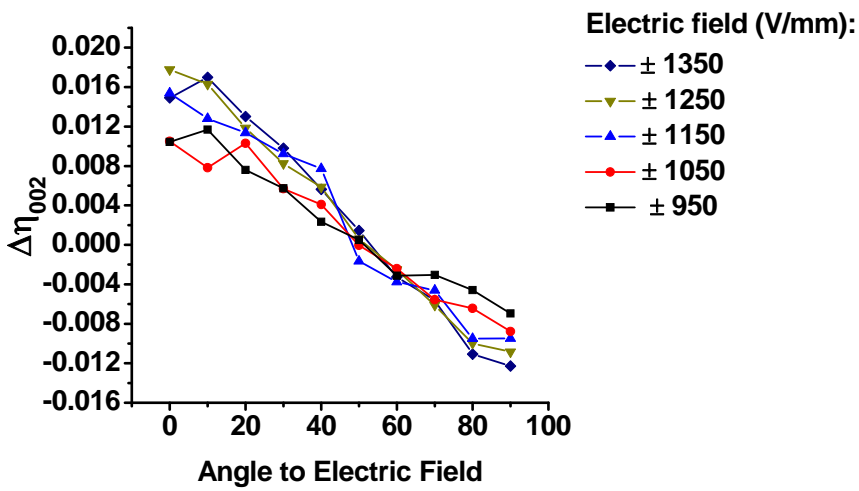
Figure 6-5. Change in volume fraction of non-180° domains in La-doped PZT ceramics under application of cyclic electric fields. A) The (002) and (200) diffracted intensities for the sample PLZT5248, corresponding to the positive and the negative segments of an applied cyclic square wave electric field of amplitude ± 750 V/mm and frequency 1 Hz, measured parallel to the direction of the applied electric field. The values of $\Delta\eta$,

for different angles with respect to the electric field direction, are calculated from the measured intensity interchanges between characteristic ferroelastic peaks at different azimuthal angles Φ . For clarity, data for amplitudes in steps of 100 V/mm are only shown, though measurements for this sample were taken at steps of 50 V/mm.

B) $\Delta\eta_{002}$ for sample PLZT5248. C) $\Delta\eta_{111}$ for sample PLZT6040. D) $\Delta\eta_{002}$ for sample PLZT4060. Error bars are not shown on the plot for clarity. Errors for $\Delta\eta$ are of the order of the size of the data points for $\Phi = 0^\circ$ and about three times the size of the data points for $\Phi = 90^\circ$, with a gradual transition through $0^\circ < \Phi < 90^\circ$.

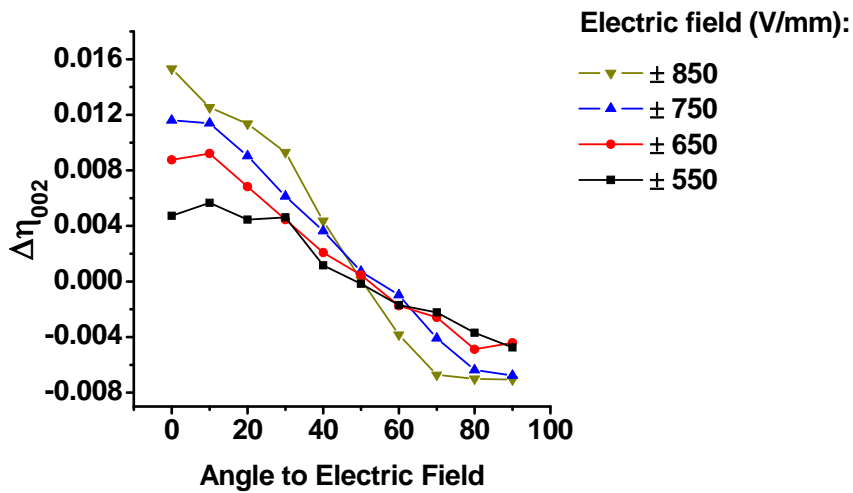


C

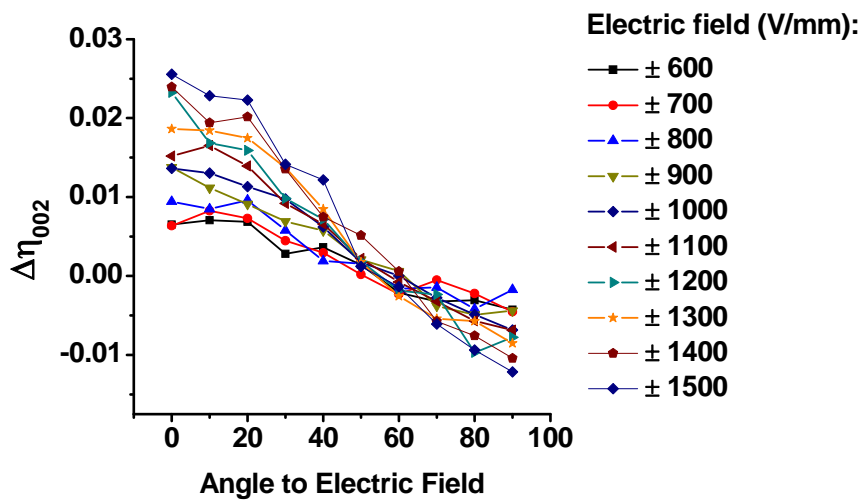


D

Figure 6-5. Continued



A



B

Figure 6-6. $\Delta\eta_{002}$ for different amplitudes of applied cyclic square wave electric fields, for A) sample PUZT5248, and B) sample PFZT4753. Error bars are not shown on the plot for clarity. Errors for $\Delta\eta$ are of the order of the size of the data points for $\Phi = 0^\circ$ and about three times the size of the data points for $\Phi = 90^\circ$, with a gradual transition through $0^\circ < \Phi < 90^\circ$.

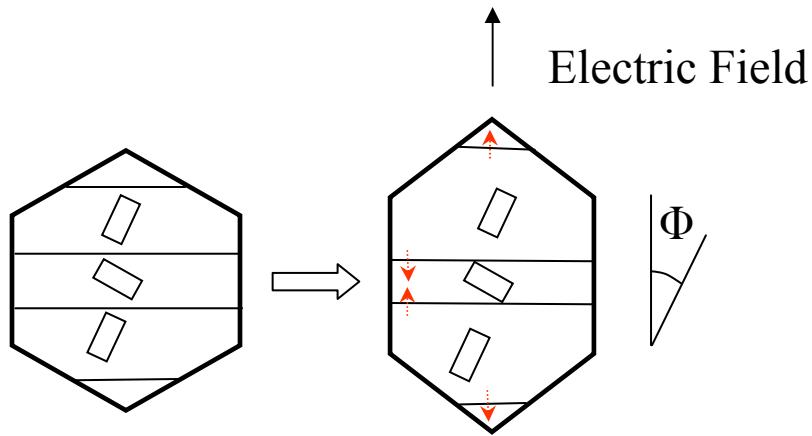
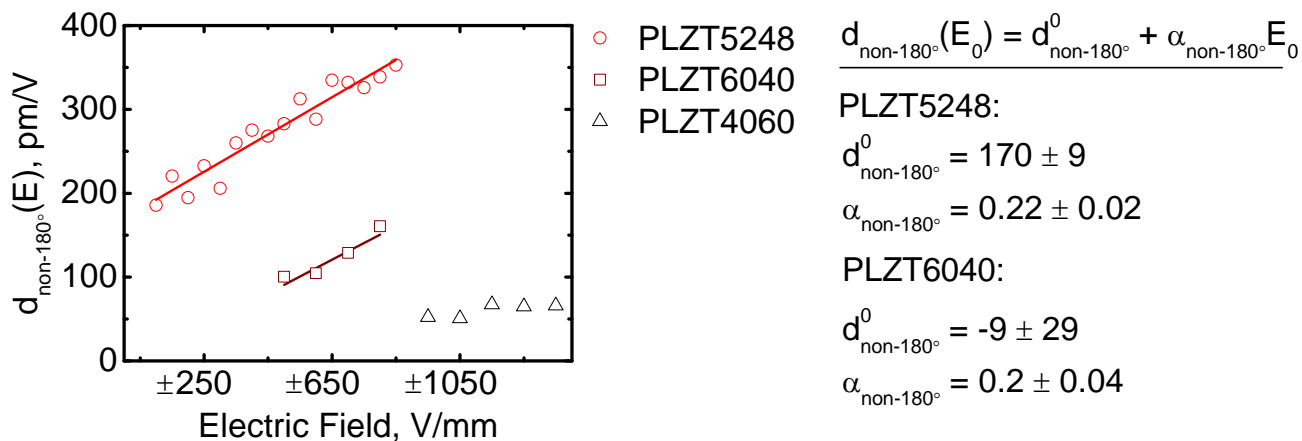
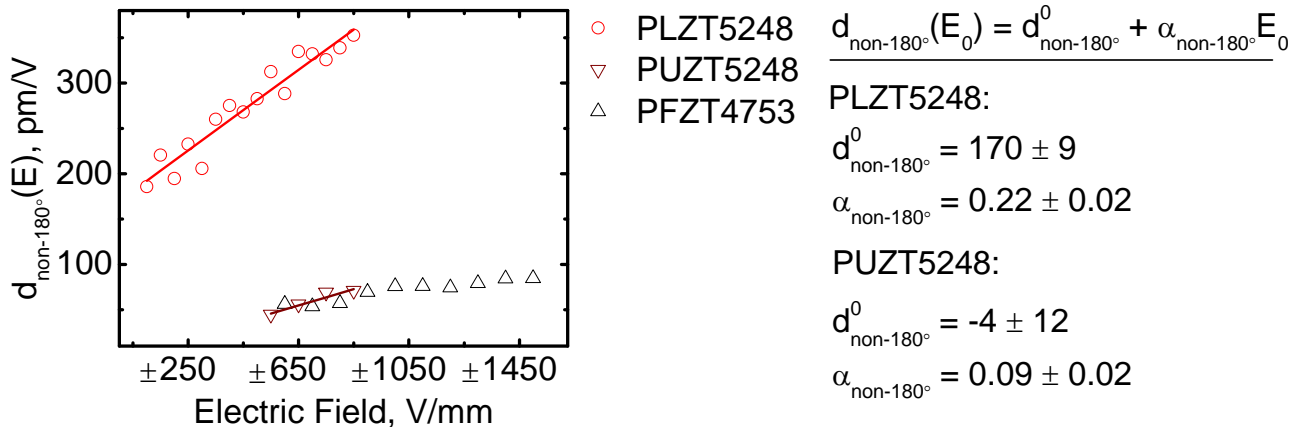


Figure 6-7. Illustration of strain due to non-180° switching of ferroelastic domains in a single grain. The domains with their long axes oriented at angle Φ with respect to the direction of the applied electric field expand, causing a change in the overall dimensions of the grain.



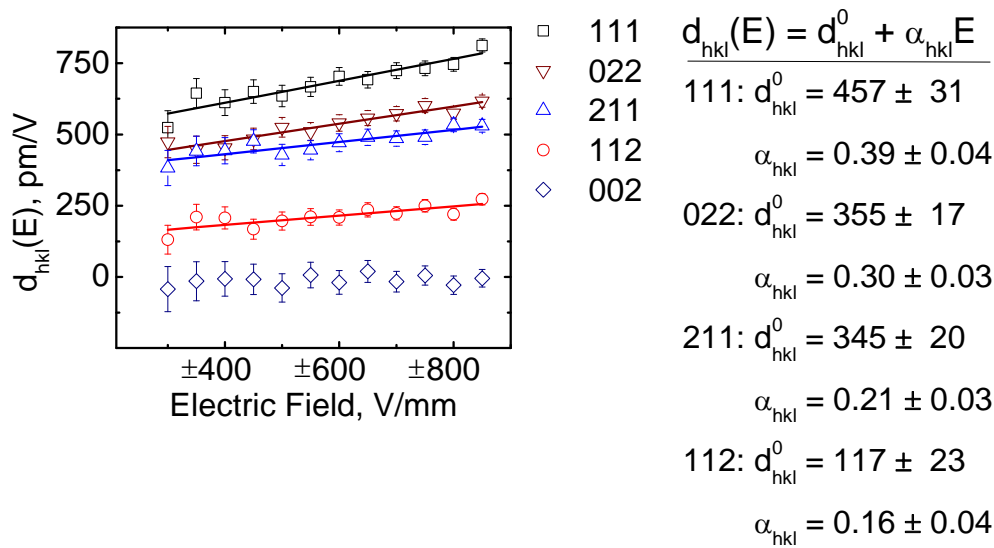
A



B

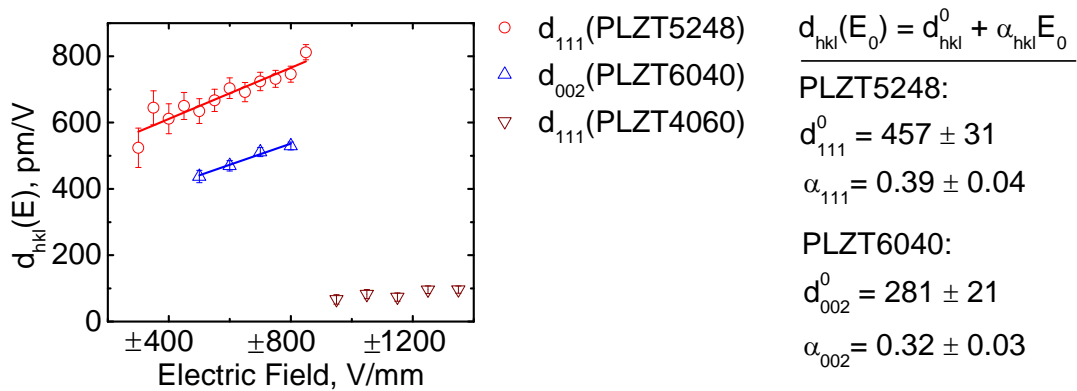
Figure 6-8. The coefficient of strain due to non-180° domain switching $d_{\text{non-180}^\circ}$ for PZT ceramics. A) $d_{\text{non-180}^\circ}$ for PZT ceramics with different crystallographic phases - PLZT6040 (rhombohedral), PLZT5248 (tetragonal with composition close to MPB) and PLZT4060 (tetragonal with a large c/a ratio). B) $d_{\text{non-180}^\circ}$ for PZT ceramics with different type of dopants for MPB-adjacent tetragonal compositions – PLZT5248 (La-doped), PUZT5248 (undoped), and PFZT4753 (Fe-doped). For compositions where a

linear relationship is valid, the relationship between the lattice strain coefficients and the applied electric field amplitudes are also shown.

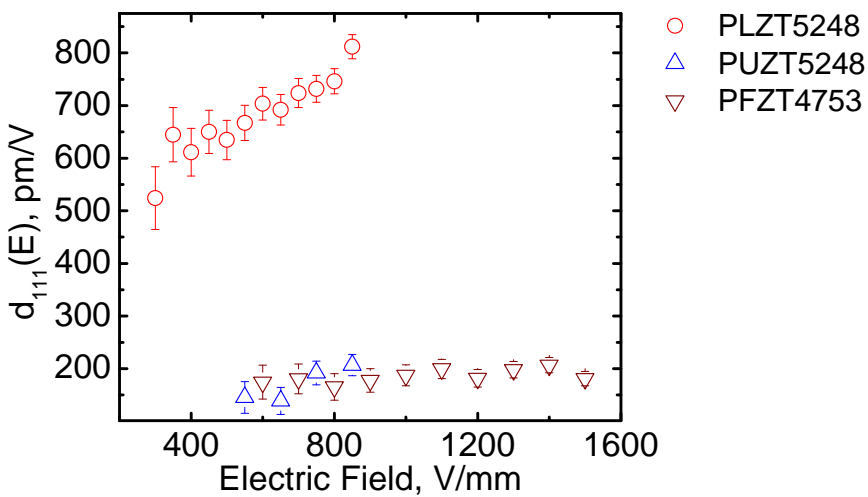


A

Figure 6-9. Electric-field-induced lattice strain coefficients in PZT ceramics. A) The different (hkl) lattice strain coefficients d_{hkl} , for sample PLZT5248, parallel to the direction of applied electric fields of amplitude $\pm E_0$, B) the maximum lattice strain coefficients for La-doped PZT ceramics with different crystal structures as a function of the amplitude of the applied cyclic electric fields - PLZT5248 (tetragonal with composition near MPB), PLZT6040 (rhombohedral), and PLZT4060 (tetragonal with a large c/a ratio). The linear relationships between the lattice strain coefficients and the applied electric field amplitudes are also shown. C) The maximum lattice strain coefficients for La-doped (PLZT5248), undoped (PUZT5248), and Fe-doped (PFZT4753) PZT ceramics of MPB-adjacent tetragonal compositions are compared for different amplitudes of applied cyclic electric fields.



B



C

Figure 6-9. Continued

CHAPTER 7 NONLINEAR CONTRIBUTIONS FROM STRUCTURAL MECHANISMS UNDER CYCLIC ELECTRIC FIELDS

In this chapter, the macroscopic piezoelectric nonlinearities presented in Chapter 4 are reconciled with the structural changes presented in Chapters 5 and 6. The objective is to develop a more fundamental understanding of piezoelectric nonlinearity with respect to the different structural mechanisms under cyclic electrical loading.

The effects of non-180° domain switching and lattice strains on macroscopic piezoelectric nonlinearity are separately discussed in Section 7.1 and Section 7.2, respectively. The cumulative effects of non-180° domain switching and lattice strains on macroscopic piezoelectric behavior are discussed in Section 7.3.

7.1 Effect of Non-180° Domain Switching Strains

Table 7-1 lists the values for α_d and $\alpha_{\text{non-180}^\circ}$ for the different samples studied. The coefficient of linear increase in the macroscopic piezoelectric coefficient d_{33} with respect to the applied electric field amplitude is denoted by α_d . The corresponding coefficient for non-180° domain switching strains is denoted by $\alpha_{\text{non-180}^\circ}$.

As explained in Chapter 4, $\alpha_d E_0$ is the electric-field-induced strain from irreversible extrinsic mechanisms. From the listed values of α_d for La-doped ceramics, it can therefore be concluded that the contribution from extrinsic mechanisms is minor in tetragonal compositions with a large c/a ratio and is significantly larger in rhombohedral and MPB-adjacent tetragonal compositions, among the investigated samples. This is consistent with the non-180° domain switching strain coefficients for the three different compositions presented in Figure 6-9A. In addition for MPB-adjacent tetragonal composition, a much higher value of α_d for La-doped ceramics is noted as compared to undoped ceramics. This is consistent with the non-180° domain switching strain coefficients for these ceramics (PLZT5248 and PUZT5248), measured using

time-resolved X-ray diffraction (Figure 6-9B). Though the irreversible extrinsic contributions for different crystallographic phases and dopants are consistent on many counts with the directly measured non-180° domain switching strains, a few disagreements could be noted as described below.

Macroscopic piezoelectric measurements show that the irreversible contributions from extrinsic mechanisms are similar for rhombohedral and MPB-adjacent tetragonal PZT ceramics (Figure 4-4A). However, from *in situ* diffraction experiments it can be observed that MPB-adjacent tetragonal PZT ceramics have nearly twice as much strain contribution from non-180° domain switching than what is observed for rhombohedral PZT ceramics (Figure 6-8A). In order to reconcile these observations, it is important to understand that *in situ* diffraction provides information about the total amount of non-180° domain switching in the material while only the irreversible extrinsic contributions are determined from the field-dependent macroscopic piezoelectric coefficients. Therefore it is possible that though the irreversible component of non-180° domain switching strains are similar for MPB and rhombohedral compositions, a greater amount of total (reversible and irreversible) non-180° domain switching occurs in MPB compositions. This is consistent with a non-zero intercept for non-180° domain switching strains at zero amplitude of applied electric field for La-doped MPB composition, as can be observed from Figure 6-8A.

Additionally, it can be observed from Table 7-1 that α_d is greater than $\alpha_{\text{non-180}^\circ}$ for the different compositions of PZT ceramics. This implies that the macroscopic electric-field-induced strains exhibit larger nonlinearity as compared to the non-180° domain switching strains. The relative nonlinear contributions from non-180° domain switching strains are evaluated using a procedure as described below.

For samples PLZT6040, PLZT5248 and PUZT5248, the relative nonlinear contributions from non-180° domain switching strains are calculated as $\alpha_{\text{non-180}^\circ} E_0 / d_{33}(E_0)$. This is done since these samples exhibit Rayleigh-type behavior for macroscopic electric-field-induced strains and a linear dependence of $d_{\text{non-180}^\circ}$ with respect to E_0 . In the above formulation, $d_{33}(E_0)$ is the longitudinal piezoelectric coefficient measured for applied electric field of amplitude E_0 . For sample PLZT4060, such an analysis was not undertaken since the non-180° domain switching strains could only be measured for electric fields outside the regime of linear dependence of $d_{33}(E_0)$ on E_0 . In Figure 7-1, the nonlinear contributions from non-180° domain switching are plotted along with the nonlinear extrinsic contributions evaluated in Chapter 4. For all the samples, it is observed that non-180° domain switching strains only partially constitute nonlinear extrinsic contributions. This implies that factors other than non-180° domain switching contribute to the macroscopic piezoelectric nonlinearity, which can include 180° domain switching [81] or nonlinear lattice strains [30]. Since 180° domain switching does not result in characteristic changes in diffracted intensities, the amount of 180° domain switching in the material under subcoercive cyclic electric fields cannot be directly determined from diffraction experiments. However, it is possible to measure lattice strains in the material under subcoercive electric fields from the shifts in the (hkl) diffraction peaks, as presented in Chapters 5 and 6. The effect of nonlinear contributions from lattice strains on macroscopic piezoelectric nonlinearity will be further explored in Section 7.3.

For sample PFZT4753, no linear relation was observed between the non-180° domain switching strain $d_{\text{non-180}^\circ}$ and applied electric field amplitude E_0 . Therefore, in this case the relative nonlinear contributions from non-180° domain switching strains were calculated as $\Delta d_{\text{non-180}^\circ} / d_{33}(E_0)$, where $d_{33}(E_0)$ is the longitudinal piezoelectric coefficient measured at the

amplitude E_0 of applied electric field. $\Delta d_{\text{non-180}^\circ}$ is given by $[d_{\text{non-180}^\circ}(E_0) - d_{\text{non-180}^\circ, \text{min}}]$, where $d_{\text{non-180}^\circ}(E_0)$ is the non-180° domain switching strain coefficient for applied electric field E_0 and $d_{\text{non-180}^\circ, \text{min}}$ is the non-180° domain switching strain for the minimum amplitude of applied electric field. $\Delta d_{\text{non-180}^\circ}/d_{33}(E_0)$ is compared with $\Delta d_{33}/d_{33}(E_0)$ as calculated for this sample in Chapter 4. For both macroscopic and non-180° domain switching strains, a sharp increase in nonlinear contributions can be observed for applied electric field amplitude of ~ 750 V/mm. This implies a threshold field of ~ 750 V/mm for non-180° domain wall displacement in this material. It is also observed that the nonlinear contributions from non-180° domain switching strains compare very well with overall extrinsic contributions. This is in contrast with the behavior observed for La-doped and undoped PZT ceramics. A possible explanation for this observation will be provided in Section 7.3.

7.2 Effect of Lattice Strains

The different hkl lattice strain coefficients for sample PLZT5248 were presented earlier in Section 6.3.3. For other samples, the calculated lattice strain coefficients for most of the hkl planes were zero within the errors of measurement and therefore further analysis of lattice strains in these samples were not carried out.

A rigorous estimate of macroscopic electric-field-induced strain from the different hkl lattice strains measured using diffraction will require formulation and execution of appropriate micromechanical models. However, good estimates of macroscopic equivalent strain can also be made from physically realistic weighting of strains obtained from multiple single peak diffraction measurements. A method for calculating macroscopic equivalent strain from weighted average of different hkl strains under the application of mechanical stress has been presented earlier [96]. A similar approach is adopted here for calculating the equivalent

macroscopic electric-field-induced strain from the different hkl strains measured under the application of cyclic electric fields.

The total longitudinal strain due to the lattice strains of all the grains within a ceramic sample can be calculated from a volume-weighted average of the different (hkl) lattice strains measured parallel to the applied electric field direction, that is,

$$\langle \varepsilon_{33,hkl} \rangle = \frac{\sum_{hkl} T_{hkl} m_{hkl} \varepsilon_{hkl}}{\sum_{hkl} T_{hkl} m_{hkl}} \quad (7-1)$$

where m_{hkl} is the planar multiplicity for the particular (hkl) crystallographic planes and T_{hkl} is the texture factor given by the MRD for the particular hkl crystallographic pole [73,96]. The values for T_{hkl} are determined from the intensities of the (hkl) diffraction peaks in the unpoled and poled state measured parallel to the applied electric field direction, following the method described in reference [69]. The values of T_{hkl} and m_{hkl} for certain hkl crystallographic poles are listed in Table 7-2.

Eq. 7-1 is equivalent to a Reuss approximation for calculating total strain in a composite of multiple constituents under isostress condition. Eq. 7-1 can be obtained based on the following assumptions: (1) the distribution of the grains with different hkl orientations within the diffracting volume is representative of the entire sample and the strains are cumulative for the different grains along a vertical section for the sample (a simplified schematic is provided in Figure 7-2) (2) each grain can contribute to only type of diffraction peak and that all grains contribute to a diffraction peak. The first assumption is not physically unrealistic if we consider uniform grains size (or distinct diffracting volumes) in the sample and the vertical section in Figure 7-2 to be uniform on average across the sample. The second assumption is not necessarily true and also is not strictly followed here since only certain hkl lattice strains are taken into account for calculation of equivalent strains. However, despite the limitations of the second

assumption, such an approach has been shown to provide realistic estimates of macroscopic equivalent strains [96].

By diving both sides of Eq. 7-1 by $2E_0$, we obtain

$$\langle d_{33,hkl} \rangle = \frac{\sum_{hkl} T_{hkl} m_{hkl} d_{33,hkl}}{\sum_{hkl} T_{hkl} m_{hkl}}, \quad (7-2)$$

where $d = \varepsilon / 2E_0$. $\langle d_{33,hkl} \rangle$ is the total effective lattice strain coefficient calculated from different (hkl) lattice strain coefficients presented in Figure 6-9A. The subscript 33 represent the lattice strain coefficients for the longitudinal direction. The calculated values of $\langle d_{33,hkl} \rangle$ are plotted in Figure 7-3 as a function of amplitude of applied electric field E_0 .

It can be observed from Figure 7-3 that $\langle d_{33,hkl} \rangle$ is a linear function of the amplitude of the applied electric field E_0 . The coefficient of linear increase in $\langle d_{33,hkl} \rangle$ with respect to the amplitude of the applied electric field E_0 is determined by fitting the calculated values of $\langle d_{33,hkl} \rangle$ following

$$\langle d_{33,hkl} \rangle(E_0) = d_{33,hkl}^0 + \alpha_{33,hkl} E_0, \quad (7-3)$$

where $d_{33,hkl}^0$ is the intercept at zero amplitude of applied electric field. The parameter $\alpha_{33,hkl}$ provides an index of the nonlinear nature of the total equivalent lattice strains with respect to the amplitude of the applied electric fields. Therefore, using a similar approach as adopted earlier, the relative nonlinear contributions from total equivalent lattice strains can be calculated as $\alpha_{33,hkl} E_0 / d_{33}(E_0)$. The effect and origin of nonlinear contributions from lattice strains are discussed in the next section

7.3 Cumulative Nonlinear Contributions from Different Structural Mechanisms

It is apparent from the above discussion that both non-180° domain switching strains and lattice strains can contribute to macroscopic piezoelectric nonlinearity under the application of cyclic electric fields. For sample PLZT5248, the cumulative nonlinear contributions from the two different mechanisms are plotted in Figure 7-4, which is slightly lower than the relative extrinsic nonlinear contributions calculated from macroscopic measurements.

It should be noted here that the current calculations for nonlinear contributions from the different structural mechanisms are based on certain physical assumptions, as mentioned earlier. The Reuss approximation provides an upper limit for the calculated total effective lattice strain coefficient, which can cause an overestimate of the calculated nonlinear contributions from lattice strains. The difference, between the total extrinsic nonlinear contributions (calculated from macroscopic d_{33} coefficients) and the cumulative nonlinear contributions from non-180° domain switching and lattice strains, can be explained due to other structural mechanisms such as 180° domain switching [81]. Nevertheless, based on the current analysis it is concluded that the dominant contributions to macroscopic piezoelectric nonlinearity comes from non-180° domain switching as well as nonlinear lattice strains.

Nonlinear contributions from electric-field-induced lattice strains are in contrast with a constant value for piezoelectric lattice strains derived from thermodynamic calculations [17-25]. This suggests that electric-field-induced lattice strains in polycrystalline ceramics are possibly influenced by extrinsic mechanisms like domain switching. A possible mechanism through which non-180° domain switching and lattice strains can be coupled in polycrystalline piezoelectrics has been suggested previously [30], which can be applied to interpret nonlinear lattice strains observed in the present investigation. According to the proposed mechanism, strains in neighboring grains within a polycrystalline matrix are expected to be coupled through

intergranular strain. For a certain distribution of grain orientations within a ceramic, existence of neighboring grains with different crystallographic orientations and consequently with different energetic preference for non-180° domain switching can be expected. The grains which undergo a larger amount of non-180° domain switching, under the application of electric fields, can impose constraints on the neighboring grains which are less favorably oriented for non-180° domain switching. Such intergranular interactions can lead to elastic strains for grains with different orientations, in addition to the intrinsic piezoelectric lattice strains, under applied electric fields. This mechanism is illustrated in Figure 7-5. A likely outcome for this proposed mechanism is a direct correlation between the nonlinearity for non-180° domain switching strains and lattice strains in piezoelectric ceramics with different compositions. This is observed for ceramics with different crystallographic phases and dopant types from the trends exhibited by non-180° domain switching strains and lattice strains, as shown in Figures 6-6 and 6-8. Further evidence of correlation non-180° domain switching and lattice strains can be observed from measurements performed under the application static electric fields, as presented in Figures 5-3A and 5-3B. For the proposed mechanism, it is also likely that the lattice strains are correlated to non-180° domain switching in the time domain under the application of applied electric fields. This is observed to be the case from Figures 6-3B and 6-3C.

It was earlier noted that for sample PFZT4753, nearly all the nonlinear contributions come from non-180° domain switching strains. In other words, no additional nonlinear contributions can be observed for this composition. However, according to the proposed mechanism in this section movement of domain walls are expected to create intergranular strain mismatch in polycrystalline ceramics which in turn can lead to nonlinear lattice strains. A possible explanation for such apparent contradiction can be provided as follows. It is possible that for

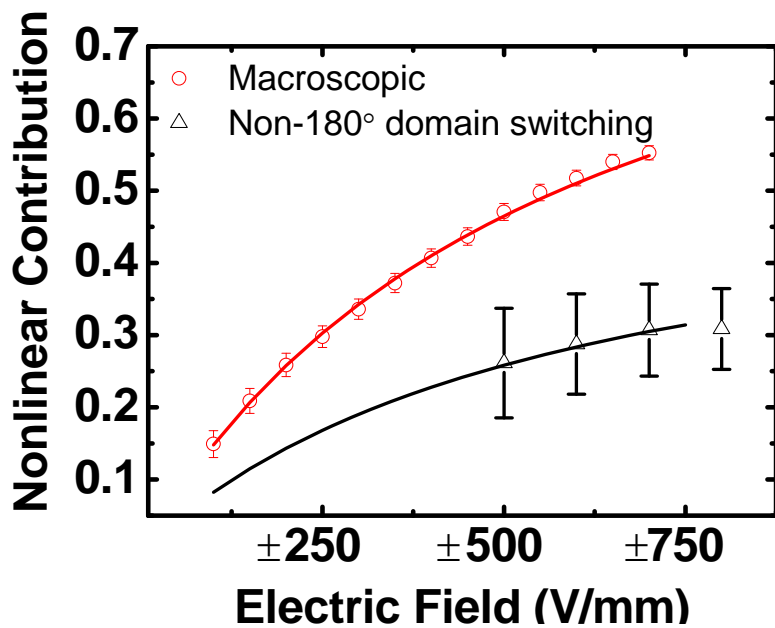
limited displacements of domain walls, the intergranular strain mismatches are accommodated within the grain boundaries rather than causing elastic lattice strains within the grains. However, additional verification of this hypothesis is necessary for a clearer understanding of the issue. One effective way to verify the underlying mechanism could be *in situ* Transmission Electron Microscopy (TEM) or Scanning Transmission Electron Microscopy (STEM), under application of electric fields.

7.4 Conclusions

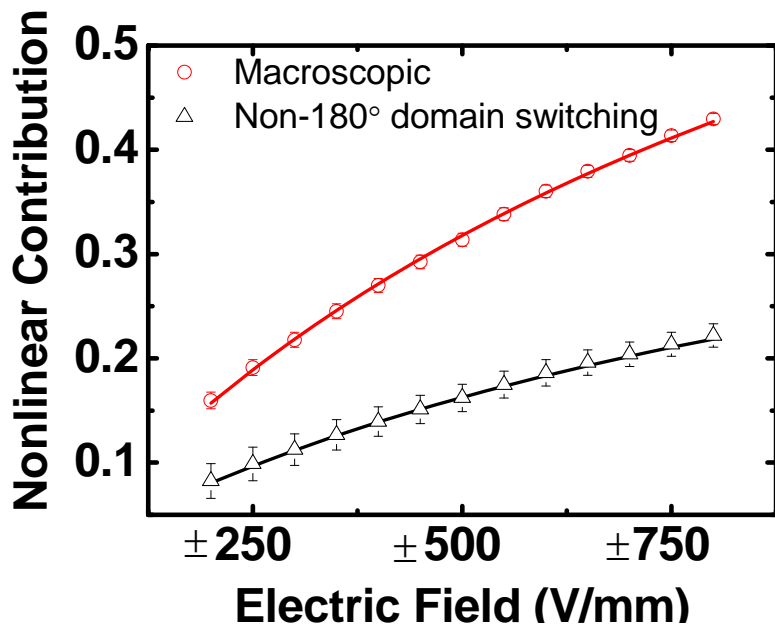
The nonlinear contributions to macroscopic electric-field-induced strains from non-180° domain switching in PZT ceramics were determined from *in situ* structural measurements under the application of cyclic electric fields. It was found that non-180° domain switching strains only partially contribute to the macroscopic piezoelectric nonlinearity for most compositions. For Fe-doped PZT ceramics, it was observed that the nonlinear contributions from non-180° domain switching strains almost exclusively contribute to macroscopic piezoelectric nonlinearity.

The nonlinear contributions from the different (*hkl*) lattice strains were determined for sample PLZT5248. The cumulative nonlinear contributions from non-180° domain switching and lattice strains show good agreement with the total nonlinear contributions calculated from macroscopic piezoelectric measurements.

A possible mechanism for the origin of nonlinear lattice strains from intergranular interactions in piezoelectric ceramics under the application of electric fields is presented.

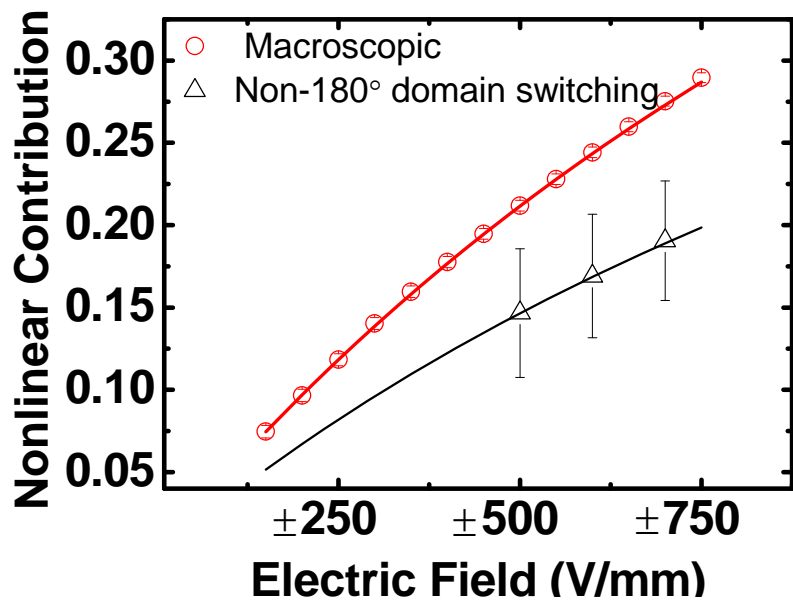


A

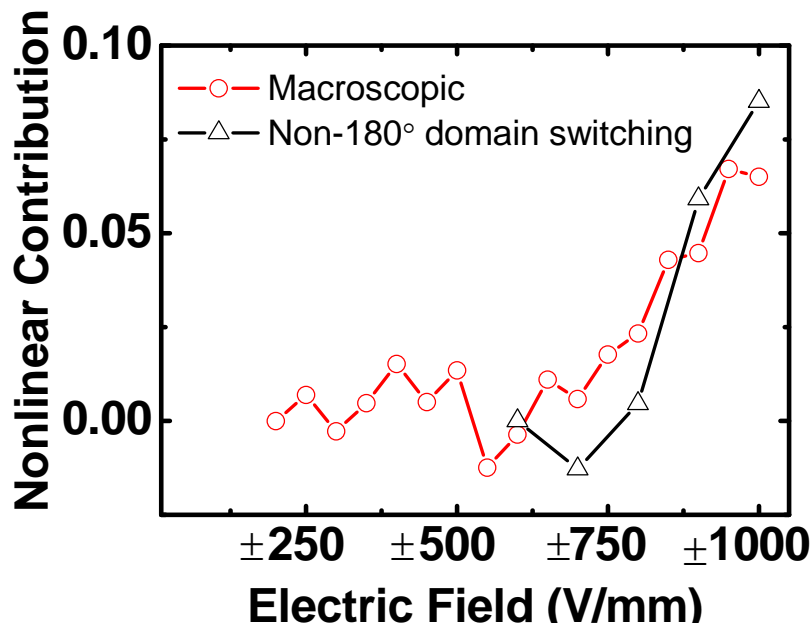


B

Figure 7-1. Nonlinear contributions to macroscopic electric-field-induced strains and nonlinear contributions from non-180° domain switching strains for samples A) PLZT6040, B) PLZT5248, C) PUZT5248, D) PFZT4753.



C



D

Figure 7-1. Continued

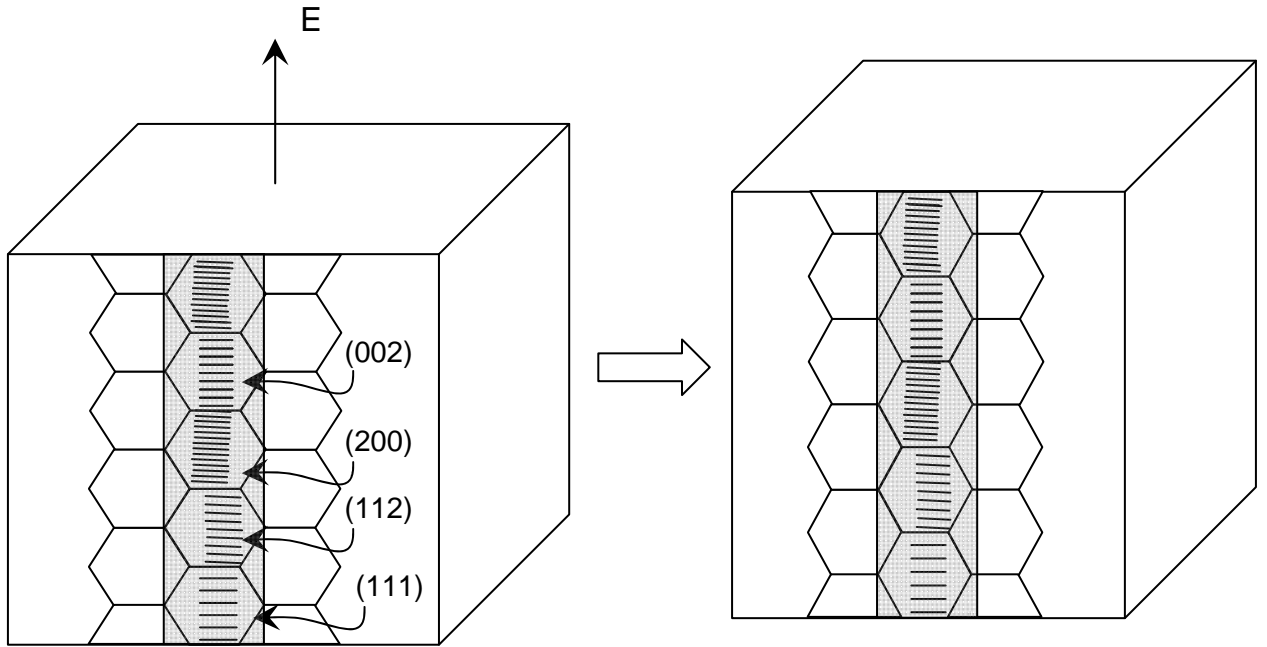


Figure 7-2. A simplified schematic illustration of cumulative addition of strains with different hkl orientations towards macroscopic electric-field-induced strain.

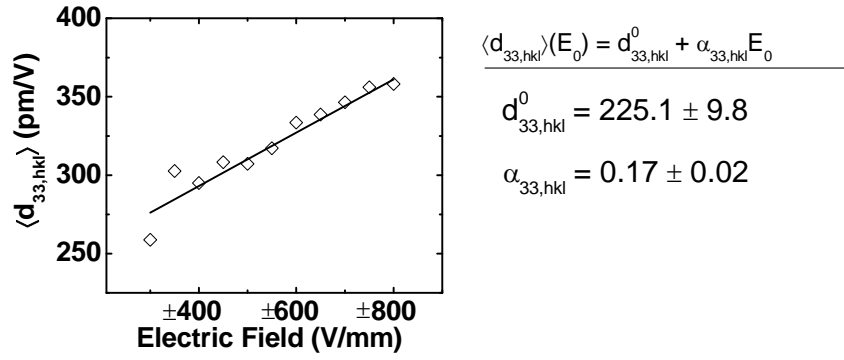


Figure 7-3. The total effective lattice strain coefficient as a function of the amplitude of the applied cyclic electric field.

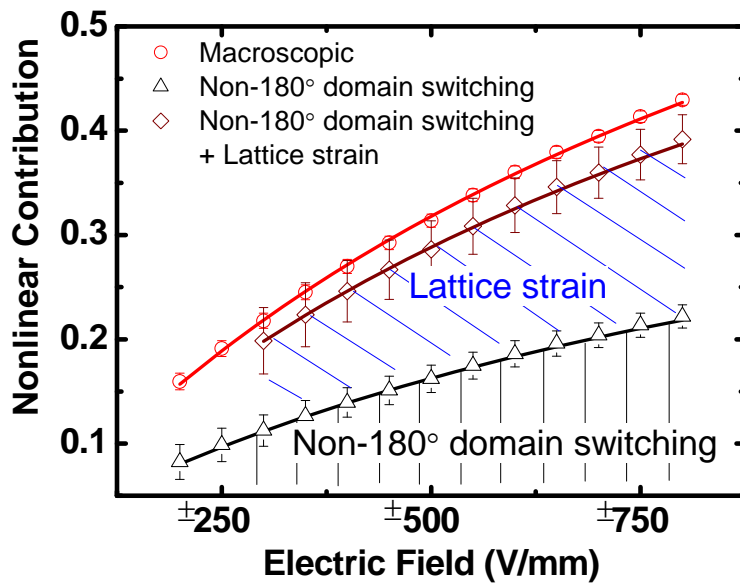


Figure 7-4. Nonlinear contributions to macroscopic electric-field-induced strain in sample PLZT5248 as a function of amplitude of applied electric field. The amount of nonlinear contribution from non-180° domain switching is marked in black. The amount of nonlinear contribution from total effective lattice strain is marked in blue. The cumulative nonlinear contribution from the two different mechanisms is in fair agreement with the relative nonlinear contributions calculated from macroscopic piezoelectric measurements.

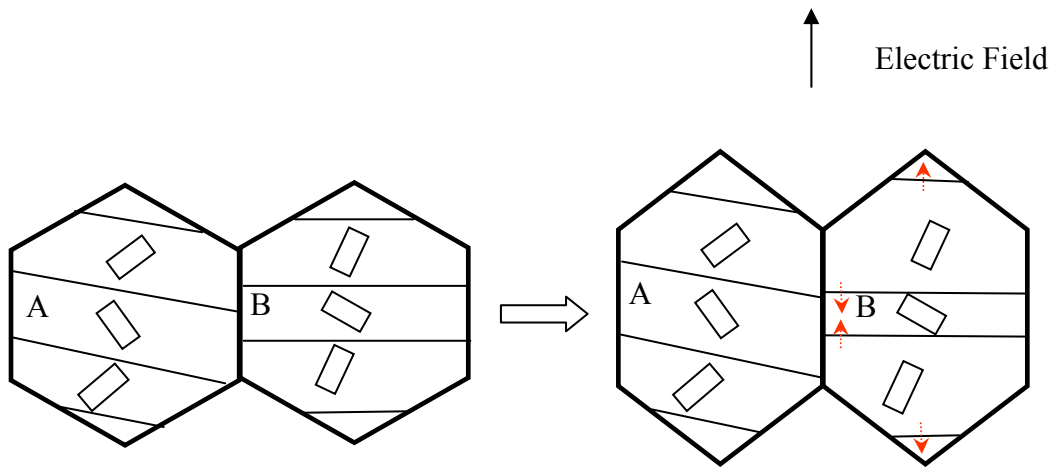


Figure 7-5. Illustration of intergranular interactions leading to elastic strains for grains with different orientations. In the above figure, domain wall displacements occur only in grain B under the application of electric field. However, grain A which shares a grain boundary with grain B is stretched due to intergranular interactions.

Table 7-1. α_d and $\alpha_{\text{non-180}^\circ}$ for the different samples studied.

Sample	α_d (pm/V)(V/mm) ⁻¹ (corresponding to macroscopic strains)	$\alpha_{\text{non-180}^\circ}$ (pm/V)(V/mm) ⁻¹ (corresponding to non-180° domain switching strains)
PLZT6040	0.36 ± 0.01	0.20 ± 0.04
PLZT5248	0.43 ± 0.01	0.22 ± 0.02
PLZT4060	0.07 ± 0.01	No linear relation
PUZT5248	0.13 ± 0.00	0.09 ± 0.02
PFZT4753	No linear relation	No linear relation

Table 7-2. The values of T_{hkl} and m_{hkl} for the different hkl crystallographic poles used to calculate the total effective lattice strain. The different hkl poles listed in the table are the ones for which significant lattice strains were observed.

hkl crystallographic pole	T_{hkl} (MRD)	m_{hkl} (Multiplicity factor)
111	1	1
002	1.82	0.33
200	0.59	0.67
112	1.46	0.33
211	0.77	0.67
022	1.59	0.33
220	0.70	0.67

CHAPTER 8 SUMMARY AND FUTURE WORK

8.1 Summary

Converse piezoelectric nonlinearity in ferroelectric PZT ceramics is analyzed from a unique perspective of electric-field-induced structural changes measured using time-resolved X-ray diffraction techniques. The ability to analyze the effects of underlying structural mechanisms on variations of piezoelectric properties in ferroelectrics under subcoercive electric fields is demonstrated using complementary macroscopic and time-resolved diffraction measurements.

PZT ceramics of different crystallographic phases and with different dopant additions were synthesized using a solid state synthesis route. Powders of the following nominal compositions were produced by the reactive calcination method: $\text{Pb}(\text{Zr}_x\text{Ti}_{1-x})\text{O}_3$ (PUZT, undoped) with $x = 0.52$, $\text{Pb}_{1-1.5z}\text{La}_z(\text{Zr}_x\text{Ti}_{1-x})\text{O}_3$ (PLZT, La-doped) with $x = 0.60, 0.52, 0.40$ and $z = 0.02$, and $\text{Pb}_{1+0.5z}[(\text{Zr}_x\text{Ti}_{1-x})_{1-z}\text{Fe}_z]\text{O}_3$ (PFZT, Fe-doped) with $x = 0.47$ and $z = 0.02$. Ceramics with 95-97% of theoretical densities were obtained by sintering the processed powders. The sintered ceramics exhibited good ferroelectric and piezoelectric properties, characteristic of their compositions.

Converse piezoelectric nonlinearities of the ceramic samples were investigated by measuring electric-field-induced strains as a function of amplitude of applied cyclic electric fields. The amplitudes of the applied electric fields were limited to below the macroscopic coercive field for the different samples. It was observed that the measured d_{33} coefficients for La-doped and undoped PZT ceramics follow Rayleigh law within certain ranges of applied electric fields, in contrast to Fe-doped PZT ceramics. The amount of nonlinear contributions from irreversible extrinsic mechanisms were calculated by application of Rayleigh law for instances where it was valid. Nonlinear extrinsic contributions in Fe-doped PZT ceramics were calculated from the field-dependence of their d_{33} coefficients. It was shown that the fraction of irreversible

extrinsic contributions is greater in the rhombohedral phase than in the tetragonal phase. The largest irreversible extrinsic contribution was observed to be about 55% of total electric-field-induced strain for La-doped rhombohedral PZT ceramics, for an applied electric field of ± 750 V/mm. In other words, ~ 298 pm/V of the macroscopic d_{33} value of 496 pm/V is contributed from extrinsic mechanisms. This can be interpreted as a result of greater possible switching of non- 180° domains in the rhombohedral phase. The effect of dopants on irreversible contributions was also determined for compositions close to the MPB. For MPB-adjacent tetragonal PZT ceramics, a maximum of 45% contribution from irreversible extrinsic mechanisms could be estimated for La-doped ceramics as compared to a maximum of 25% and 8% for undoped and Fe-doped ceramics respectively. Similar variations in extrinsic contributions with different crystallographic phases were reported earlier for direct piezoelectric response in PZT ceramics; under such loading, a maximum of 35% extrinsic contribution was observed for Nb-doped rhombohedral PZT ceramics [97]. However, the explicit derivations of extrinsic contributions for converse piezoelectric effect in PZT ceramics, as a function of phase and dopants, is unique from this current work.

The application of Rayleigh law for converse piezoelectric effect in PZT ceramics were further examined by determining the piezoelectric losses and harmonics of converse piezoelectric strain. Hystereses of strain-electric field curves under subcoercive electric fields were described consistently using Rayleigh relations, for La-doped and undoped PZT ceramics. From the calculated areas of the strain-electric field hysteresis loops, it was determined that the Rayleigh-type nonlinearity is the dominating mechanism for piezoelectric hysteresis in materials with linear variation of d_{33} with respect to electric field amplitude. However additional minor contributions to converse piezoelectric hysteresis were also observed, possibly from viscoelastic

motion of domain walls in the material. Analysis of harmonic components further emphasized the dominant nature of Rayleigh component towards macroscopic piezoelectric strain.

As described in Chapter 1, the Preisach model can be applied to provide a physical explanation of the Rayleigh law. In simplified terms, the Rayleigh behavior is obtained due to displacement of domain walls in a medium with randomly distributed energy barriers. Greater displacement of the domain walls is achieved across these energy barriers with increase in the amplitude of the applied electric field, thereby leading to greater domain switching and consequently greater macroscopic strains [4].

A more fundamental description of piezoelectric nonlinearity can therefore be provided from direct measurements of electric-field-induced structural changes including non-180° domain switching, as presented in Chapters 5 and 6. The amount of non-180° domain switching was evaluated from the intensity interchanges of characteristic ferroelectric diffraction peaks. The different hkl lattice strains were calculated from the shift in the 2θ positions of the (hkl) diffraction peaks.

Measurement of structural changes in tetragonal La-doped PZT ceramics under the application of static and dynamic electric fields using a laboratory diffractometer in reflection mode was described in Chapter 5. Under the application of static electric fields, 90° domain switching and 111 lattice strains, parallel to the direction of the applied electric field, were observed to correlate with the macroscopic strain-electric field hysteresis loop. However, differences were noted for values for $E_{\text{threshold}}$ and E_C calculated from macroscopic strain measurements and X-ray diffraction analyses. This effect is probably observed due to the fact that the X-ray measurements were taken under static electric fields unlike a continuous cyclic field as adopted for macroscopic measurements. A novel time-resolved X-ray diffraction

technique in the stroboscopic mode was adopted to perform measurement of structural changes under the application of cyclic electric fields of frequencies similar to macroscopic piezoelectric measurements. It was observed that both the amount of 90° domain switching and the 111 lattice strains increase with an increase in the amplitude of applied cyclic electric fields.

Time-resolved diffraction using high-energy X-rays in transmission mode was performed using an area detector at the European Synchrotron Radiation Facility (ESRF). High-energy X-rays enabled measurement of electric-field-induced structural changes from the bulk of the material. The Debye-Scherrer diffraction rings from the sample were collected in the stroboscopic mode using an area detector. The collected diffraction rings were segmented into separate azimuthal sectors. The pattern of the hkl diffracted intensity within each azimuthal sector Φ was indicative of the structural state of grains with their hkl poles approximately parallel to an angle Φ to the applied electric field. This experimental setup enabled *in situ* measurements of structural changes at different angles with respect to the direction of the applied electric field. The total amount of strain due to non- 180° domain switching in the material was evaluated by integrating the measured changes in the volume fractions of the non- 180° domains at different azimuthal sections. The non- 180° domain switching strains in PZT ceramics were observed to be characteristic of the crystal structure and dopant composition of the material. The largest non- 180° domain switching strains were observed for La-doped tetragonal ceramics with compositions close to the MPB. In addition, the non- 180° domain switching strain coefficients and the lattice strain coefficients showed characteristic dependencies on applied electric field amplitudes for different crystal structures and dopant variants.

The contributions from non- 180° domain switching towards macroscopic piezoelectric nonlinearities in PZT ceramics of different crystal structures and dopant variants were

determined in Chapter 7. For most compositions, it was observed that the non-180° domain switching strains only partially contribute towards macroscopic piezoelectric nonlinearity. For Fe-doped tetragonal PZT ceramics, the nonlinear contributions from non-180° domain switching strains were observed to be comparable with the irreversible extrinsic contributions determined from macroscopic piezoelectric measurements. A quantitative determination of nonlinear contributions from non-180° domain switching and lattice strains towards macroscopic piezoelectric nonlinearity was determined for La-doped tetragonal PZT ceramics with compositions close to MPB. It was observed that non-180° domain switching and total effective lattice strain equally contribute to macroscopic piezoelectric nonlinearity. It was proposed that nonlinear lattice strains result from intergranular constraints which in turn are caused by different amount of non-180° domain switching in grains with different orientations. The support for this proposed mechanism was noted from the observed correlations between the non-180° domain switching strains and lattice strains for different amplitudes and time periods of applied electric fields.

In addition, it was noted that the nonlinear contributions from non-180° domain switching and lattice strains do not exactly add up to the total extrinsic contributions determined from macroscopic piezoelectric measurements. It is possible that additional minor nonlinear contributions come from dynamic reorientation of 180° domains in the material during application of cyclic electric fields.

Based on the conclusions made from measurements of converse piezoelectric properties and electric-field-induced structural changes, the following mechanism for piezoelectric nonlinearity in ferroelectric PZT can be proposed. The underlying physical basis of piezoelectric nonlinearity is the displacement of domain walls, mostly separating non-180° domains.

However, the preference for non-180° domain switching depends on the hkl orientation of each individual grain with respect to the direction of the applied electric field. Neighboring grains with different hkl orientations experience different amounts of non-180° domain switching under the application of electric field. Since the grains are constrained in a polycrystalline matrix, elastic strains are resulted from mismatch in their electric-field-induced strains. In this scenario, the lattice strains are correlated to the amount of non-180° domain switching in the material. Consequently, both non-180° domain switching and lattice strains can be functions of amplitudes of applied electric fields. In other words, non-180° domain switching is the primary driving mechanism but not necessarily the exclusive contributor to macroscopic piezoelectric nonlinearity in ferroelectric PZT ceramics.

8.2 Suggestions for Future Work in this Area

A unique approach for analysis of field-dependent piezoelectric response in ferroelectric ceramics was provided in this work. It was shown that time-resolved diffraction can be employed to measure the nonlinear contributions from different structural changes to macroscopic strains under different conditions of applied cyclic electric fields. Similar approaches can be taken to understand variation of piezoelectric properties as a function of other variables as proposed below.

8.2.1 Nonlinearity in Direct Piezoelectric Behavior

Direct piezoelectric effect of ferroelectric ceramics is utilized in various sensor applications. As mentioned in Chapter 1, direct piezoelectric coefficients of PZT ceramics can exhibit Rayleigh behavior within certain range of applied ac mechanical stress. Though it is widely held that non-180° domain wall motion is responsible for nonlinearity in direct piezoelectric behavior, direct experimental evidence in this regard is lacking. It is therefore worthwhile to perform *in situ* structural measurements in these materials under the application of

ac mechanical stress. Experimental techniques similar to ones described in Chapters 5 and 6, can be applied to perform these measurements. Relative nonlinear contributions from different structural mechanisms can be calculated using an approach as describe in Chapter 7. Since 180° domain wall motion is absent under mechanical stress unlike application of electric fields, it would be interesting to observe whether that has any influence on the relative nonlinear contributions from different structural mechanisms.

8.2.2 Frequency Dependence of Piezoelectric Coefficients

Characteristic dependencies of direct piezoelectric effect on frequencies of applied cyclic mechanical stress were observed earlier [5,80]. Similar experiment on variation of converse piezoelectric coefficients as a function of frequency of applied electric field was performed for PLZT5248 samples, the result for which are shown in Figure 8-1. A linear variation of piezoelectric coefficients over frequencies of two orders of magnitude could be observed. It is generally held that such frequency dependence of piezoelectric coefficients originate from the time-dependence of domain wall motion in ferroelectric materials. However, as it was observed in this work, domain wall motion can influence other induced structural changes such as lattice strains. A systematic investigation of different structural changes under the application of electric fields at different frequencies is therefore necessary. *In situ* time-resolved diffraction can be an ideal technique for making these measurements.

Figures 8-2 and 8-3 show some results from preliminary investigations in this area. Figure 8-2 shows the time-dependent changes in the 111 lattice strains in PLZT5248 ceramic, parallel to the direction of the applied electric fields of different frequencies [98]. The data in Figure 8-2 was collected from measurements taken at beamline ID15B of ESRF. Similar experiments were performed on a commercial soft PZT (EC65) at the WOMBAT instrument at the Australian Nuclear Science and Technology (ANSTO). The 111 lattice strains for EC65 ceramics parallel to

the direction of applied cyclic electrical fields at different frequencies, are shown in Figure 8-3 [99]. No significant differences in the amplitude or time-dependence of the 111 lattice strains could be observed over a frequency range of 1 – 500 Hz for EC65 ceramics. This is in contrast with dynamic structural behavior observed in other PZT ceramics under cyclic electrical loading, where the 111 lattice strains and 90° domain switching were observed to be correlated in time [28]. This can imply the following two possibilities for the origin of this behavior in the current materials under applied cyclic electric fields: (1) the 111 lattice strain in this material is mainly intrinsic for these frequencies, or (2) the 111 lattice strains are correlated with non-180° domain switching [30,68], although domain switching occurs at time scales shorter than 30 μs and thus were not measurable using the experimental setup at ANSTO.

8.2.3 Temperature Dependence of Piezoelectric Nonlinearity and Frequency Dispersion

It is necessary to understand piezoelectric nonlinearity and frequency dispersion in ferroelectric ceramics at different operating temperatures. However, study of piezoelectric nonlinearity and frequency dispersion as a function of temperature do not figure largely in the literature.

An earlier study on the effect of temperature on frequency dispersion of modified lead titanate ceramics showed behavior typical for thermally activated mechanisms following Arrhenius law,

$$\tau = \tau_0 \exp(A/kT) \quad (8-1)$$

where τ is the relaxation time at temperature T , and A is the activation energy for the underlying physical mechanism [4]. From the observed behavior, the activation energy for mechanism responsible for frequency dispersion in modified lead titanate ceramics was estimated to be about 0.4 eV. However, the energy barrier for 90° domain wall motion in defect-free PbTiO₃ ceramics

has been determined from first-principle calculations to be ~ 0.02 eV at room temperature [100]. It was proposed that the presence of defects in modified lead titanate ceramics leads to the large increase in the activation energy of 90° domain walls which are associated with dopants and grain boundaries [4]. However, underlying this hypothesis is the assumption that domain wall displacements contribute exclusively to variable piezoelectric properties, which is not necessarily the case as is evident from the current work.

Direct measurements of changes in the volume fractions of non- 180° domains in piezoelectric ceramics at different temperatures can be obtained using time-resolved diffraction. Such measurements can also be used to directly determine the activation energy for non- 180° domain wall motions in the material under application of external fields.

8.2.4 Piezoelectric Nonlinearity and Frequency Dispersion in Lead-Free Piezoceramics

Due to concerns about detrimental effects of lead on environment, alternatives to PZT have been pursued intensely over the past decade [101]. However, for their effective adoption in sensor and actuator devices, it is necessary to study the stability of their piezoelectric properties under different applied conditions such as amplitudes and frequencies of applied electric fields or mechanical stress. Such studies are generally lacking in the literature. In a recent article, it has been shown that Rayleigh law can be applied to describe nonlinear dielectric and piezoelectric properties of lead-free sodium-potassium niobate (NKN) modified piezoceramics [102]. Interestingly, it is known that modified NKN ceramics show polymorphic behavior around room temperature [103]. It is therefore debatable whether the nonlinear contributions in such materials can comprise strains due to orthorhombic-to-tetragonal phase switching. Comprehensive analyses of nonlinear piezoelectric behavior and *in situ* diffraction experiments under application of electric fields or mechanical stress can potentially provide answer to such questions.

8.2.5 Piezoelectric Nonlinearity and Frequency Dispersion in Ferroelectric Thin Films

Extrinsic contributions to electric-field-induced strains are greatly reduced in ferroelectric thin films, particularly for film thickness of less than 1 μm [104-106]. This has been explained due to restricted non-180° domain wall displacements as a result of small grain sizes, residual stresses and high concentration of point and line defects in thin films as compared to bulk ceramics. Since the microstructure and hence the energy profile for domain wall displacements can be significantly different in thin films, investigations on structural origin of nonlinear piezoelectricity in these materials under subcoercive cyclic electric fields should provide new physical insights. Experimental techniques based on time-resolved X-ray diffraction as described in this work can be adopted for such an investigation.

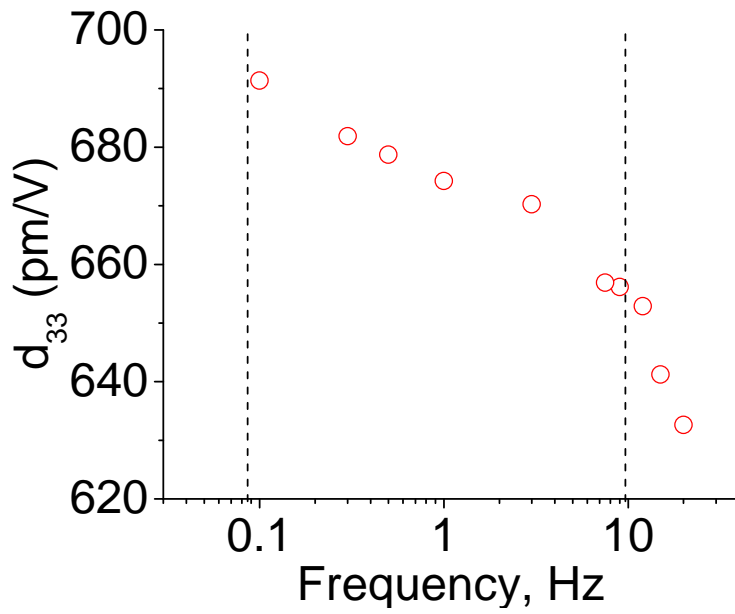


Figure 8-1. Variation of converse piezoelectric coefficients of PLZT5248, as a function of frequency of applied electric fields. The region of linear variation of d_{33} with respect to applied field frequency is shown by the dotted lines.

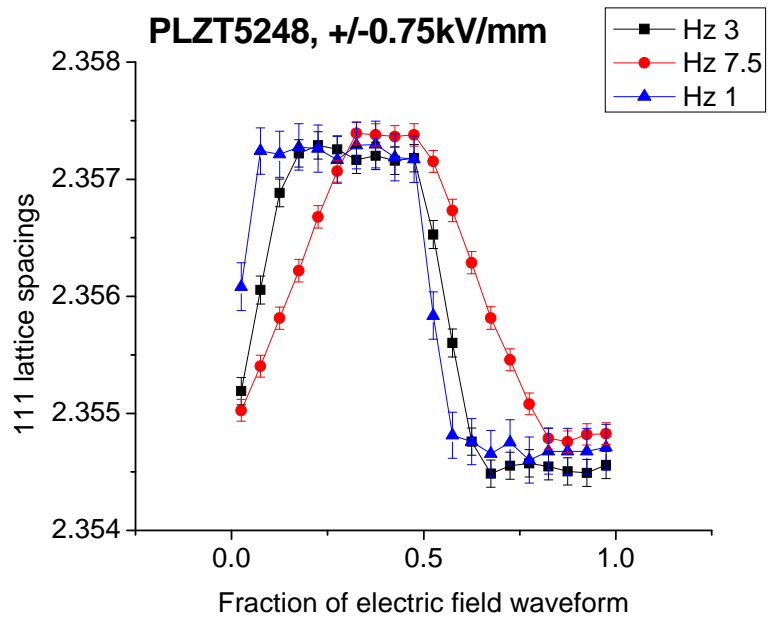


Figure 8-2. The time-dependent changes in the 111 lattice strains in PLZT5248 ceramic, parallel to the direction of the applied electric fields of different frequencies [98].

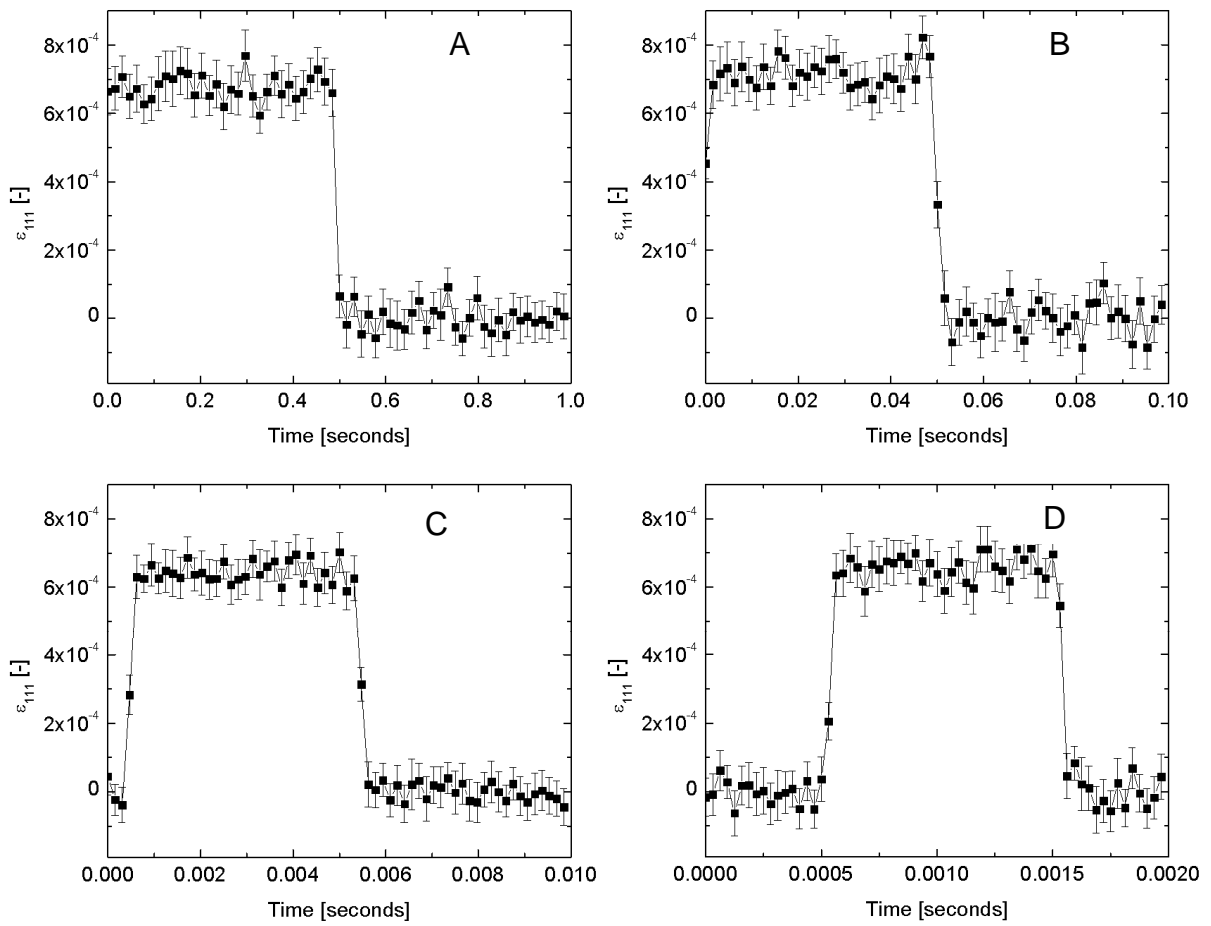


Figure 8-3. The electric-field-induced 111 lattice strains ε_{111} , as a function of time during application of a bipolar electric waveform of amplitude ± 0.4 kV/mm and frequencies of A) 1 Hz, B) 10 Hz, C) 100 Hz, and D) 500 Hz, for EC65 ceramics [99].

APPENDIX A
EFFECT OF SAMPLE DISPLACEMENT ON DIFFRACTION PEAK POSITION FOR A CPS
DETECTOR

A curved position sensitive (CPS) detector was used to collect *in situ* diffraction patterns under the application of electric fields, presented in Chapter 5. The longitudinal electric-field-induced strain causes a vertical displacement of the diffraction volume and therefore leads to a shift in the 2θ position of the diffraction peaks. The amount of shift in the 2θ position due to vertical sample displacement has been derived earlier [107].

The geometry for the diffraction setup is illustrated in Figure A-1A. The detector is in form of a circular arc of radius R with its center coincident with the center of the diffraction volume. The angle of the incident X-ray beam is ω with respect to the sample surface. Let us consider that the diffracted beam, corresponding to a particular hkl diffraction peak is recorded at a distance S along the circumference of the detector and it makes an angle φ with the surface of the sample and an angle 2θ with the incident X-ray beam. For this geometry, we have the following relations

$$\frac{\Delta\varphi}{\varphi} = \frac{\Delta S}{S}, \quad (\text{A-1})$$

and

$$\frac{\Delta\varphi}{\varphi} = \frac{2\Delta\theta}{2\theta - \omega}, \quad (\text{A-2})$$

where ΔS is the deviation in the measured position of the peak along the circumference of the detector and $2\Delta\theta$ is the error in the measured Bragg angle 2θ . For a vertical displacement of the sample surface by Δy , ΔS is given by

$$\Delta S = \frac{\Delta y(\sin 2\theta)}{\sin \omega} . \quad (\text{A-3})$$

Eq. A-3 becomes apparent from the illustration in Figure A-1B.

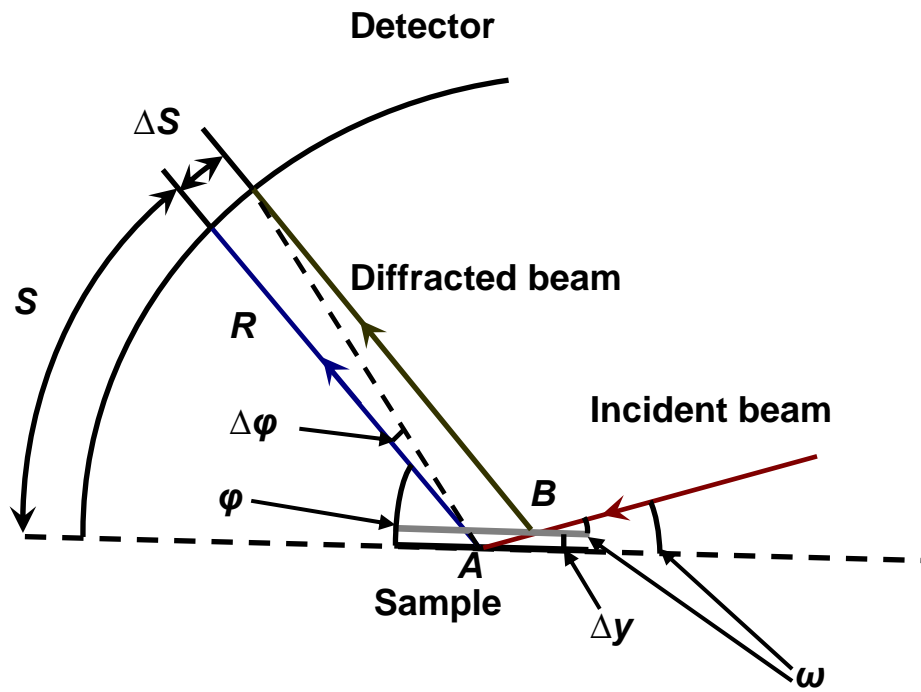
Since, for small-angle geometry ($\Delta\phi = \Delta S/R$) and ($\Delta\phi = \Delta\theta$), the following relation can be arrived using Eqs. A-1-A-3,

$$2\Delta\theta = \frac{\Delta y(\sin 2\theta)}{R \sin \omega} . \quad (\text{A-4})$$

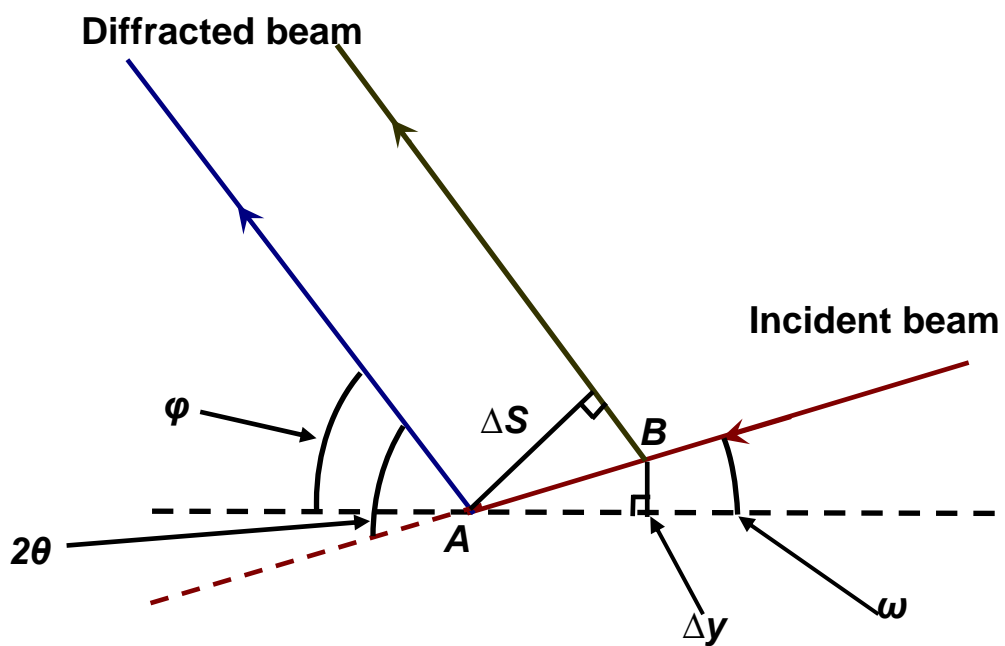
For a sample of 1 mm thickness (t) and a longitudinal piezoelectric coefficient (d_{33}) of 500 pm/V, the vertical displacement (Δy) of the sample surface is 1 μm for an applied electric field (E) of 2000 V/mm ($\Delta y = d_{33} \times E \times t$). The values for the other parameters in Eq. A-4 are: $R \sim 1$ m; $\omega \sim 10^\circ$; and $2\theta \sim 38.7^\circ$ for 111 diffraction peak. Applying Eq. A-4, the value of $2\Delta\theta$ for these values is 0.0002° .

For the applied cyclic electric fields of amplitude ± 550 V/mm, the shift in 2θ position of the 111 diffraction peak was measured to be 0.02° , for sample PLZT5248.

Therefore, the peak shift due to electric-field-induced lattice strains (0.02°) are at least two orders of magnitude higher than the peak shifts due to macroscopic sample displacement (0.0002°) at highest applied field amplitudes.



A



B

Figure A-1. Diffraction geometry and peak shift due to sample displacement, for a CPS detector.
 A) Diffraction geometry in reflection-mode with parallel incident X-ray beam, used for CPS detector B) Estimation of ΔS for a vertical sample displacement of Δy .

APPENDIX B STROBOSCOPIC DATA COLLECTION USING MCDWIN

The sequential steps followed for enabling stroboscopic data collection using MCDWIN software are described below:

1. The windows for MCDWIN and P7889 is opened by double-clicking the P7889 icon.
2. In the P7889 window, under settings tab, the option of “system” is selected. A new window, called “System definition”, opens. In this window, “Status Dig0” check box needs is selected. On right, the following check boxes: “Watch”, “Release a Start” and “Low at sweep preset reached”, are selected. The settings are saved on clicking “OK”.
3. A new window, called “P7889 Settings”, opens when the “Range, Preset...” icon is selected in the MCDWIN window. For both “Sync out TTL:” and “Sync out NIM:”, WINDOW is selected from the drop-down menus.
4. In the “P7889 Settings”, the option for sequential cycles is checked and the number of cycles for which data acquisition are enabled are specified in the field of sequential cycles. The number of patterns within each cycle is specified in the field for “y-range”. For the “Timepreset”, the input is approximately equal to time period for electric field cycle/ number of patterns in each cycle. The settings are saved on clicking “OK”.
5. A new cycle for data collection is started by clicking on the “Start” icon in MCDWIN window.
6. The TTL signal coming out of the P7889 data acquisition board is used to trigger a function generator. The length of the acquisition windows is monitored from the NIM signal. The TTL and the NIM signals are monitored together on an oscilloscope for synchronization of applied electric fields and collection of diffraction patterns.

The sequential steps for enabling stroboscopic data collection are shown in Figure B-1.

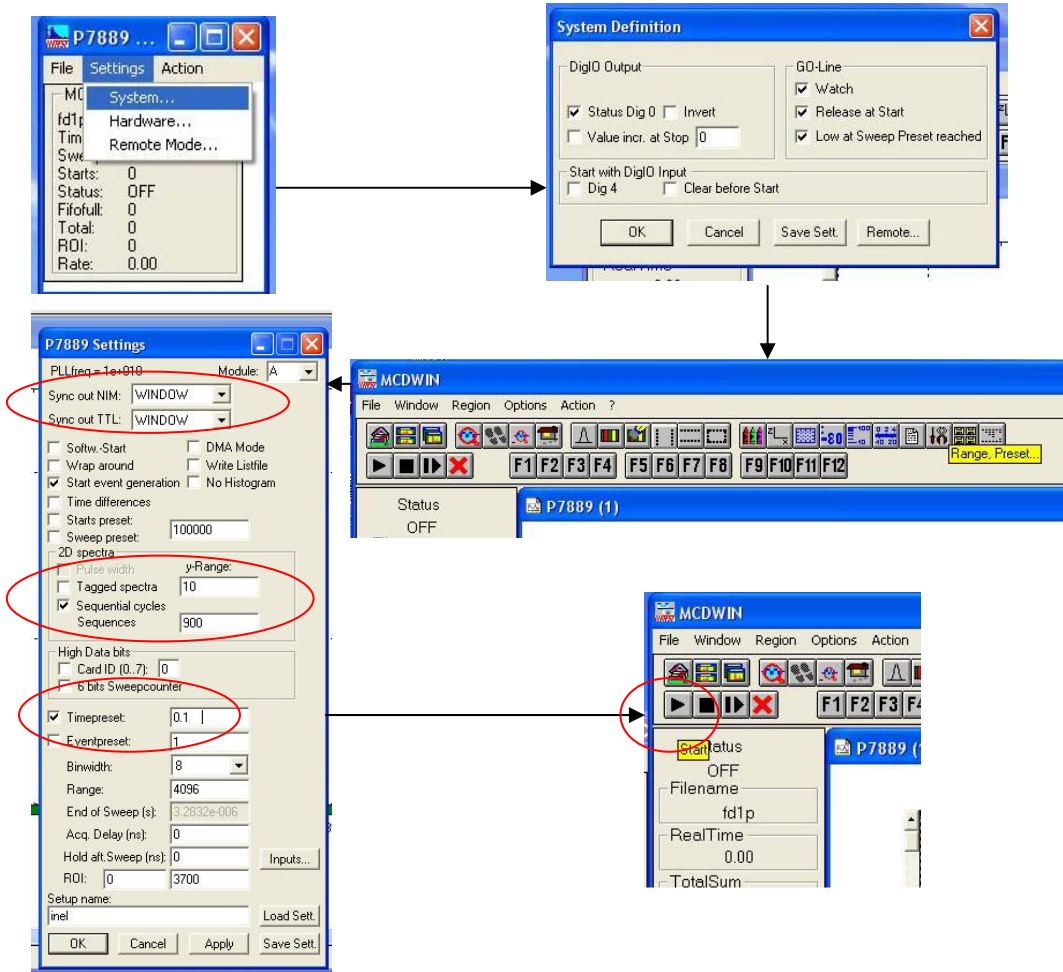


Figure B-1. Sequential steps for enabling stroboscopic data collection.

APPENDIX C
PENETRATION DEPTH OF X-RAYS IN PZT CERAMICS

The absorption of X-rays within ceramic samples of $\text{Pb}(\text{Zr}_{0.52}\text{Ti}_{0.48})\text{O}_3$ composition is calculated in order to estimate the typical penetration depths for X-rays in PZT ceramics used in this study.

The fraction of diffracted intensity G that comes from a given layer of material of thickness t , in reflection geometry, is given by [108]

$$G = (1 - e^{-\mu (\frac{1}{\sin \gamma} + \frac{1}{\sin \beta}) t}), \quad (\text{C-1})$$

where μ is the absorption coefficient of the material for X-rays; γ and β are the angles made by the incident and diffracted rays with respect to the sample surface, respectively. In case of diffraction in transmission mode, Eq. (C-1) can be modified as

$$G = (1 - e^{-\mu t}). \quad (\text{C-2})$$

The absorption coefficient for $\text{Pb}(\text{Zr}_{0.52}\text{Ti}_{0.48})\text{O}_3$ μ_{PZT} is given by

$$\mu_{PZT} = (w_{Pb}\mu_{Pb} + w_{Zr}\mu_{Zr} + w_{Ti}\mu_{Ti} + w_O\mu_O) \times \rho_{PZT}, \quad (\text{C-3})$$

where w represents the weight fractions and μ represent the mass absorption coefficients of the respective elements; ρ_{PZT} is the density of $\text{Pb}(\text{Zr}_{0.52}\text{Ti}_{0.48})\text{O}_3$ (theoretical density of 8 g/cm^3 is used in the present calculations).

A reflection geometry is adopted for *in situ* experiments using a laboratory diffractometer, as presented in Chapter 5. For Cu-K α radiation, the μ values are given below [108]:

$$\mu_{Pb} = 207.2 \text{ cm}^2/\text{g}$$

$$\mu_{Zr} = 91.2 \text{ cm}^2/\text{g}$$

$$\mu_{Ti} = 47.9 \text{ cm}^2/\text{g}$$

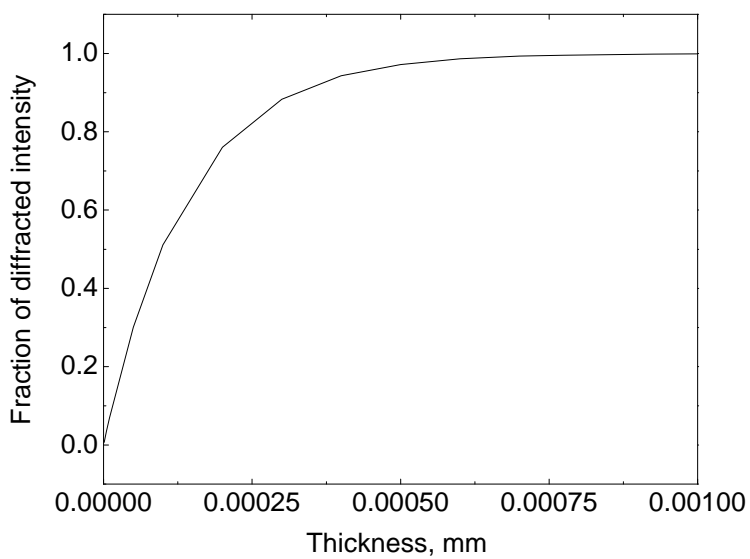
$$\mu_O = 16 \text{ cm}^2/\text{g}.$$

For representative hkl reflections measured at $2\theta \sim 40^\circ$ (111 and 002 reflections), $\gamma \sim 16^\circ$ and $\beta \sim 24^\circ$. For this geometry, G is calculated following Eqs. (C-1) and (C-3), and is shown in Figure C-1(a) as a function material thickness. It is observed that most of diffracted X-ray intensities come from a surface layer of less than 1 μm . In other words, structural changes only within a surface layer of 1 μm can be probed using a Cu-K α source.

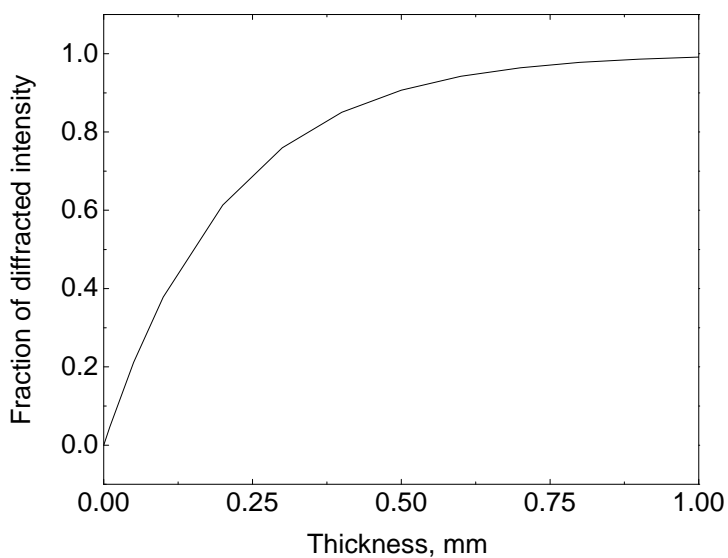
In Chapter 6, high-energy X-rays from a synchrotron source are used for *in situ* diffraction experiments in transmission mode. For incident X-rays of energy 87.80 keV (from a synchrotron source as described in Chapter 6), the μ values are given below [109]:

$$\begin{aligned}\mu_{Pb} &\sim 1 \text{ cm}^2/\text{g} \\ \mu_{Zr} &\sim 0.7 \text{ cm}^2/\text{g} \\ \mu_{Ti} &\sim 0.3 \text{ cm}^2/\text{g} \\ \mu_O &\sim 0.2 \text{ cm}^2/\text{g}.\end{aligned}$$

G is calculated following Eqs. (C-2) and (C-3), and is shown in Figure C-1(b) as a function of material thickness. It is observed that most of diffracted X-ray intensity comes from material of thickness $< 1 \text{ mm}$, which is the thickness of the samples used for high-energy diffraction experiments. Therefore, structural changes presented in Chapter 6 are representative of the bulk of the ceramic samples.



A



B

Figure C-1. Fraction of diffracted intensities as a function of thickness of diffracting volume for A) X-rays from a Cu-K α source, B) high energy X-rays (87.80 keV) from a synchrotron source.

APPENDIX D
IGOR CODES FOR ANALYSIS OF 2-DIMENSIONAL DIFFRACTION DATA

Some of the codes listed here were originally written by Dr. John Daniels of the ESRF and were modified for this work by the author of this document. Other codes were written by the author.

Igor code for loading text files containing intensity values of a 2-D diffraction image into waves of a Igor project

```
#pragma rtGlobals=1          // Use modern global access method.
Function loadfile1(wave0) // This function load data from a text file to waves in a Igor project

string wave0
variable n,i,j,k,l
variable file
string line
wave numwave
string filename
make /T sepwave
make /N=(2001) numwave // N is the number of points in entire range of two theta

for (n=0;n<17;n+=1) // n is the number of different amplitudes of applied electric fields
make /N=(2000,36,20) $("wave"+num2str(50+50*n)) // 36 is the number of azimuthal sectors
for the Debye rings

for (k=0;k<20;k+=1)

filename = "SamPLZT5248_0"+num2str(k+48+21*n)+".spr" // filename is the name of the text
files containing intensity values
open /R/P=pathname file as filename

wave cd = $("wave"+num2str(50+50*n))

    for(j=0;j<37;j+=1)
FReadline file,line
    if (strlen(line)>100)
LoadSpaceDellLine1 (line,sepwave,numwave)
        for (i=0;i<2001;i+=1)
            cd[i][j-1][k]=numwave[i]
        endfor
    endif
endfor

endfor
```

```

endfor
end
Function LoadSpaceDellLine1(line, sepwave,numwave) // This function reads each line in a text
file

    string line
    wave /T sepwave
    wave numwave
    variable j
    variable numtext = 0

    sepwave[0] = ""

    For (j=0;j<strlen(line)-1;j+=1)

        If (char2num(line[j]) != 32)

            Redimension /N=(numtext + 1) sepwave

            do
                sepwave[numtext] = sepwave[numtext] + line[j]
                j+=1
            while ((char2num(line[j]) != 32) && (j<strlen(line)-1))

            numtext = numtext+1

        Endif

    Endfor

    variable i
    for (i=0;i<2001;i+=1)
        numwave[i] = str2num(sepwave[i])
    endfor

End

```

Igor code for loading text files containing 2 theta values for a 2-D diffraction image into waves of a Igor project

```
#pragma rtGlobals=1          // Use modern global access method.
Function loadfileTT(wave0) // This function load data from a text file to waves in a Igor project
```

```
string wave0
variable n,i,j,k,l
variable file
string line
wave numwave
string filename
make /T sepwave
make /N=(2001) numwave // N is the number of points in entire range of two theta
```

```
for (n=0;n<17;n+=1) // n is the number of different amplitudes of applied electric fields
```

```
make /N=2000 $("TT_" + num2str(50+n*50))
wave cd = $("TT_" + num2str(50+n*50))
```

```
filename = "SamPLZT5248_0"+num2str(48+21*n)+".chi" // filename is the name of the text
files containing 2 theta values
open /R/P=pathname file as filename
```

```
for (i=0;i<2000;i+=1)
  FReadline file,line
  LoadSpaceDellLineTT (line,sepwave,numwave)
  cd[i]=numwave[0]
endfor
```

```
endfor
```

```
end
```

```
Function LoadSpaceDellLineTT(line, sepwave,numwave) // This function reads each line in a
text file
```

```
string line
wave /T sepwave
wave numwave
variable j
variable numtext = 0
```

```
sepwave[0] = ""
```

```
For (j=0;j<strlen(line)-14;j+=1)
    If (char2num(line[j]) != 32)
        do
            sepwave[0] = sepwave[0] + line[j]
            j+=1
        while ((char2num(line[j]) != 32) && (j<strlen(line)-14))
        Endif
    Endfor

numwave[0] = str2num(sepwave[0])

End
```

Igor code for extracting intensity for specific diffraction peaks for different azimuthal sectors

```
#pragma rtGlobals=1          // Use modern global access method.
function loadsegmentsang(wave0) // This function create waves containing diffracted intensities
of specific peaks such as 002 and 200, for different azimuthal sectors

string wave0
variable n,i,j,k

for (k=1;k<36;k+=1) // k is the azimuthal sector
make /N=(59,16) $("allfieldbi002neg"+num2str(k*10)) // 59 is the number of data points for
002 and 200 diffraction peaks
wave cd =$("allfieldbi002neg"+num2str(k*10))

for (n=0;n<16;n+=1)

    wave tf = $("wavebineg"+num2str(100+50*n))
    for (i=0;i<59;i+=1)
        cd[i][n] = tf[730+i][k]
    endfor

endfor

make /N=(59,16) $("allfieldbi002pos"+num2str(k*10))
wave ce =$("allfieldbi002pos"+num2str(k*10))

for (n=0;n<16;n+=1)

    wave te = $("wavebipos"+num2str(100+50*n))
    for (i=0;i<59;i+=1)
        ce[i][n] = te[730+i][k]
    endfor

endfor

endfor
end
end
```

Igor code for rebinning diffraction intensities with respect to time

```
#pragma rtGlobals=1          // Use modern global access method.
Function addtimepos(wave0) //This function rebins diffraction intensities with respect to time

string wave0
variable i,j,k,n

for (n=0;n<16;n+=1) // n is the number of different amplitudes of applied electric fields

make /N=(2000,36) $("wavebipos"+num2str(100+n*50))
wave cd = $("wavebipos"+num2str(100+n*50))
wave tf = $("wavebi"+num2str(100+n*50))

for (k=10;k<18;k+=1) // this code sums diffraction intensities from time period 10 to time period
18
  for (j=0;j<37;j+=1)
    for (i=0;i<2000;i+=1)
      cd[i][j] = cd[i][j] + tf[i][j][k]
    endfor
  endfor
endfor

endfor

end
```

Igor code for extracting peak parameters including ratio of integrated intensities of diffraction peaks constituting a doublet, such as 002 and 200 for a tetragonal sample, for different time periods during application of cyclic electric fields of different amplitudes. The function used here is double Asymmetric Pearson VII with equal strain approximation.

```
#pragma rtGlobals=1          // Use modern global access method.
function fit002200f(matname) // This function fits doublet peaks such as 002 and 200 and
calculate the ratio of integrated intensities of the doublet peaks

wave matname
variable i,j,k,field
string foldername
string componentpath

field =Dimsize(matname,1)

make /D/N=13 /O W_coef
make /D/N=13 /O W_sigma

FolderName = getdatafolder (0)

//Make new Data Folder for the processed data
  NewDataFolder /O root:$(FolderName):StandardDevs
  NewDataFolder /O root:$(FolderName):CalibratedData
  NewDataFolder /O root:$(FolderName):FitData
  NewDataFolder /O root:$(FolderName):Coefficients
  NewDataFolder /O root:$(FolderName):PeakComponents
  NewDataFolder /O root:$(FolderName):RunSpecs

//Make new waves to hold fitted data
  Make/D/N=(field) /O root:$(FolderName):Coefficients:$( "Baselines" )
  Make/D/N=(field) /O root:$(FolderName):Coefficients:$( "BackStep" )
  Make/D/N=(field) /O root:$(FolderName):Coefficients:$( "Center1" )
  Make/D/N=(field) /O root:$(FolderName):Coefficients:$( "Center2" )
  Make/D/N=(field) /O root:$(FolderName):Coefficients:$( "Y0Peak2" )
  Make/D/N=(field) /O root:$(FolderName):Coefficients:$( "Area Left Peak 1" )
  Make/D/N=(field) /O root:$(FolderName):Coefficients:$( "Area Right Peak 1" )
  Make/D/N=(field) /O root:$(FolderName):Coefficients:$( "Area Left Peak 2" )
  Make/D/N=(field) /O root:$(FolderName):Coefficients:$( "Area Right Peak 2" )
  Make/D/N=(field) /O root:$(FolderName):Coefficients:$( "m variable left peak 1" )
  Make/D/N=(field) /O root:$(FolderName):Coefficients:$( "m variable Right peak 1" )
  Make/D/N=(field) /O root:$(FolderName):Coefficients:$( "m variable left peak 2" )
  Make/D/N=(field) /O root:$(FolderName):Coefficients:$( "m variable Right peak 2" )
  Make/D/N=(field) /O root:$(FolderName):Coefficients:$( "ErrBaselines" )
  Make/D/N=(field) /O root:$(FolderName):Coefficients:$( "ErrBackStep" )
  Make/D/N=(field) /O root:$(FolderName):Coefficients:$( "ErrCenter1" )
```

Make/D/N=(field) /O root:\$(FolderName):Coefficients:\$("ErrCenter2")
 Make/D/N=(field) /O root:\$(FolderName):Coefficients:\$("ErrY0 Peak 2")
 Make/D/N=(field) /O root:\$(FolderName):Coefficients:\$("ErrArea Left Peak 1")
 Make/D/N=(field) /O root:\$(FolderName):Coefficients:\$("ErrArea Right Peak 1")
 Make/D/N=(field) /O root:\$(FolderName):Coefficients:\$("ErrArea Left Peak 2")
 Make/D/N=(field) /O root:\$(FolderName):Coefficients:\$("ErrArea Right Peak 2")
 Make/D/N=(field) /O root:\$(FolderName):Coefficients:\$("Errm variable left peak 1")
 Make/D/N=(field) /O root:\$(FolderName):Coefficients:\$("Errm variable Right peak 1")
 Make/D/N=(field) /O root:\$(FolderName):Coefficients:\$("Errm variable left peak 2")
 Make/D/N=(field) /O root:\$(FolderName):Coefficients:\$("Errm variable Right peak 2")

//New waves to hold calculated values

Make/D/N=(field) /O root:\$(FolderName):Coefficients:\$("Numerical Area Peak 1")
 Make/D/N=(field) /O root:\$(FolderName):Coefficients:\$("Numerical Area Peak 2")

Make/D/N=(field) /O root:\$(FolderName):Coefficients:\$("I002/I200")

//New waves for the run specs

Make /N=59 /O root:\$(FolderName):RunSpecs:tt002

//Make short reference for each of the new waves

Wave Ba = root:\$(FolderName):Coefficients:\$("Baselines")
 Wave BS = root:\$(FolderName):Coefficients:\$("BackStep")
 Wave C1 = root:\$(FolderName):Coefficients:\$("Center1")
 Wave C2 = root:\$(FolderName):Coefficients:\$("Center2")
 Wave amp2 = root:\$(FolderName):Coefficients:\$("Y0Peak2")
 Wave AL1 = root:\$(FolderName):Coefficients:\$("Area Left Peak 1")
 Wave AR1 = root:\$(FolderName):Coefficients:\$("Area Right Peak 1")
 Wave AL2 = root:\$(FolderName):Coefficients:\$("Area Left Peak 2")
 Wave AR2 = root:\$(FolderName):Coefficients:\$("Area Right Peak 2")
 Wave mL1 = root:\$(FolderName):Coefficients:\$("m variable left peak 1")
 Wave mR1 = root:\$(FolderName):Coefficients:\$("m variable Right peak 1")
 Wave mL2 = root:\$(FolderName):Coefficients:\$("m variable left peak 2")
 Wave mR2 = root:\$(FolderName):Coefficients:\$("m variable Right peak 2")
 Wave ErrBa = root:\$(FolderName):Coefficients:\$("ErrBaselines")
 Wave ErrBS = root:\$(FolderName):Coefficients:\$("ErrBackStep")
 Wave ErrC1 = root:\$(FolderName):Coefficients:\$("ErrCenter1")
 Wave ErrC2 = root:\$(FolderName):Coefficients:\$("ErrCenter2")
 Wave Erramp2 = root:\$(FolderName):Coefficients:\$("ErrY0 Peak 2")
 Wave ErrAL1 = root:\$(FolderName):Coefficients:\$("ErrArea Left Peak 1")
 Wave ErrAR1 = root:\$(FolderName):Coefficients:\$("ErrArea Right Peak 1")
 Wave ErrAL2 = root:\$(FolderName):Coefficients:\$("ErrArea Left Peak 2")
 Wave ErrAR2 = root:\$(FolderName):Coefficients:\$("ErrArea Right Peak 2")

```
Wave ErrmL1 = root:$(FolderName):Coefficients:$("Errm variable left peak 1")
Wave ErrmR1 = root:$(FolderName):Coefficients:$("Errm variable Right peak 1")
Wave ErrmL2 = root:$(FolderName):Coefficients:$("Errm variable left peak 2")
Wave ErrmR2 = root:$(FolderName):Coefficients:$("Errm variable Right peak 2")
```

```
Wave NA1 = root:$(FolderName):Coefficients:$("Numerical Area Peak 1")
Wave NA2 = root:$(FolderName):Coefficients:$("Numerical Area Peak 2")
```

```
Wave RI = root:$(FolderName):Coefficients:$("I002/I200")
```

```
Wave d = root:$(FolderName):tt002
```

```
k=0
```

```
//First must put into new waves
For(k=0; k<DimSize(Matname, 1); k+=1)
```

```
    //Initialize guesses for fit coefficients
    W_coef[0] = 200//Base
    W_coef[1] = 1 //slope
    W_coef[2] = 3.92//Center1
    W_coef[3] = 4.003 //Center2
    W_coef[4] = 33000 // Y0 Value peak 2
    W_coef[5] = 0.043// Area Left Peak 1
    W_coef[6] = 0.01// Area Right Peak 1
    W_coef[7] = 0.015// Area Left Peak 2
    W_coef[8] = 0.02// Area Right Peak 2
    W_coef[9] = 5 // m variable Left Peak 1
    W_coef[10] = 0.6//m variable Right Peak 1
    W_coef[11] = 1.2//m variable Left Peak 2
    W_coef[12] = 4.3//m variable Right Peak 2
```

```
    Make /N=59 /O root:$(FolderName):CalibratedData:$("field" + num2str(k+1))
    wave CD = root:$(FolderName):CalibratedData:$("field" + num2str(k+1))
    Make /N=59 /O root:$(FolderName):StandardDevs:$("field" + num2str(k+1))
    wave STDV = root:$(FolderName):StandardDevs:$("field" + num2str(k+1))
```

```
    For(j=0;j<59 ;j+=1)
```

```
        CD[j] = Matname[j][k]
```

```
    EndFor
```

```

STDV = 1/Sqrt(CD)

//Now must fit peaks to each new wave

Variable V_fitOptions = 4 // suppress progress window
Variable V_FitError = 0 // prevent abort on error

Make /N=2000 /O root:$(FolderName):FitData:$( "fit_field" + num2str(k+1))

Wave FD = root:$(FolderName):FitData:$( "fit_field" + num2str(k+1))

//Fit with double AsymPearson 7 Equal strain approximation
FuncFit /L=2000 /N/Q DoubleAsymP7s_EqualStrain W_coef CD /D/X=d
/W=STDV /C=T_Constraints

Wave TF = $( "fit_field" + num2str(k+1))

FD = TF

KillWaves $( "fit_field" + num2str(k+1))

Wave WC = W_coef
Wave WS = W_sigma

// save the coefficients
Ba[k] = WC[0]
BS[k] = WC[1]
C1[k] = WC[2]
C2[k] = WC[3]
amp2[k] = WC[4]
AL1[k] = WC[5]
AR1[k] = WC[6]
AL2[k] = WC[7]
AR2[k] = WC[8]
mL1[k] = WC[9]
mR1[k] = WC[10]
mL2[k] = WC[11]
mR2[k] = WC[12]

ErrBa[k] = WS[0]
ErrBS[k] = WS[1]
ErrC1[k] = WS[2]
ErrC2[k] = WS[3]
Erramp2[k] = WS[4]
ErrAL1[k] = WS[5]

```

```

ErrAR1[k] = WS[6]
ErrAL2[k] = WS[7]
ErrAR2[k] = WS[8]
ErrmL1[k] = WS[9]
ErrmR1[k] = WS[10]
ErrmL2[k] = WS[11]
ErrmR2[k] = WS[12]

//Make component waves in the components folder
componentpath = "root:" + FolderName + ":PeakComponents"
MakeCompAsymDoubleP7s_ESfolder(WC, d[0], d[numpnts(d)-1], "field" +
num2str(k+1), componentpath)

"Peak1") Wave P1 = root:$(foldername):peakcomponents:$( "field" + num2str(k+1) +
"Peak2") Wave P2 = root:$(foldername):peakcomponents:$( "field" + num2str(k+1) +
"reconX") Wave RX = root:$(foldername):peakcomponents:$( "field" + num2str(k+1) +

//*****Need to set the scale of these waves before these are comparable to the
calculated values
NA1[k] = areaXY(RX, P1, (WC[2] - (WC[3] - WC[2])), (WC[2] +(WC[3] -
WC[2]))) // Area 1 Numeric (integrated intensity)
NA2[k] = areaXY(RX, P2, (WC[3] - (WC[3] - WC[2])), (WC[3] + (WC[3] -
WC[2]))) // Area 2 Numeric (integrated intensity)

RI[k] = NA1[k]/NA2[k] //ratio of integrated intensities

EndFor

End

```

Igor code for fitting doublet peaks and recalculating intensities for the deconvoluted peaks. This code is called for by the code for calculating ratio of integrated intensities of diffraction peaks constituting a doublet, such as 002 and 200 for a tetragonal sample, for different time periods during application of cyclic electric fields of different amplitudes

```
#pragma rtGlobals=1          // Use modern global access method.
// this function fit doublet peaks to a asymmetric pearson VII function
```

```
Function DoubleAsymP7s_EqualStrain(w, x) : FitFunc
```

```
    wave w
    variable x
    variable result1
    variable result2
    variable result3
    variable result4
    variable result5
    variable y01 //y0 value calculated for peak 2 assuming there is equal strain between the
002 and 200 domains
```

```
    //    W_coef[0] = 500 //Base
    //    W_coef[1] = 200 // Background Step : Now changed to slope
    //    W_coef[2] = 57.55//Center1
    //    W_coef[3] = 58.2 //Center2
    //    W_coef[4] = 2000 // Y0 Value peak 2
    //    W_coef[5] = 9000 // Area Left Peak 1
    //    W_coef[6] = 7000 // Area Right Peak 1
    //    W_coef[7] = 4000 // Area Left Peak 2
    //    W_coef[8] = 3000 // Area Right Peak 2
    //    W_coef[9] = 5 // m variable Left Peak 1
    //    W_coef[10] = 5 //m variable Right Peak 1
    //    W_coef[11] = 8 //m variable Left Peak 2
    //    W_coef[12] = 8 //m variable Right Peak 2
```

```
    y01 = w[4]*((w[7]*gamma(w[11]-0.5)/gamma(w[11])) - (w[8]*gamma(w[12]-
0.5)/gamma(w[12]))) / ((w[6]*gamma(w[10]-0.5)/gamma(w[10])) - (w[5]*gamma(w[9]-
0.5)/gamma(w[9])))
```

```
    if (x<w[2]) //left hand side of peak 1
        result1= y01* (1+((x-w[2])^2)/((w[5]^2))^-w[9])
    else
        result1=0
    endif
```

```

if (x>w[2]) //right hand side of peak 1
  result2= y01 * (1+((x-w[2])^2)/((w[6]^2))^-w[10])
  else
  result2=0
endif

if (x<w[3]) //left hand side of peak 2
  result3= w[4]*(1+((x-w[3])^2)/((w[7]^2))^-w[11])
  else
  result3=0
endif

if (x>w[3]) //right hand side of peak 2
  result4= w[4]*(1+((x-w[3])^2)/((w[8]^2))^-w[12])
  else
  result4=0
endif

return w[0] + w[1]*x + result1 + result2 + result3 + result4

```

End

Function MakeCompAsymDoubleP7s_ES(w, startx, endx, prefix) // this function recalculate the intensities for the deconvoluted peaks

```

wave w
variable startx
variable endx
string prefix
variable i, y01

Make /N = 500 /O $(prefix + "Peak1"), $(prefix + "Peak2"), $(prefix + "Background"),
$(prefix + "reconX")

Wave peak1 = $(prefix + "Peak1")
Wave peak2 = $(prefix + "Peak2")
Wave reconX = $(prefix + "reconX")
Wave Background = $(prefix + "Background")

y01 = w[4]*((w[7]*gamma(w[11]-0.5)/gamma(w[11])) - (w[8]*gamma(w[12]-
0.5)/gamma(w[12]))) / ((w[6]*gamma(w[10]-0.5)/gamma(w[10])) - (w[5]*gamma(w[9]-
0.5)/gamma(w[9])))

For (i=0;i<500;i+=1)

```

```

reconX[i] = startx + i*((endx - startx)/499)
Background[i] = w[0] + w[1]*x

if (reconX[i]<w[3]) //left hand side of peak 2
    peak2[i] = w[4]*(1+((reconX[i]-w[3])^2)/((w[7]^2))^-w[11])
endif

if (reconX[i]>w[3]) //right hand side of peak 2
    peak2[i] = w[4]*(1+((reconX[i]-w[3])^2)/((w[8]^2))^-w[12])
endif

if (reconX[i]<w[2]) //left hand side of peak 1
    peak1[i] = y01* (1+((reconX[i]-w[2])^2)/((w[5]^2))^-w[9])
endif

if (reconX[i]>w[2]) //right hand side of peak 1
    peak1[i] = y01* (1+((reconX[i]-w[2])^2)/((w[6]^2))^-w[10])
endif

Endfor

```

End

Function MakeCompAsymDoubleP7s_ESfolder(w, startx, endx, prefix, folder) // this function recalculate the intensities for the deconvoluted peaks, specific folder is specified

```

wave w
variable startx
variable endx
string prefix
string folder
string currentfolder
variable i, y01

currentfolder = GetDataFolder(1)
SetDataFolder folder

Make /N = 500 /O $(prefix + "Peak1"), $(prefix + "Peak2"), $(prefix + "Background"),
$(prefix + "reconX")

Wave peak1 = $(prefix + "Peak1")
Wave peak2 = $(prefix + "Peak2")
Wave reconX = $(prefix + "reconX")
Wave Background = $(prefix + "Background")

```

```

y01 = w[4]*((w[7]*gamma(w[11]-0.5)/gamma(w[11])) - (w[8]*gamma(w[12]-
0.5)/gamma(w[12]))) / ((w[6]*gamma(w[10]-0.5)/gamma(w[10])) - (w[5]*gamma(w[9]-
0.5)/gamma(w[9])))

```

```

For (i=0;i<500;i+=1)

```

```

    reconX[i] = startx + i*((endx - startx)/499)

```

```

    Background[i] = w[0] + w[1]*x

```

```

    if (reconX[i]<w[3]) //left hand side of peak 2

```

```

        peak2[i] = w[4]*(1+((reconX[i]-w[3])^2)/((w[7]^2))^-w[11])

```

```

    endif

```

```

    if (reconX[i]>w[3]) //right hand side of peak 2

```

```

        peak2[i] = w[4]*(1+((reconX[i]-w[3])^2)/((w[8]^2))^-w[12])

```

```

    endif

```

```

    if (reconX[i]<w[2]) //left hand side of peak 1

```

```

        peak1[i] = y01* (1+((reconX[i]-w[2])^2)/((w[5]^2))^-w[9])

```

```

    endif

```

```

    if (reconX[i]>w[2]) //right hand side of peak 1

```

```

        peak1[i] = y01* (1+((reconX[i]-w[2])^2)/((w[6]^2))^-w[10])

```

```

    endif

```

```

Endfor

```

```

SetDataFolder currentfolder

```

```

End

```

Igor code to input integrated intensities for different electric field amplitudes into a single wave

```
#pragma rtGlobals=1          // Use modern global access method.
function inputarea(wave0) // this function inputs integrated intensities of doublet peaks for
different amplitudes of applied electric fields in a single wave

string wave0
variable i, j
string foldername

foldername = getdatafolder (0)

make /N=(16,2) root:$(foldername):eta:$( "areapos" )
make /N=(16,2) root:$(foldername):eta:$( "areaneg" )

wave apos = root:$(foldername):eta:$( "areapos" )
wave aneg = root:$(foldername):eta:$( "areaneg" )

wave posp1= root:$(foldername):positive:Coefficients:$( "Numerical Area Peak 1" )
wave posp2= root:$(foldername):positive:Coefficients:$( "Numerical Area Peak 2" )
wave negp1= root:$(foldername):negative:Coefficients:$( "Numerical Area Peak 1" )
wave negp2= root:$(foldername):negative:Coefficients:$( "Numerical Area Peak 2" )

for (i=0;i<16;i+=1)
  apos[i][0]= posp1[i]
  apos[i][1]= posp2[i]
  aneg[i][0]= negp1[i]
  aneg[i][1]= negp2[i]
endfor

end
```

Igor code for calculating etas for different amplitudes of applied electric fields

```
#pragma rtGlobals=1          // Use modern global access method.
function calceta(wave1, wave2) // this function calculates eta values for different amplitudes of
applied electric fields

wave wave1, wave2
variable i, p1, p2 // p1 is peak 002 and p2 is peak 200

p1=323.038 // integrated intensities of the specific peak for unpoled sample
p2=753.087

make /N=16 $("etadiff")
make /N=16 $("etapos")
make /N=16 $("etaneg")

wave epos = $("etapos")
wave eneg = $("etaneg")
wave ediff = $("etadiff")

for (i=0; i<16; i+=1)
  epos[i] = ((wave1[i][0]/p1)/((wave1[i][0]/p1)+2*(wave1[i][1]/p2)))-(1/3)
  eneg[i] = ((wave2[i][0]/p1)/((wave2[i][0]/p1)+2*(wave2[i][1]/p2)))-(1/3)
  ediff[i] = epos[i] - eneg[i]
endfor

end
```

Igor code for fitting a single peak, such as 111 for a tetragonal sample, for different amplitudes of applied electric fields. The function for fitting used here is Asymmetric Pearson VII.

```
#pragma rtGlobals=1          // Use modern global access method.
```

```
Function MakeAndFit111f(W2DMat) // this function fit a single peak such as 111 for different amplitudes of applied electric fields
```

```
Wave W2DMat
```

```
variable i, j, field  
string FolderName
```

```
field = Dimsize(W2DMat, 1)
```

```
FolderName = GetDataFolder(0)
```

```
NewDataFolder /O root:$(FolderName):StandardDevs  
NewDataFolder /O root:$(FolderName):CalibratedData  
NewDataFolder /O root:$(FolderName):FitData  
NewDataFolder /O root:$(FolderName):Coefficients  
NewDataFolder /O root:$(FolderName):RunSpecs
```

```
Make/D/N=(field) /O root:$(FolderName):Coefficients:$( "Baselines" )  
Make/D/N=(field) /O root:$(FolderName):Coefficients:$( "Amplitude" )  
Make/D/N=(field) /O root:$(FolderName):Coefficients:$( "Centre" )  
Make/D/N=(field) /O root:$(FolderName):Coefficients:$( "WidthLeft" )  
Make/D/N=(field) /O root:$(FolderName):Coefficients:$( "mLeft" )  
Make/D/N=(field) /O root:$(FolderName):Coefficients:$( "WidthRight" )  
Make/D/N=(field) /O root:$(FolderName):Coefficients:$( "mRight" )  
Make/D/N=(field) /O root:$(FolderName):Coefficients:$( "Slope" )
```

```
Make/D/N=(field) /O root:$(FolderName):Coefficients:$( "ErrBaselines" )  
Make/D/N=(field) /O root:$(FolderName):Coefficients:$( "ErrAmplitude" )  
Make/D/N=(field) /O root:$(FolderName):Coefficients:$( "ErrCentre" )  
Make/D/N=(field) /O root:$(FolderName):Coefficients:$( "ErrWidthLeft" )  
Make/D/N=(field) /O root:$(FolderName):Coefficients:$( "ErrmLeft" )  
Make/D/N=(field) /O root:$(FolderName):Coefficients:$( "ErrWidthRight" )  
Make/D/N=(field) /O root:$(FolderName):Coefficients:$( "ErrmRight" )  
Make/D/N=(field) /O root:$(FolderName):Coefficients:$( "ErrSlope" )
```

```
Make/D/N = 8 /O W_Coef //New waves to hold fitted data  
Make/D/N = 8 /O W_Sigma //Errors wave
```

```
Make /N=36 /O root:$(FolderName):RunSpecs:tt111
```

```
Wave Ba = root:$(FolderName):Coefficients:$( "Baselines" )  
Wave Am = root:$(FolderName):Coefficients:$( "Amplitude" )  
Wave Ce = root:$(FolderName):Coefficients:$( "Centre" )  
Wave WL = root:$(FolderName):Coefficients:$( "WidthLeft" )  
Wave ML = root:$(FolderName):Coefficients:$( "mLeft" )  
Wave WR = root:$(FolderName):Coefficients:$( "WidthRight" )  
Wave MR = root:$(FolderName):Coefficients:$( "mRight" )  
Wave S = root:$(FolderName):Coefficients:$( "Slope" )
```

```
Wave ErrBa = root:$(FolderName):Coefficients:$( "ErrBaselines" )  
Wave ErrAm = root:$(FolderName):Coefficients:$( "ErrAmplitude" )  
Wave ErrCe = root:$(FolderName):Coefficients:$( "ErrCentre" )  
Wave ErrWL = root:$(FolderName):Coefficients:$( "ErrWidthLeft" )  
Wave ErrML = root:$(FolderName):Coefficients:$( "ErrMixLeft" )  
Wave ErrWR = root:$(FolderName):Coefficients:$( "ErrWidthRight" )  
Wave ErrMR = root:$(FolderName):Coefficients:$( "mRight" )  
Wave ErrS = root:$(FolderName):Coefficients:$( "ErrSlope" )
```

```
Wave d= root:$(FolderName):tt111
```

```
i=0
```

```
For(i=0; i<DimSize(W2DMat, 1); i+=1)
```

```
//Initialize guesses for fit coefficients
```

```
W_coef[0] = 10 //Base  
W_coef[1] = 1 //Slope  
W_coef[2] = 41200 //Y0  
W_coef[3] = 0.047 //a left  
W_coef[4] = 0.042// a right  
W_coef[5] = 12 // m left  
W_coef[6] = 9.8 // m right  
W_coef[7] = 3.435 // center
```

```
Make /N=36 /O root:$(FolderName):CalibratedData:$( "Field" +  
num2str(50*i+100))  
wave CD = root:$(FolderName):CalibratedData:$( "Field" + num2str(50*i+100))
```

```

        Make /N=36 /O root:$(FolderName):StandardDevs:$("Time" +
num2str(50*i+100))
        wave STDV = root:$(FolderName):StandardDevs:$("Time" +
num2str(50*i+100))

//input data
For(j=0;j<36 ;j+=1)

        CD[j] = W2DMat[j][i]

EndFor

STDV = 1/Sqrt(CD)

Variable V_fitOptions = 4 // suppress progress window
Variable V_FitError = 0 // prevent abort on error

        Make /N=2000 /O root:$(FolderName):FitData:$("fit_Field" +
num2str(50*i+100))

Wave FD = root:$(FolderName):FitData:$("fit_Field" + num2str(50*i+100))

FuncFit /L=2000 /N/Q AssymP7Elderton W_coef CD /D/X=d /W=STDV
/C=T_Constraints

Wave TF = $("fit_Field" + num2str(50*i+100))

FD = TF

KillWaves $("fit_Field" + num2str(50*i+100))

Wave WC = W_coef
Wave WS = W_sigma

Ba[i] = W_coef[0]
Am[i] = W_coef[2]
Ce[i] = W_coef[7]
WL[i] = W_coef[3]
ML[i] = W_coef[5]
WR[i] = W_coef[4]
MR[i] = W_coef[6]

```

S[i] = W_coef[1]

ErrBa[i] = W_sigma[0]

ErrAm[i] = W_sigma[2]

ErrCe[i] = W_sigma[7]

ErrWL[i] = W_sigma[3]

ErrML[i] = W_sigma[5]

ErrWR[i] = W_sigma[4]

ErrMR[i] = W_sigma[6]

ErrS[i] = W_sigma[1]

Endfor

End

Igor code for fitting single peaks. This code is called for by the code for fitting single peaks and calculating peak parameters, for different time periods during application of cyclic electric fields of different amplitudes

```
#pragma rtGlobals=1      // Use modern global access method.
```

```
Function AssymP7Elderton(w, x) : FitFunc
```

```
    wave w
    variable x
    variable result1
    variable result2
    variable final

    //W_coef[0] = //Base
    //W_coef[1] = //Slope
    //W_coef[2] = // Y0
    //W_coef[3] = // a left
    //W_coef[4] = // a right
    //W_coef[5] = // m left
    //W_coef[6] = //m right
    //W_coef[7] = // center

    if (x>w[7]) //right hand side of peak 1
        result2= w[2]*(1+(x-w[7])^2/w[4]^2)^-w[6]
    else
        result2=0
    endif

    if (x<w[7]) //left hand side of peak 1
        result1= w[2]*(1+(x-w[7])^2/w[3]^2)^-w[5]
    else
        result1=0
    endif

    final = w[0] + w[1]*x + result1 + result2

    return final
```

```
End
```

REFERENCES

- [1] Zupan M, Ashby MF, Fleck NA, *Adv Engg Mat* 2002; 4:933.
- [2] Nye JF, *Physical Properties of Crystals*, Oxford University Press, 1957.
- [3] Hall DA, *J Mater Sci* 2001; 36:4575.
- [4] Damjanovic D, Chapter 4 in Vol. III of *Science of Hysteresis*, ed. G. Bertotti and I. Mayergoyz, Elsevier, 337 (2005).
- [5] Damjanovic D, *J Am Ceram Soc* 2005; 88:2663.
- [6] Jaffe B, Cook WR, Jaffe H, *Piezoelectric Ceramics* (Academic, London, 1971).
- [7] Setter N ed., *Piezoelectric Materials in Devices* (Lausanne: EPFL) pp 163–82 (ISBN: 2-9700346-0-3).
- [8] Moulson AJ and Herbert JM, *Electroceramics*, John Wiley & Sons, Inc., Second Edition, 2003.
- [9] Jones JL, *J Electroceram* 2007; 19:67.
- [10] Hall DA, *J Mater Sci* 2001; 36:4575.
- [11] Herbiet R, Robels U, Dederichs H, Arlt G, *Ferroelectrics* 1989; 98:107.
- [12] Fu H, Cohen RE, *Nature* 2000; 403:281.
- [13] Bellaiche L, Vanderbilt D, *Phys Rev Lett* 1999; 83:1347.
- [14] Bellaiche L, Garcia A, Vanderbilt D, *Phys Rev Lett* 2000; 84:5427.
- [15] Bellaiche L, Garcia A, Vanderbilt D, *Phys Rev B* 2001; 64:060103.
- [16] Garcia A, Vanderbilt D, *Appl Phys Lett* 1998; 72:2981.
- [17] Devonshire AF, *Phil Mag* 1949; 40:1040.
- [18] Devonshire AF, *Phil Mag* 1949; 42:1065.
- [19] Haun MJ, Furman E, Jang SJ, Cross LE, *Ferroelectrics* 1989; 99:13.
- [20] Haun MJ, Furman E, McKinstry HA, Cross LE, *Ferroelectrics* 1989; 99:27.
- [21] Haun MJ, Zhuang ZQ, Furman E, Jang SJ, Cross LE, *Ferroelectrics* 1989; 99:45.
- [22] Haun MJ, Furman E, Halemane TR, Cross LE, *Ferroelectrics* 1989; 99:55.

- [23] Haun MJ, Furman E, Jang SJ, Cross LE, *Ferroelectrics* 1989; 99:63.
- [24] Haun MJ, Furman E, Jang SJ, McKinstry HA, Cross LE, *J Appl Phys* 1987; 62:3331.
- [25] Damjanovic D, Budimir M, Davis M, Setter N, *J Mater Sci* 2006; 41:65.
- [26] Budimir M, Damjanovic D, Setter N, *Phys Rev B: Cond Mat and Mat Phys* 2006; 73:174106.
- [27] Davis M, Budimir M, Damjanovic D, Setter N, *J Appl Phys* 2007; 101:054112.
- [28] Jones JL, Pramanick A, Nino JC, Motahari SM, Üstündag E, Daymond MR, Oliver EC, *Appl Phys Lett* 2007; 90:172909.
- [29] Guo R, Cross LE, Park SE, Noheda B, Cox DE, Shirane G, *Phys Rev Lett* 2000; 84:5423.
- [30] Hall DA, Steuwer A, Cherdhirunkron B, Mori T, Withers PJ, *J Appl Phys* 2004; 96:4245.
- [31] Hall DA, Steuwer A, Cherdhirunkorn B, Withers PJ, Mori T, *J Mech Phys Solids* 2005; 53:249.
- [32] Von Hippel A, *Rev Mod Phys* 1950; 22:221.
- [33] Lewis B, *Proc Phys Soc (London)* 1960; 73:17.
- [34] Hagemann H-J, *J Phys C: Solid State Phys* 1978; 11:3333.
- [35] Li S, Cao W, Cross LE, *J Appl Phys* 1991; 69:7219.
- [36] Robels U, Zadon C, Arlt G, *Ferroelectrics* 1992; 133:163.
- [37] Hall DA, *Ferroelectrics* 1999; 223:319.
- [38] Hall DA, Ben-Omran MM, Stevenson PJ, *J Phys: Condensed Matter* 1998; 10:461.
- [39] Hall DA, Stevenson PJ, *Ferroelectrics* 1999; 228:139.
- [40] Garcia JE, Perez R, Albareda A, *J Phys: Condensed Matter* 2005; 17: 7143.
- [41] Garcia JE, Perez R, Ochoa DA, Albareda A, Lente MH, Eiras JA, *J Appl Phys* 2008; 103:054108.
- [42] Demartin M, Damjanovic D, *Appl Phys Lett* 1996; 68:3046.
- [43] Damjanovic D, Demartin M, *J Phys D: Appl Phys* 1996; 29:2057.
- [44] Damjanovic D, *Phys Rev B* 1997; 55:R649.
- [45] Lord Rayleigh, *Phil Mag* 1887; 23:225.

- [46] Kugel VD, Cross LE, J Appl Phys 1998; 84:2815.
- [47] Eitel RE, ShROUT TR, Randall CA, J Appl Phys 2006; 99:124110.
- [48] Weiss P, De Freudenreich D, Arch Sc Phys Nat Geneve 1916; 42:449.
- [49] Preisach F, Zeitschrift fur Physik 1935; 94:277.
- [50] Neel L, Chiers de Physique 1942; 12:1.
- [51] Bertotti G, "Hysteresis in Magnetism" (Academic Press, 1998).
- [52] Turik AV, Soviet Phys – Solid State 1963; 5:885.
- [53] Turik AV, Soviet Phys – Solid State 1964; 5:1751.
- [54] Turik AV, Soviet Phys – Solid State 1964; 5:2141.
- [55] Robert G, Damjanovic D, Setter N, Appl Phys Lett 2000; 77:4413.
- [56] Robert G, Damjanovic D, Setter N, Turik AV, J Appl Phys 2001; 89:5067.
- [57] Robert G, Damjanovic D, Setter N, J Appl Phys 2001; 90:2459.
- [58] Mayergoyz ID, Mathematical Models of Hysteresis, Springer-Verlag, New York, 1991.
- [59] Ge P, Jouaneh M, Precision Engineering 1995; 17:211.
- [60] Ge P, Jouaneh M, Precision Engineering 1997; 20:99.
- [61] Hwang SC, Lynch CS, McMeeking RM, Acta Metall Mater 1995; 45:2073.
- [62] Hwang SC, Huber JE, McMeeking RM, Fleck NA, J Appl Phys 1998; 84:1530.
- [63] Subbarao EC, McQuarrie MC, Buessem WR, J Appl Phys 1957; 28:1194.
- [64] Saito Y, Jpn J Appl Phys 1997; 36:5963.
- [65] Bedoya C, Muller Ch, Baudour J.-L, Madigou V, Anne M, Roubin M, Mater Sci Engg B 2001; 75:43.
- [66] Hoffmann MJ, Hammer M, Endriss A, Lupascu DC, Acta mater 2001; 49:1301.
- [67] Wan S, Bowman KJ, J Mater Res 2001; 16:2306.
- [68] Hall DA, Steuwer A, Cherdhirunkorn B, Withers PJ, Mori T, Mater Sci Eng A 2005; 409:206.
- [69] Jones JL, Slamovich EB, Bowman KJ, J Appl Phys 2005; 97:034113.

- [70] Kungl H, Theissmann R, Knapp M, Baecht C, Fuess H, Wagner S, Fett T, Hoffmann MJ, Acta mater 2007; 55:1849.
- [71] Jones JL, Pramanick A, Daniels JE, Appl Phys Lett 2008; 93:152904.
- [72] Jones JL, Hoffman M, Daniels JE, Studer AJ, Appl Phys Lett 2006; 89:092901.
- [73] Daniels JE, Finlayson TR, Studer AJ, Hoffman M, Jones JL, J Appl Phys 2007; 101:094104.
- [74] Jones JL, Pramanick A, Nino JC, Motahari SM, Üstündag E, Daymond MR, Oliver EC, Appl Phys Lett 2007; 90:172909.
- [75] Noheda B, Cox DE, Shirane G, Gonzalo JA, Cross LE, Park S-E, Appl Phys Lett 1999; 74:2059.
- [76] Noheda B, Cox DE, Phase Transitions 2006; 79:5.
- [77] Swartz SL, Shrout TR, Mat Res Bull 1982; 17:1245.
- [78] Randall CA, Kim N, Kucera J-P, Cao W, Shrout TR, J Am Ceram Soc 1998; 81:677.
- [79] Pramanick A, Damjanovic D, Juan C Nino, Jones JL, Acta Mat submitted.
- [80] Damjanovic D, J Appl Phys 1997; 82:1788.
- [81] Trolier-McKinstry S, Gharb NB, Damjanovic D, Appl Phys Lett 2006; 88:202901.
- [82] Schönau KA, Schmitt LA, Knapp M, Fuess H, Eichel R-A, Kungl H, Hoffmann MJ, Phys Rev B 2007; 75:184117.
- [83] Daniels JE, Jones JL, Finlayson TR, J. Phys. D 2006; 39, 5294.
- [84] Daniels JL, Pramanick A, Jones JL, IEEE Trans on UFFC, accepted for publication 2008.
- [85] Daniels JE, Drakopoulos, J Synchrotron Rad submitted.
- [86] Hammersley AP. ESRF Internal Report, ESRF98HA01T, FIT2D V9.129 Reference Manual V3.1 (1998).
- [87] Hammersley AP, Svensson SO, Hanfland M, Fitch AN, Häusermann D, *High Pressure Res* 1996; 14:235.
- [88] Rietveld HM, J Appl Crystallogr 1969; 2:65.
- [89] Barsch GR, Krumhansl JA, Phys Rev Lett 1984; 53:1069.
- [90] Jacobs AE, Phys Rev B :Condensed Matter 1985; 31:5984.

- [91] Taylor DR, Swainson IP, J Phys: Condensed Matter 1998; 10:10207.
- [92] Elderton WP, Johnson NL, Systems of frequency curves, Cambridge University Press, Cambridge, 1969, 77-79.
- [93] Hammer M, Hoffmann MJ, J. Electroceramics 1998; 2:75.
- [94] Noheda B, Cox DE, Shirane G, Guo R, Jones B, Cross LE, Phys Rev B 2000; 63:014103.
- [95] Jones JL, Hoffman M, Bowman KJ, J Appl Phys 2005; 98:024115.
- [96] Daymond MR, J Appl Phys 2004; 96:4263.
- [97] Damjanovic D, Demartin D, Shulman HS, Testorf M, Setter N, Sensors and Actuators A 1996, 53:353.
- [98] Pramanick A, Daniels JE, Jones JL, unpublished work.
- [99] Pramanick A, Prewitt AD, Cottrell MA, Lee W, Studer AJ, An K, Hubbard CR, Jones JL, Appl Phys A, submitted.
- [100] Meyer B, Vanderbilt D, Phys Rev B 2002; 65:104111.
- [101] Maeder MD, Damjanovic D, Setter N, J Electroceramics 2004; 13:385.
- [102] Ochoa DA, Garcia JE, Perez R, Gomis V, Albareda A, Rubio-Marcos F, Fernandez JF, J Phys D: Appl Phys 2009; 42:025402.
- [103] Dai Y, Zhang X, Zhu G, Appl Phys Lett 2007; 90:262903.
- [104] Kholkin AL, Calzada ML, Ramos P, Mendiola J, Setter N, Appl Phys Lett 1996, 69:3602.
- [105] Xu F, Troiler-McKinstry S, Ren W, Xu B, Xie ZL, Hemker KJ, J Appl Phys 2001, 89:1336.
- [106] Bassiri-Gharb N, Fujii I, Hong E, Troiler-McKinstry S, Taylor DV, Damjanovic D, J Electroceram 2007, 19:47.
- [107] Pramanick A, Omar S, Nino JC, Jones JL, J Appl Crystallogr in press.
- [108] Cullity BD, *Elements of X-ray Diffraction*, Addison-Wesley Publishing Company Inc., Second Edition, 1978.
- [109] <http://physics.nist.gov/PhysRefData/XrayMassCoef/tab3.html>.

BIOGRAPHICAL SKETCH

Abhijit Pramanick was born on October of 1980 in Toofanganj, a little known small town in India. Over time he traveled extensively and lived in different places in India. He received a Bachelor of Engineering in Metallurgy from the National Institute of Technology (NIT), Rourkela, India in July of 2002. He then moved to the Indian Institute of Science (IISc) located at Bangalore, a south Indian city of technological prominence. He enjoyed the city life of Bangalore and the academic environment of the campus in IISc. He received a Master of Engineering in Metallurgy from IISc in 2004. He then joined KLA-Tencor Corporation as an Applications Development Engineer. As part of his job, he traveled to countries including the USA, Singapore, China and South Korea. As much as he liked traveling, he was eventually getting tired of such a mobile lifestyle. He left his job in August 2005 and joined the Department of Materials Science and Engineering at the University of Florida (UF) as a PhD student. He joined Dr. Jacob Jones' research group in summer of 2006. He thoroughly enjoyed the exciting and cosmopolitan student life at UF. His last year as a PhD student has been quite eventful. During this time, he traveled across the globe, performed his experiments and analyses, and contributed to numerous scientific publications. He received his PhD from UF in the spring of 2009 and immediately started as a post-doctoral researcher at the New York State College of Ceramics at Alfred University, situated at Alfred, NY.

Apart from his general education in science and technology, he has often wondered about the meaning of all existences and of life in particular. He contemplated the viewpoints of science, religions and philosophies, but could never convince himself entirely. Though the truth has eluded him so far, he remains hopeful in figuring it out someday.